

https://dspace.org/

Research and development of thulium-doped fibre lasers

Morris, Daniel

2017

http://hdl.handle.net/10539/23529

Morris, Daniel (2017) Research and development of thulium-doped fibre lasers, University of the Witwatersrand, Johannesburg, <http://hdl.handle.net/10539/23529>

Downloaded from a DSpace repository. https://dspace.org/



UNIVERSITY OF THE
WITWATERSRAND,
JOHANNESBURG

Research and development of thulium-doped fibre lasers

by

Daniel Morris

A Dissertation submitted to the Faculty of Science, University of the Witwatersrand, in fulfilment of the requirements for the degree Master of Science

Johannesburg, 2017

Declaration

I declare that this dissertation is my own, unaided work. It has been submitted for the Degree of Master of Science at the University of the Witwatersrand. It has not been submitted before for any degree or examination at any other University.

_____

_____day of _____20_____in_____

Abstract

Three thulium-doped fibre lasers (TDFLs) were developed: a large mode area (LMA) 25/400 “test” TDFL, a high power cw TDFL, and a Q-switched TDFL. For the test TDFL, the relationship between self-pulsing in TDFLs and laser reabsorption effects were explored by way of spectral and temporal measurements. Laser design aspects and technical procedures were also investigated.

The highly efficient, high power cw TDFL produced a pump limited output power of 63 W with a slope efficiency of ~56 %. Thermal management schemes including splicing and fibre cooling were discussed and implemented.

A polarisation maintaining thulium-doped fibre (TDF) was implemented for the Q-switched TDFL which produced pulse lengths of ~207 ns and peak powers of 1.17 kW at ~23 W of average laser output power. Gain switching of the Q-switched TDFL pump diodes further reduced the output pulse length to ~163 ns with peak powers of 1.35 kW.

Dedication

To my wife, Lauren

Acknowledgements

I would firstly like to acknowledge and personally thank my supervisors, Dr. Lorinda Wu (CSIR), Dr. Wayne Koen (CSIR) and Prof. Andrew Forbes (Wits) for their contributions and input throughout this project, especially in the writing up phase of this dissertation. Your knowledge and patience was paramount to the completion of this dissertation.

In addition I would like to thank Gary King for his guidance and contribution to some of the technical aspects that accompanied this project, Cobus Jacobs for electrical (electronics) assistance, and Corrie Van der Westhuizen for the professional CAD designs.

I would also like to thank Dr. Hencharl Strauss, Dr. Darryl Naidoo, Ameeth Sharma, Nyameko Lisa, Loyiso Maweza, and Dr. Attie Hendriks for making me feel at home at the National Laser Centre (NLC), and always being willing to show support wherever possible.

I would personally like to thank my loving wife Lauren and my family and friends for their faith, love, and support given to me during the past few years.

Finally, I would like to thank the National Laser Centre (NLC), CSIR, for the opportunity to undertake this project by aiding with financial assistance towards this research.

Contents

Declaration....ii
Abstract....iii
Dedication....iv
Acknowledgements....v
List of Figures....ix
List of Tables....xiv
List of symbols and abbreviations....xv
Chapter 1: Introduction to silica based thulium-doped fibre lasers (TDFLs).... 1
Overview of the dissertation....1
1.1 Introduction to silica-based optical fibres 2
1.2 Absorption, stimulated and spontaneous emission 3
1.3 Basic laser concepts 4
1.4 Energy transfer mechanisms between rare-earth ions 8
1.5 Transmission spectra of silica 12
1.6 Self-pulsing in TDFLs.... 12
1.7 Wavelength selection 14
Chapter 2: Introductory Theory to large mode area (LMA) thulium-doped fibre lasers (TDFLs).... 15
2.1 Introduction 15
2.2 Numerical aperture (NA).... 15
2.3 Transverse modes in optical fibres and the *V* parameter.... 16
2.4 Large mode area (LMA) fibres.... 17
2.5 Beam quality 20
2.6 Longitudinal modes in fibres.... 23
2.7 Q-switching 24
2.8 Literature review on continuous wave and pulsed TDFLs 25
2.8.1 High power cw TDFLs 25
2.8.2 Discussion on high power CW TDFLs 28
2.8.3 Pulsed nanosecond TDFLs.... 29
2.8.4 Discussion on pulsed nanosecond TDFLs.... 30
Chapter 3: Design, cavity and temperature considerations for TDFLs.... 31
3.1 Introduction 31
3.2 Experimental design and setup.... 31
3.2.1 Fibre parameters and preparation techniques.... 31

3.2.2 Pump design and coupling efficiency 35
3.2.3 Laser design and setup 38
3.3 Experimental results and discussions 40
3.3.1 Optimisation of the TDFL cavity 40
3.3.2 Effect of air cooling on power, temporal stability and spectral output 44
3.3.3 TDF length and cavity considerations 49
3.3.4 Beam quality 50
3.4 Conclusions 51
Chapter 4: Development of a high power cw TDFL 51
4.1 Introduction 52
4.2 Experimental setup and procedures 52
4.2.1 Thermal management of the Tm-doped fibre 52
4.2.2 Thermal management of the TDF tip 55
4.2.3 Splicing 56
4.3 Laser design 63
4.3.1 Fibre parameters and laser design considerations 63
4.3.2 Laser development process 65
4.4 Experimental results and discussion 67
4.4.1 Laser development 67
4.4.2 Output stability of the high power TDFL with an intracavity HR mirror 70
4.4.3 Laser characterisation with intracavity 1939.8 nm and 2036.1 nm VBG's 73
4.5 Conclusions 77
Chapter 5: Development of a Q-switched TDFL 77
5.1 Introduction 78
5.2 Fibre preparation and pump setup 78
5.2.1 Fibre parameters 78
5.2.2 Fibre preparation 79
5.2.3 Pump design and coupling efficiency 80
5.3 Laser design 81
5.3.1 Laser design considerations 81
5.3.2 Setup and procedures 82
5.4 Experimental results and discussions 85
5.4.1 Continuous wave operation 85
5.4.2 Discussion 88
5.4.3 Q-switched operation 88
5.4.4 Gain switching the Q-switched TDFL 92

5.4.5 Beam quality of the Q-switched PM TDFL 96
5.5 Conclusions 96
Chapter 6: Conclusions and Future Work 97
6.1 Chapter 3 (Design, cavity and temperature considerations for TDFLs) 98
6.2 Chapter 4 (Development of a high power TDFL) 98
6.3 Chapter 5 (Development of a Q-switched TDFL) 99
References 99
Appendix A: Supplementary Mathematics 104
Appendix B: Component specification 107
Appendix C: Parameter settings 109

List of figures

Figure 1: (a) Light propagation through a cylindrical glass rod with no cladding and (b) with a cladding. 2
Figure 2: Simple diagrams illustrating light interaction with matter. (a) illustrates photon absorption, (b), spontaneous emission and (c), stimulated emission. 4
Figure 3: Simple optical cavity consisting of two parallel mirrors. 5
Figure 4 : Illustration of a single round trip within a simple two dimensional optical cavity. 6
Figure 5: (a) Pumping of a gain material with no optical cavity. (b) The effect of introducing an optical cavity with insufficient pumping to induce laser action. (c) With sufficient pumping, laser action is induced. 6
Figure 6: Simplified energy level diagrams depicting (left) a 3-level system and (right) a 4-level system. 8
Figure 7: (a) A simple 3-level energy diagram for thulium and (b-e) simplified diagrams of inter- 9
Figure 8 : Absorption spectra for thulium with simplified energy diagram [23]. 9
Figure 9: Slope efficiencies measured for cladding-pumped TDFL with a 805 nm laser diode [21] 11
Figure 10: Graph of transmission losses in silica fibre [20] 12
Figure 11: A simplified energy diagram depicting the pair-induced quenching effect [32]. 13
Figure 12: Atmospheric transmission spectra (left) in the 1.5 to 2 µm wavelength range and (right) the 2 to 2.5 µm wavelength range [36]. 14
Figure 13: Ray of light passing through a simple step index fibre. 16
Figure 14: Calculated modes for a step index fibre with a NA of 0.09 and core radius of 12.5 µm. .. 17
Figure 15: Comparison of single mode beam diameters (grey circles) with respect to normalised core diameters for a (left) LMA fibre and (right) single mode fibre. 18
Figure 16: Example of a skew ray and intercepting ray propagating through a cladding pumped fibre with circular cladding geometry. 19
Figure 17: Cross section, excluding the polymer coating, of a Nufern 25/400 thulium-doped fibre showing the core and pedestal dimensions [44]. 20
Figure 18: (a) Shows a typical setup for a M^2 measurement done in this dissertation. (b) Illustrates some important parameters concerning Gaussian beams. 22
Figure 19: Potential longitudinal modes for an arbitrary fibre laser in the frequency domain. 23
Figure 20: Simplified, schematic illustration of Q-switching population dynamics and laser signal pulse generation when pulse pumped. 24
Figure 21: Fibre tip soaking in acetone. 32
Figure 22: Optical microscope images of the fibre facets at various tension settings performed on a Nufern, LMA 25/400 passive fibre (Table 2). 33
Figure 23: (left) Blade in position to cleave a fibre and (right), the blade / backstop assembly with ingot cover / fibre guide. 33
Figure 24: A clean mirror-like cleave of a LMA 25/400 thulium-doped fibre as used in this dissertation. 34
Figure 25: Microscope image of a 7.8° (90°-82.4°) angle cleaved Nufern 25/400 passive fibre. 35

Figure 26: Output wavelengths for the FCLD at various pump powers. 36
Figure 27: The complete pump assembly with a simple diagram illustrating the coupling of pump light into a target fibre through a dichroic mirror (input coupler). 37
Figure 28: Graph of the measured coupling efficiency. 37
Figure 29: Various laser design configurations for the cw TDFLs developed in this dissertation. 39
Figure 30: The TDFL set up in configuration 3 with the cooling fans and intracavity VBG in place. 40
Figure 31: Laser output powers as a function of incident pump power for various output couplers butted against the flat cleave output. 41
Figure 32: Spectral output for of the short fibre laser with various output couplers at 43.5 W of incident pump power. 42
Figure 33: Plot of the residual pump power measured against the launched pump power. 42
Figure 34: A time series of sequential spectral measurements (T1 through T4) measured at arbitrary time intervals 43
Figure 35: Slope efficiencies for the air cooled and uncooled laser with an intracavity high reflector mirror and VBG. 45
Figure 36: Typical self-pulsing pulse train observable at 1.17 times the laser threshold incident pump power. 45
Figure 37: Temporal stability for the air cooled (blue) and uncooled (red) laser with an intracavity high reflector at 43.5 W of incident pump power. 46
Figure 38: Temporal stability for the air cooled (blue) and uncooled (red) laser with an intracavity VBG at 43.5 W of incident pump power. 47
Figure 39: Output laser spectra for the air cooled and uncooled system with an intracavity high reflecting mirror and VBG at 43.5 W of pump power. 48
Figure 40: Second order polynomial fit for beam quality factor measurement performed for the air cooled TDFL in configuration 3 with an intracavity VBG. 50
Figure 41: Profile of the beam waist of the air cooled TDFL in configuration 3 with an intracavity VBG at 60 W of pump power and 6.6 W of laser output power. 51
Figure 42: (left) CAD rendering of the assembled copper fibre holder with rounded end and water cooling channel. (right) Disassembled view. 53
Figure 43: CAD rendering of the cooling scheme implemented in the development of the high power TDFL. 54
Figure 44: Laser output power at various current and chiller temperature settings. 54
Figure 45: Laser configuration for testing the thermal load limits of the TDFL fibre tip. 55
Figure 46: Thermally induced damage of the TDFL tip without splices at approximately 56 W of pump power. 56
Figure 47: (from left to right, top to bottom) Time sequence images of the splicing of two mode-matched passive fibres for a rough splice optimisation. (f) A successful splice is achieved. 58
Figure 48: An unsuccessful splice for the “rough” optimisation. The fibre edges are parallel, however fusion at splice joint visible as a seam within the yellow ellipse, was unacceptable. 59
Figure 49: Splice program and relevant spice parameters used for the successful splice in the “rough” splice optimisation process. 60
Figure 50: Fibre orientation for the fine splice optimisation measurements. 61

Figure 51: Unsuccessful splice attempt at a high arc power set point. 61
Figure 52: Laser slope efficiency measurements for the fine splice optimisation. 62
Figure 53: Illustration of the modified cleaving technique specifically devised for this work to minimise the loss of doped fibre in a splice between a doped and a passive fibre. 62
Figure 54: (left) Silver based, thermal paste applied into the holders, and (right) the complete cooling system. 63
Figure 55: The various TDFL configurations used in the development of the high power cw TDFL. ... 64
Figure 56: (left) Illustration of core misalignment and (right) thermal mismatching of the MFD, both of which initiate cladding modes in a fibre laser. 65
Figure 57: Simplistic representation of a chemically etched, cladding mode stripper scattering cladding light at the surface of the fibre cladding. 65
Figure 58: Tm-doped fibre spliced to two lengths of passive fibre, in configuration 3. 66
Figure 59: Comparative slope efficiencies for several reference measurements in the development of the high power cw TDFL with an intracavity HR mirror. 67
Figure 60: With reference to table 5, (top left) measurement 1, (top right) measurement 2, bottom left (measurement 3) and (bottom right) measurement 4 show comparative beam quality factors (M^2) for several measurements during the development of the high power cw TDFL. 68
Figure 61: Beam profiles for various measurements (Ref) in the development of a high power cw TDFL. 69
Figure 62: Screen shots recorded by the oscilloscope (@1 μs/div) for (left) 2.9 W and (right) 4.8 W of laser output power respectively. 70
Figure 63: (lower traces) Single, periodic, pulse envelope as seen on the output of the 3.7 m TDFL at low output powers (6.8 W and 10.9 W). (upper traces) An expanded view of the low output power pulse envelope. The dotted lines represent the laser off (zero signal) baselines. 71
Figure 64: Screen shot recorded by the oscilloscope (@100 ns/div) for 50 W of laser output power. 71
Figure 65 : (upper traces) Comparison of the periodic modulation of the TDFLs continuous wave output at high laser output powers and, (lower traces) the modulated pulse envelope at low laser output powers. 72
Figure 66: (left) Position of the HR mirror with respect to the passive fibre's angle cleaved input coupler. (right) After placement of the 2036.1 nm VBG between the HR mirror and input coupler. . 73
Figure 67: Slope efficiencies of the TDFL with various intracavity elements including a HR mirror, 1939.8 nm VBG and a 2036.1 nm VBG. 74
Figure 68: Measurements for the beam quality factor determination of the high power TDFL with an intracavity 2036.1 nm VBG. 74
Figure 69: Beam profiles for the 3.7 m TDFL showing (a) the intracavity ASE signal and far field output signals for (b) a 1939.8 nm VBG and (c) a 2036.1 nm VBG. 75
Figure 70: Spectroscopy of the 3.7 m TDFL with an intracavity HR mirror, 1939.8 nm VBG and 2036.1 nm VBG. 76
Figure 71: (left) Output stability the 3.7 m TDFL with an intracavity 1939.8 nm VBG at low power (@ 500 ns/division), (middle) high power (@ 20 ns/division)and (right) with an intracavity 2036.1 nm VBG at high power (@ 50 ns/division). 76

Figure 72: Colour coded cross section (Table 7) of the PM 25/400 TDF used in the development of the Q-switched TDFL. 79
Figure 73: Fibre facet after the successful cleaving of the PM 25/400 TDF. 80
Figure 74: Respective coupling efficiencies for the two pump diodes used in the development of the Q-switched TDFL. 81
Figure 75: Schematic of the q-switched TDFL with a bi-directional pumping scheme. 83
Figure 76: (top left, right) The AOM's adjustable azimuthal and elevation stages and (right) the dry air box with sealed bag for adjusting. 84
Figure 77: Photograph of the Q-switched TDFL highlighting some important laser components. 84
Figure 78: Slope efficiencies of the cw laser output (vertically polarised) for the PM TDF. Polarised laser output was first induced with a PBS (unidirectional pumping). Polarisation was later induced by a Brewster angled AOM which replaced the PBS. Efficiency measurements with the intracavity AOM were performed with unidirectional and bidirectional pumping schemes. 85
Figure 79: Comparison between the cw laser output slope efficiencies with an intracavity PBS and the total unpolarised laser output. 86
Figure 80: Ratio of vertically polarised to total laser output power on rotation of a HWP between the TDFL and a fixed thin film polariser. The AOM was the intracavity polarising element. 86
Figure 81: (upper trace) Output stability of the cw laser output with bidirectional pumping and, (lower trace) unidirectional pumping of the PM TDFL. The traces were recorded over a 20 µs interval (@ 2 µs/division) with 14 W of average laser output power. 87
Figure 82: Screen shots recorded by the oscilloscope at laser output powers (upper trace) 4.7W (@ 500 ns/division), (middle trace) 14 W (@ 2 µs/division) and (lower trace) 17.8 W (@ 1 µs/division)of laser output power with a bidirectional pumping scheme. The frequency of the modulated cw output was measured to have a frequency of ~3.8 MHz for all three traces. 87
Figure 83: Slope efficiency of the q-switched PM TDFL at various pulse repetition rates. 89
Figure 84: (top) Stable Q-switching of the TDFL before (50 µs/division) and (middle) observed post pulsing before temporal destabilisation of the laser output at 50 kHz PRF (100 µs/division). (bottom) Post pulsing before the onset of temporal instability at 25 kHz PRF (100 µs/division). 89
Figure 85: Plot of the pulse energy and average laser power as functions of pulse repetition frequency. 90
Figure 86: Pulse energy and pulse length curves at 37.5 KHz (pulse skipping at 75 kHz) and 75 kHz (every pulse). 91
Figure 87: The DCFDG voltage (blue trace) and corresponding pump intensity (yellow trace) as recorded by the oscilloscope (@ 100 µs/div). 93
Figure 88: Comparison of the rise and fall times between external analogue and internal digital modulation of the FCLD. 94
Figure 89: Screen shot recorded by the oscilloscope (@ 100 µs/div) illustrating the pulsed TDFL output with gain switching of the FCLD and no Q-switching. 95
Figure 90: Photograph of the oscilloscope screen (@ 100 µs/div) showing the laser output pulses (yellow trace) for the Q-switched TDFL with a gain switched pump. 95
Figure 91: Beam profile of the Q-switched TDFL. 96

Figure 92: Radial plot of $u(r)$ with the proportionality constants γ and k_T chosen such that the function is continuous at $r = a$. *Left,* plot of $u(r)$ with $l = 1$ and *right,* $l = 3$. 106

List of Tables

Table 1: V parameters for LP_{lm} modes for l = 0, 1 and m = 1, 2, 3. 17
Table 2: Table of parameters for some commercial SM and LMA thulium-doped fibres [43]. 19
Table 3: cw and pulsed TDFLs. 27
Table 4: List of commercially available TDFLs in the marketplace 28
Table 5: Correlation between cladding radius and pulse length for three AOM, Q-switched TDFLs. .. 30
Table 6: Summary of measurements in the development of a CW TDFL 69
Table 7: Fibre parameters for the polarization maintaining thulium-doped fibre. 78
Table 8: Maximum average powers, pulse energies and peak pulse powers at the minimum achievable pulse lengths for several pulse repetition frequencies. 91
Table 9: Comparison between components used for the development of the Q-switched TDFL (this work) and that of Willis *et al.* 91
Table 10: Comparison between the performance of the Q-switched TDFL (author) and that of Willis *et al* 92
Table 11: Gooch & Housego AO Q-switch Specifications. 108
Table 12: Gooch & Housego RF driver specifications. 108
Table 13: Optigrate 2036.1 nm VBG specifications. 108
Table 14: Optigrate 1939.8 nm VBG specifications. 109
Table 15: 3SAE LDS splice parameters for LMA Nufern 25/400 passive and TDF. 110
Table 16: Parameter settings for Vytran PTR-200-MRC for recoating a Nufern 25/400 TDF to passive splice 110
Table 17: Parameter setting for 3SAE LCCII cleaver for the various fibres used in this dissertation. 110

List of symbols and abbreviation

c	Speed of light
σ_a	Effective absorption cross-section
σ_e	Effective stimulated emission cross-section
h	Planck's constant
k_B	Boltzmann's constant
M^2	Beam Quality Factor
Tm	Thulium
wt. %	Weight percentage
AC	Angle Cleave
AOM	Acousto Optic Modulator
ASE	Amplified Stimulated Emission
cw	Continuous wave
CR	Cross-Relaxation
DM	Dichroic Mirror
EDFL	Erbium-Doped Fibre Laser
EOM	Electro Optic Modulator
ESA	Excited State Absorption
FBG	Fibre Bragg Grating
FC	Flat Cleave
FCLD	Fibre Coupled Laser Diode
FCMRP	Fibre-Cavity Mirror Reflectivity Products
HR	High Reflector
IR	Infra Red
LIDAR	Light Detection and Ranging
LMA	Large Mode Area
MOPA	Master Oscillator Power Amplifier
NA	Numerical Aperture
OPO	Optical Parametric Oscillator
PCF	Photonic Crystal Fibre
PM	Polarisation Maintaining
PBS	Polarisation Beam Splitter
RPL	Residual Pump Light
SBS	Stimulated Brillouin Scattering
SM	Single Mode
SRS	Stimulated Raman Scattering
TDF	Thulium-Doped Fibre
TDFL	Thulium-Doped Fibre Laser
UV	Ultra Violet
VBG	Volume Bragg Grating
ZGP	$ZnGeP_2$

Chapter 1: Introduction to silica-based thulium-doped fibre lasers (TDFLs)

Overview of the dissertation

Lasers with operating wavelengths in the 2 µm wavelength region have found useful applications in fields such as medical surgery [1,2], light detection and ranging (LIDAR) [3],manufacturing [4], free space propagation [5], and directed infra-red counter measures (DIRCM) [6]. The growing success of TDFLs as sources of 2 µm wavelength radiation can be attributed to their broad tuneability (1850-2100 nm) [5], high slope efficiencies [7], potential for high output power (~1 kW) [8], good beam quality, ease of cooling, and their ability to pump holmium-doped crystals in a variety of crystalline hosts [9,10]. Another advantage of TDFLs over other "eye-safe" (>1400 nm) 2 µm wavelength laser sources such as, erbium-ytterbium-doped fibre lasers and holmium-doped fibre lasers is their ability to be optically pumped with readily available ~790 nm laser diodes. Comparatively, Holmium-doped fibre lasers are often pumped with TDFLs and erbium-ytterbium-doped fibre lasers; when pumped by commercially available diodes have poor slope efficiencies (<45 %)[7].

TDFLs have also been utilised for wavelength generation beyond the 2 µm wavelength range (3-5 µm) by either directly or indirectly pumping $ZnGeP_2$ (ZGP) optical parametric oscillators (OPOs). Laser emission in this wavelength range is applied in fields such as LIDAR and directed missile counter measures (DIRCM). Traditionally, continuous wave (cw) TDFLs pumped Q-switched holmium-doped crystals or fibres [11] which in turn pumped ZGP crystals. However, recently it has been shown that a Q-switched TDFL can directly pump the ZGP crystal for efficient nonlinear wavelength doubling [12].

Direct pumping of a ZGP crystal with a Q-switched TDFL source will lower the overall laser development costs, improve the wall plug efficiency, and simplify the laser architecture; however, there is a drawback. A solid state Ho:YLF amplifier has been demonstrated to deliver high energy pulses in excess of 300 mJ [13]. The pump source for the amplifier and seed source was a Tm:YLF crystal and TDFL respectively. The high pulse energies are in part owing to holmium's large emission cross section, high gain profile, and long upper state lifetime. Q-switched TDFLs on the other hand, like the one that pumped the aforementioned OPO produced pulse energies in the order of µJ's.

To this end three TDFLs were developed in this study: the short "test" TDFL (Chapter 3), the high power cw TDFL (Chapter 4), capable of pumping Holmium crystals and, the Q-switched TDFL (Chapter 5) for pumping ZGP OPOs. The test TDFL served as an experimental platform for gaining insight into TDFL development techniques and laser design considerations. Experimental outcomes and literature studies covered in chapter 3 were then implemented into the development of the high power (63 W), high slope efficiency (~56 %) cw TDFL (Chapter 4). Similarly, experimental

outcomes from chapter 3 and 4 were implemented in the development of the high power (23 W average power), high slope efficiency (~47 %) Q-switched TDFL (Chapter 5).

The chapters to follow (Chapter 1 and Chapter 2) will introduce the necessary background knowledge and fibre theory for the rest of the dissertation.

1.1 Introduction to silica-based optical fibres

The propagation of light in a transparent cylindrical glass rod surrounded by air is illustrated in Figure 1. The refractive index of air, n_2, is approximately 1 and that of glass, n_1, is approximately 1.46. Since $n_2 < n_1$, light rays incident on the glass to air interface at angles greater than the critical angle (θ_c) undergo total internal reflection, that is, virtually all of the light is reflected at the interface and thus propagates along the length of the glass rod. This is shown by the red ray trace. The blue trace illustrates a ray incident on the glass-to-air interface at angles less than θ_c. In this instance the ray undergoes Fresnel reflection at the surface transmitting some of the beam. As a result, the beam is attenuated as it propagates down the glass rod. Early fibre optics had a simple, uncladded, glass to air interface as depicted in Figure 1(a). These fibres were susceptible to surface damage reducing the strength increasing the optical losses of the fibres. This problem was overcome in 1954 by Hopkins, Kapany, and van Heel who reported the first step index fibres. The concept was to surround a class core with a glass cladding of lower refractive index, as illustrated in Figure 1(b).

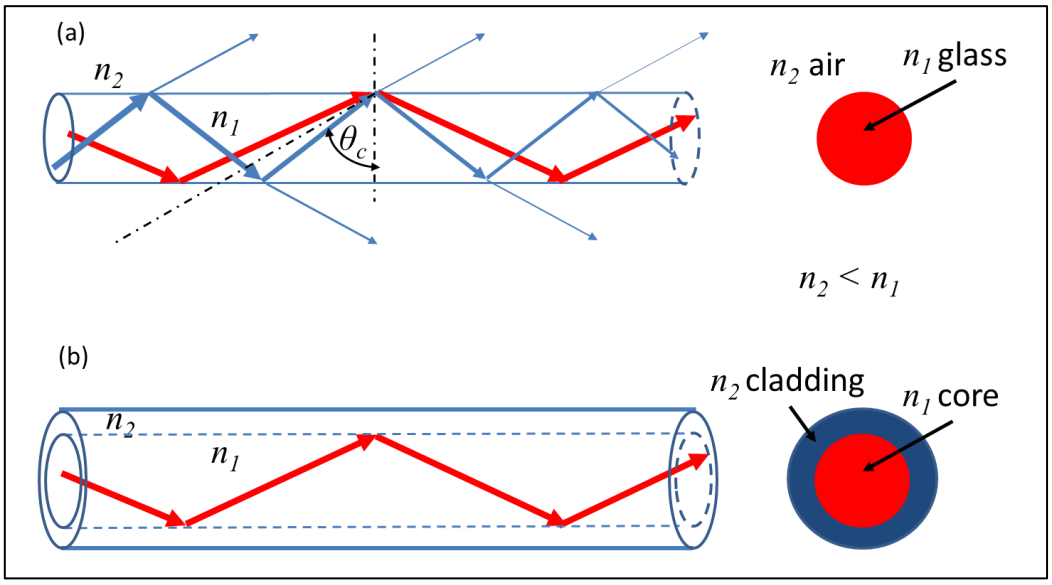

Figure 1: (a) Light propagation through a cylindrical glass rod with no cladding and (b) with a cladding.

The major technological advancement in silica fibres as a means for data transfer came about as a solution to the overwhelmed copper telecommunications networks. Since signal bandwidth is roughly proportional to signal frequency, data transfer using light waves instead of electrical waves is advantageous. Early problems concerning the use of fibre optics for data transfer included, joining

of fibres, glass impurities and multimodal dispersion of the light wave. It was later pointed out in a paper by Charles Kao and George Hockham that choosing a small fibre core with a cladding to core ratio of 100:1 allowed for the propagation of single mode laser light through an optical fibre. This finding, addressed the issue of modal dispersion in optical fibres. Other dispersion effects such as polarisation and chromatic dispersion were not affected by this finding. The paper also reported bending, scattering, and absorption loss measurements for a host of glasses. The paper systematically outlined the feasibility of optical fibres as a means of long distance data propagation and predicted that attenuation in fibre optical cables could be reduced to under 20 dB/km. The year was 1966 and dawn had officially broken on the optical fibre era; in 2009 Kao was awarded a Nobel Prize in physics [14,15].

Modern telecoms uses amorphous silica-based fibre due to silica's high tensile strength, low loss transmission windows (particularly at ~1500 nm wavelengths), low nonlinearity and hygroscopic behaviour, to mention a few [16]. Joining techniques such as cleaving (cutting) and splicing (fusing together) have been extensively developed, as well as reducing impurities in the silica glass. These developments stemming from the telecommunications industry has resulted in fibre optics being the dominant means of propagating data over long distances with extensive networks the world over [14].

1.2 Absorption, stimulated and spontaneous emission

Laser is an acronym for Light Amplification through Stimulated Emission of Radiation and was first predicted by Albert Einstein in 1917 [17]. Einstein's *theoretical* model was a simple two level laser system which worked as follows:

Consider three ways in which light can interact with matter, namely absorption, stimulated emission and spontaneous emission (Figure 2). Suppose a photon with energy $E_p = h\nu$, where h is Planck's constant and ν is frequency, is incident on an atom with its electron initially in some low energy manifold E_l. There is a probability that the photon can excite the electron directly into a higher energy manifold E_u provided E_p = (E_u - E_l), the energy difference between the two manifolds. This process is illustrated in Figure 2(a) and is known as absorption. After absorption has occurred, there are two direct routes for de-excitation of the excited electron from the E_u manifold back to the lower energy manifold E_l namely stimulated emission and spontaneous emission. Stimulated emission occurs if a photon with energy E_p = (E_u - E_l), from any direction, is incident on the already excited atom. When this happens there exists a probability that the incoming photon will cause (stimulate) a de-excitation of the atom resulting in the emission of two photons as illustrated in Figure 2(b). A special property of stimulated emission is that the stimulated photon will inherit the same phase, direction and energy as the incident photon. If no stimulated emission occurs, the excited electron will spontaneous decay back to the lower energy manifold emitting a photon in a random direction. This process is known as spontaneous emission and is shown in Figure 2(c). The average time it takes for an electron to spontaneously decay is given by τ_{ul}, the upper state lifetime.

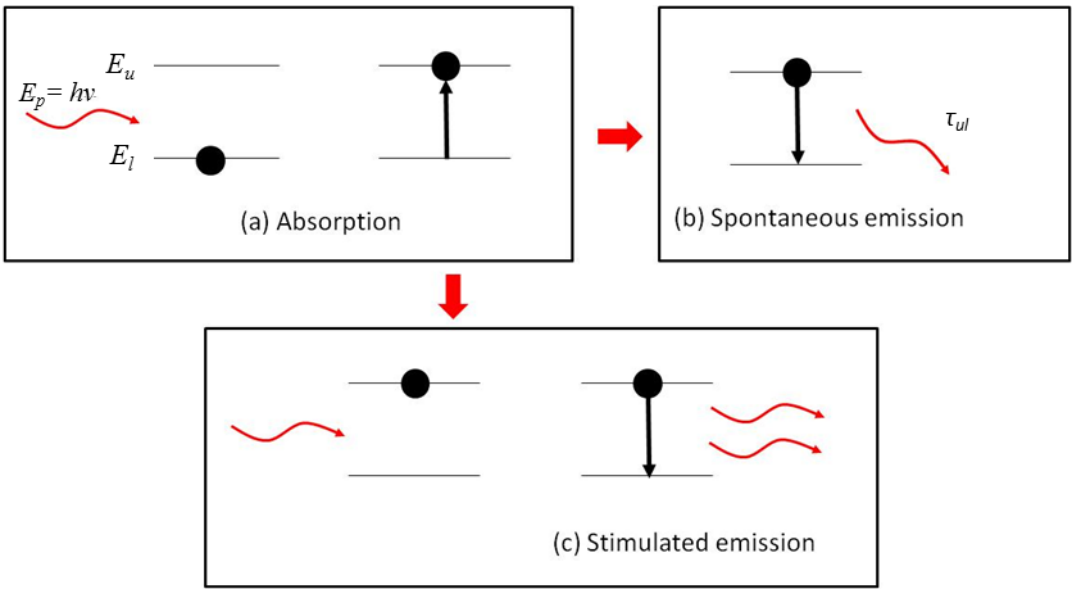

Figure 2: Simple diagrams illustrating light interaction with matter. (a) illustrates photon absorption, (b), spontaneous emission and (c), stimulated emission.

1.3 Basic laser concepts

If we now consider an ensemble of atoms such as in a crystal (gain material), then the goal of building a laser would be to promote stimulated emission processes as follows:

1) Excite as many electrons to the upper energy manifold to promote stimulated emission,
2) amplify the stimulated emission and reduce spontaneous emission,
3) reduce re-absorption and losses to the amplified stimulated emission beam.

The rate of stimulated emission is proportional to the number of atoms with electrons in the upper energy manifold, and the rate of absorption is proportional to the number of atoms with electrons in the lower energy manifold. Let these populations be N_u and N_l respectively. Promotion of N_u, essentially promotes stimulated emission. **Therefore the first condition for laser action is a population inversion, that is,** $N_u > N_l$. One method of increasing the upper state population is to expose the gain material to intense light of the appropriate wavelength supplied by some light source. The name of such a source is a pump source and the light it supplies, pump light. Optical pump light sources include laser diodes and flash lamps to name a few.

Stimulated emission can be amplified (promoted) and spontaneous emission reduced with the introduction of an optical cavity, also known as an optical resonator. An optical cavity essentially provides optical feedback for amplification by reflecting light back and forth along repeatable fixed paths. Figure 3 illustrates a simple optical cavity consisting of two parallel mirrors, one highly reflecting and the other partially reflecting.

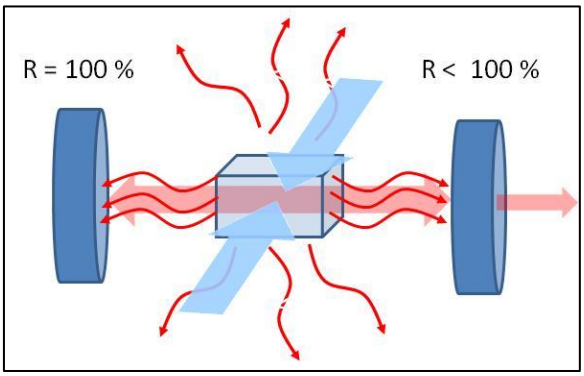

Figure 3: Simple optical cavity consisting of two parallel mirrors.

The blue arrows in Figure 3 represent pump light. The amplification process works as follows: Initially there is spontaneous emission of photons in random directions, some of these within the confines of the optical cavity. Such photons on average will make multiple passes through the gain material before exiting the optical cavity. Photons not contained on repeatable paths within the cavity will experience less gain or no gain at all. The intracavity photons will constantly stimulate emissions from newly excited electrons, afforded by the continual pumping of the gain material, thus amplifying the stimulated emission process along the optical paths governed by the optical cavity. The amount of amplification the stimulated emission signal experiences after one round trip is known as the round trip gain. In reality there will be cavity losses which includes scattering, reflectivity losses and fluorescence losses to name a few [18]. **This brings about a second condition for laser action to occur, that is, the round trip gain must exceed the round trip optical losses**. An example of a round trip within a two dimensional optical cavity is illustrated in Figure 4.

Amplification of stimulated emission within the optical cavity will increasingly depopulate the upper energy manifold until equilibrium is established. Once equilibrium has been achieved the laser is said be in a steady state since the output is stable. Under these conditions the laser will supply a continuous stream of laser photons. Such laser operation is known as continuous wave (cw).

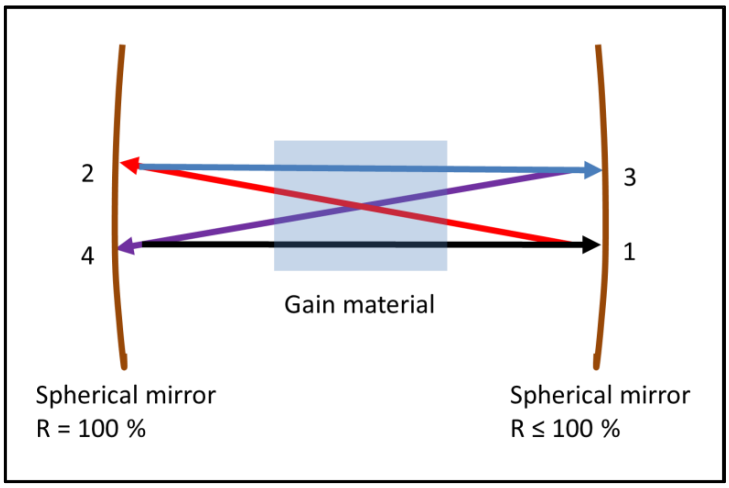

Figure 4 : Illustration of a single round trip within a simple two dimensional optical cavity.

Figure 5 illustrates how an optical cavity promotes stimulated emission. Figure 5(a) is an illustration of a weakly pumped crystal with no optical cavity. The thin red lines in the figure represent emissions from the crystal. In such a scenario, spontaneous emission dominates as there is little population inversion (thin red lines) and the crystal is said to fluoresce. Increasing the pump intensity increases population inversion and therefore stimulated emission in the crystal. This scenario is illustrated in Figure 5(b). With no feedback mechanism, the randomly directed spontaneous emissions are amplified stimulated emission by the gain material. This weak, incoherent laser signal is known as amplified spontaneous emission (ASE). Since fibre lasers are long, single pass ASE signal can be particularly intense. Under these circumstances, fluorescence will also increase. Introduction of an optical feedback mechanism (optical cavity) is illustrated in Figure 5(c). In this scenario, provided the round trip gain exceeds the round trip losses, laser action will be induced. The output laser beam will be directional, have a high degree of coherence and be monochromatic.

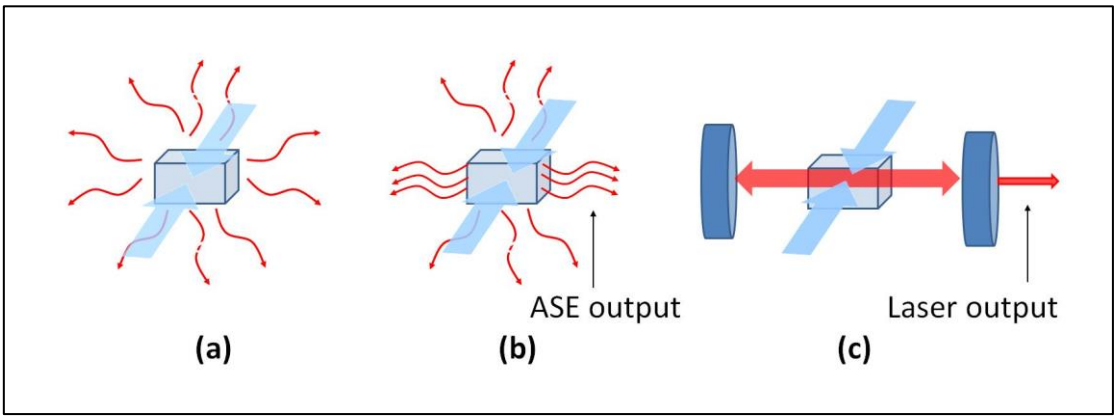

Figure 5: (a) Pumping of a gain material with no optical cavity. (b) The effect of introducing an optical cavity with insufficient pumping to induce laser action. (c) With sufficient pumping, laser action is induced.

For an ensemble of atoms within a gain material, the absorption and emission probabilities can be expressed by the absorption and emission cross sections respectively. The unit of measurement for these cross sections is area. The round trip gain, also known as the small signal gain, can be expressed in terms of the emission and absorption cross sections by

$$g_0(z,\nu) = \sigma_a(\nu)N_l(z) - \sigma_e(\nu)N_u(z) \ldots(1)$$

where σ_a and σ_e are the effective absorption and emission cross sections, respectively, and N_l and N_u are the total electron populations of the lower and upper energy manifolds relevant to the laser emission. The upper and lower energy manifolds will henceforth be referred to as the upper and lower laser levels. The method for solving Equation 1 is reported in a paper by Hanna [19].

So far only a *theoretical* two level system has been discussed, however such systems do not exist in reality. This is because in a true 2-level system, absorption and stimulated emission processes promote one another and thus a population inversion cannot be achieved [18]. Real laser systems are either 3-level, 4-level, quasi 3-level or quasi 4-level. For a three level system, as illustrated in Figure 6(left), pump light excites electrons to the pump manifold p. The electron then quickly undergoes non-radiative (phonon decay as heat) to the upper laser level. The upper level laser lifetime is significantly longer than the pump manifold lifetime and the energy gap between the two levels is large enough such that incoming pump light cannot stimulate emissions from the upper laser level. Electrons in the upper laser level return to the lower laser level via emission of a photon. Provided the pump light is intense enough, in a three level system a population inversion can occur. However, in a true 3-level system since the lower laser level and the ground state electron level g are the same, at least 50 % of the ground state electrons must be pumped into the upper laser level for population inversion to occur. 4-level systems, as illustrated in Figure 6(right) don't have this requirement. The lower laser level is high enough above the ground state level such that after fast non-radiative decay the level is essentially always empty. Thus population inversion occurs at much lower pump levels. 3-level systems are also prone to reabsorption of the laser signal.

For some gain materials there is significant Stark splitting of the ground level manifold. When an ion is perturbed by a local electric field, the energy levels of the ion can be shifted or split. This phenomenon is known as the Stark effect. Since glass hosts are inhomogeneous, the local electric field experienced by each ion as a result of surrounding atoms is random, causing inhomogeneous broadening of the energy level [18]. The ground level is thus made up of many sublevels. For Quasi 3-level systems the uppermost sublevel is the lower laser level. Supposing there is strong coupling between the sublevels due to non-radiative decay and the energy difference between the lower laser level and the ground level is approximately $k_B T$, where k_B is Boltzmann's constant and T is the temperature. Under these conditions the sublevels will always be in thermal equilibrium with each other and hence electrons will always be present in the lower laser level. Since the lower laser level is populated at any given time, there is always potential for reabsorption. Also, the pump intensity required for population inversion will be higher than 4-level systems-but lower than 3-level systems. Quasi 3-level systems are therefore something in-between. Quasi-4 level systems are similar to quasi 3-level systems in that they also have a ground level with many sublevels, however, the energy gap

between the lower laser level and the ground level is high enough such that the lower laser level is almost always empty. To minimise reabsorption losses, a suitable gain and host material must be chosen.

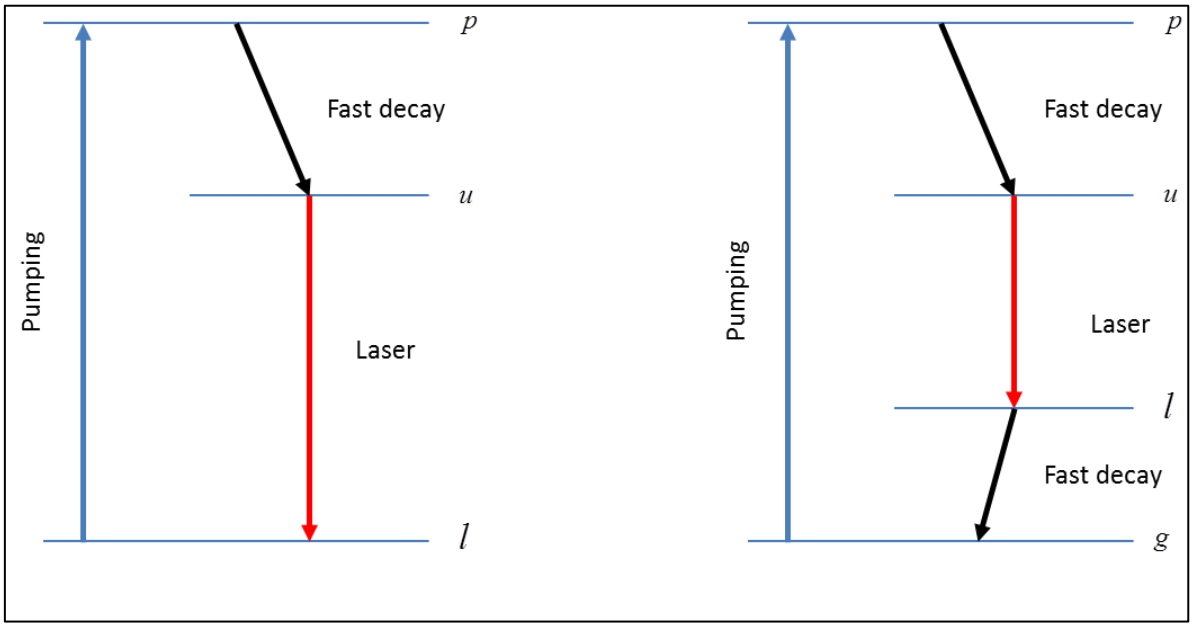

Figure 6: Simplified energy level diagrams depicting (left) a 3-level system and (right) a 4-level system.

1.4 Energy transfer mechanisms between rare-earth ions

Rare-earth ions are predisposed to ion-ion interactions. These interionic interactions are crucial to TDFL performance. The study of rare-earth interionic interactions has been studied in Erbium-doped fibre laser (EDFL) research [20]. Similar models with slight modifications have been explored in TDFL research [21]. There are four inter-ionic energy transfer mechanisms relevant to this dissertation, namely, co-operative upconversion, energy migration, cross-relaxation (CR) and excited state absorption (ESA)[20]. Figure 7 shows simple energy transfer diagrams between two thulium ions. The relevant energy manifolds are shown in Figure 7(a). These energy transfer mechanisms are also relevant to other paired, rare-earth ions like holmium and erbium. They can also be generalised to co-doping regimes where the sensitiser ion (ion transferring energy) is different from the activator ion (ion receiving energy) as in thulium-holmium co-doped systems [22]. In this dissertation we will be looking exclusively at paired thulium ion (Th^{3+}- Th^{3+}) interactions.

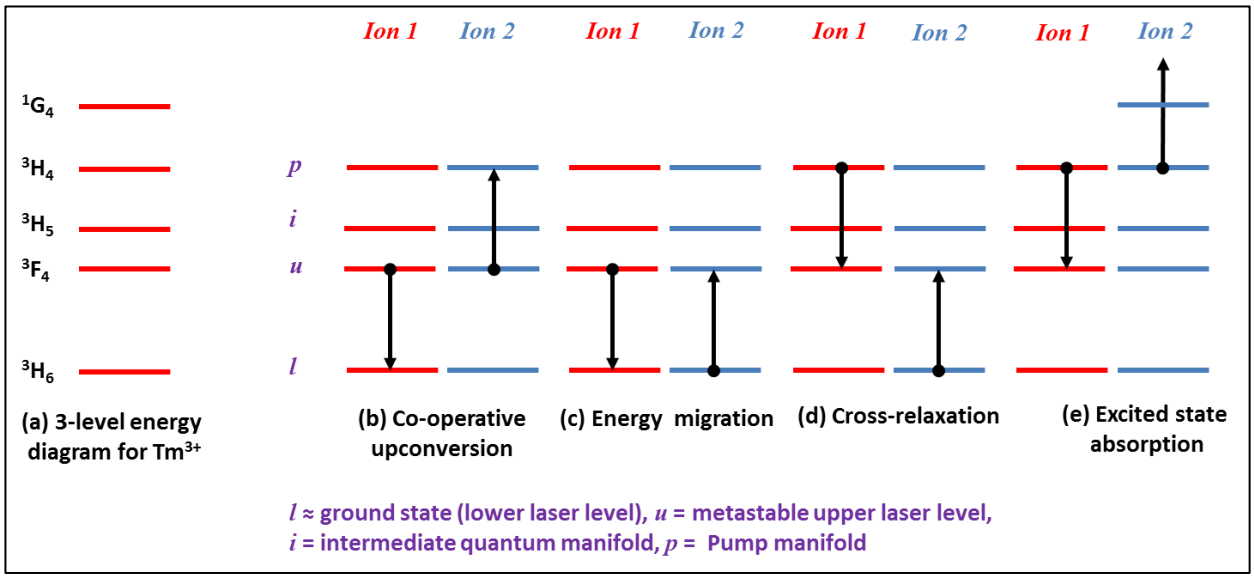

Figure 7: (a) A simple 3-level energy diagram for thulium and (b-e) simplified diagrams of inter-ionic energy transfer mechanism between two Tm^{3+} ions.

The complete absorption spectra for Tm^{3+} doped glass with the relevant energy manifolds are illustrated in Figure 8 [23].

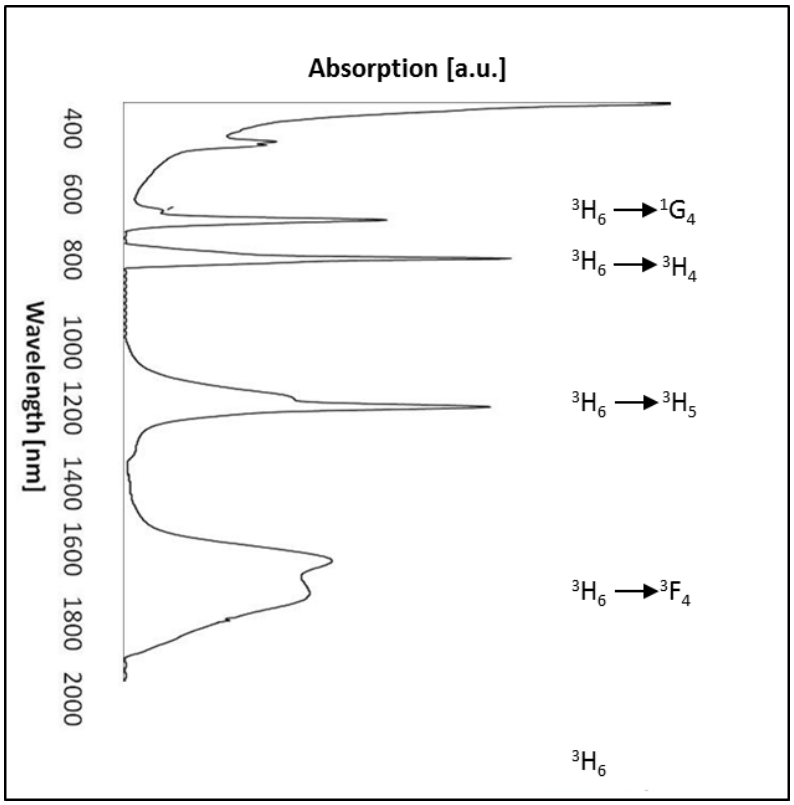

Figure 8 : Absorption spectra for thulium with simplified energy diagram [23].

Analysis of Figure 8 indicates that pumping of electrons to the $^3F_4$ energy manifold is possible at pump wavelengths of 1200 and 1699 nm. However, there are no commercial pump diodes available at the 1200 nm and 1600 nm absorption peaks; instead, complex laser systems would need to be developed for emission at these wavelengths.

Reported optical pumping wavelengths for TDFLs include, ~1904 nm, 1550 nm and 793 nm. For 1904 and 1550 nm pumping schemes, electrons are pumped directly into the metastable $^3F_4$ upper laser level with reported slope efficiencies of >90 % [24] and 60 % [25] respectively. The large difference in slope efficiencies between the two pumping wavelengths is due to their different quantum defects. Quantum defect is the difference in energy between the pump photon and the emitted laser photon (*quantum defect* = hv_{pump}-$hv_{emitted}$). For the 1904 nm pumped laser, the emission wavelength is 1994 nm which is relatively close to the pump wavelength of 1908 nm. Relaxation, in the form of multi-phonon decay from the pump level, through the Stark-broadened upper lasing level ($^3H_4$), is therefore small compared to the multi-phonon decay from the 1550 nm pump level to the 1940 nm laser level of the in-band pumped laser. Multi-phonon decay is emitted as heat making low quantum defect lasers attractive for scaling to high powers. However, due to lack of commercially available high power pump diodes at these absorption wavelengths, in-band and resonantly pumped TDFLs are impractical. Instead, the highest reported powers (1 kW) from TDFLs are optically pumped by laser diodes in the 790 nm absorption band.

793 nm pumped TDFLs have a poor quantum defect. This is however offset by their high quantum efficiencies. Quantum efficiency is the ratio of absorbed pump photons to emitted photons. By pumping thulium with ~793 nm light, electrons are pumped to the upper energy manifold Figure 7(d). A dipole-dipole, dipole-quadrupole or quadrupole-quadrupole interaction between two ions can potentially facilitate cross-relaxation (CR). The result of cross-relaxation is two photons are emitted for a single pump photon resulting in a theoretical quantum efficiency limit of 2. This high quantum efficiency offsets the poor quantum defect of 793 nm pumped TDFLs. Cross relaxation as a means to reduce heat and increase quantum efficiencies in TDFLs was proposed by Antipenko in 1987 [16,26] and by the year 2000 a TDFL with slope efficiency (52 %) exceeding the Stokes efficiency limit of thulium (~40 %) was reported [16]. It was later shown by Moulton that CR processes in TDFLs resulted in maximum quantum efficiencies of 1.8 [7].

Since CR is an ion-ion interaction, the probability of two ions interacting is dependent on their separation distance [20]. The efficiency of the CR mechanism is therefore dependent upon the doping concentration. Rare-earth ions tend to cluster making them prone to co-operative upconversion and ESA (Figure 7(b-e)), which are competing mechanisms to CR. To alleviate clustering, silica-based TDFLs are co-doped with aluminium to increase thulium solubility. One explanation for the increased solubility of thulium ions as a result of co-doping with aluminium is as follows: The commonly accepted structure of silica (SiO_2) is a network of tetrahedral units with oxygen as the bridging atom. The strong covalent bonds present in the silica network are responsible for silica's good mechanical strength and thermal properties, however, when introducing rare-earth ions into the silica network, there is a limited amount of non-bridging oxygen atoms to sufficiently coordinate with the rare-earth ions. The rare-earth ions are therefore forced to share non-bridging

oxygen atoms causing them to cluster. By introducing atoms such as aluminium which are larger than the basic silica network, bridging bonds are broken effectively increasing the number of non-bridging oxygen atoms the rare earth ion can coordinate with. This in turn increases the solubility of the rare-earth ion in silica which therefore reduces clustering [27].

Optimisation of the aluminium co-dopant as well as the thulium doping concentration resulted in the highest reported slope efficiency (74 %) for a diode pumped TDFL by Jackson in 2004 [21]. Figure 9 from the paper by Jackson illustrates the increase of slope efficiency η_s with increased doping concentration. The 74 % slope efficiency was reported for a Tm^{3+} doping concentration of 1.8 wt. %.

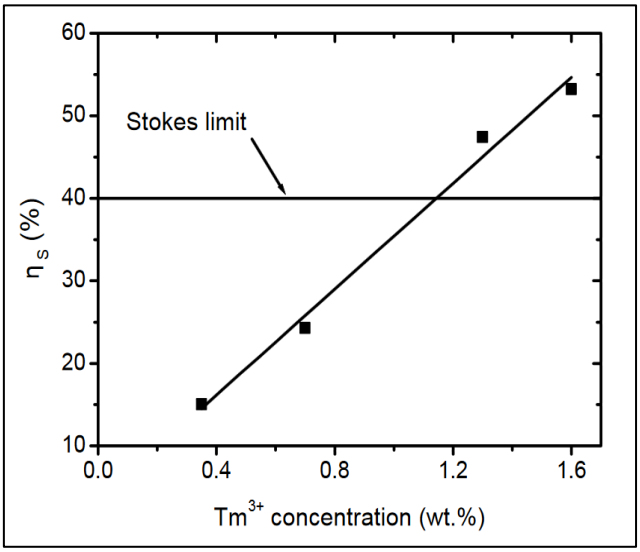

Figure 9: Slope efficiencies measured for cladding-pumped TDFL with a 805 nm laser diode [21].

Commercially available TDF's typically have doping concentrations of 4.wt % [28]. The high doping concentration increases the fibres absorption per metre whilst facilitating CR. Another benefit of diode pumping at ~793 nm is reduced photodarkening. Photodarkening is the degradation of silica host material due to prolonged exposure to UV light. TDFLs emit a blue fluorescence (470 nm) under pumping with 793 nm diode lasers due to ESA or co-operative upconversion of electrons to the $^1G_4$ energy level Figure 7(e). Prolonged exposure to this blue fluorescence would normally lead to photodarkening. However, since the non-radiative interactions involved in CR are faster than radiative processes from the $^3H_4$ energy manifold, its upper state lifetime is significantly reduced. This depopulation of the $^3H_4$ reduces the probability of upconversion processes which lead to photodarkening. It was shown for a 20 W, 1900 nm TDFL that optimisation of thulium doping concentrations (~4.6 wt.%) assisting CR processes, led to silica host degradation of less than 10 % over 10000 hours [29].

High Tm^{3+} doping concentrations, increases the probability of co-operative upconversion and ESA. Electrons excited to higher energy level by ESA or co-operative upconversion normally relax to the metastable $^3H_4$ laser level via phonon radiation (heat) or fluorescence at a non-laser wavelength. Both ESA and co-operative upconversion are therefore loss mechanisms due to two pump photons

resulting in one emitted laser photon. Silica-based TDFLs, due to silica's high phonon energy, are susceptible to non-radiative phonon decay from ESA and co-operative upconversion, the details of which are discussed further in chapter 3.

1.5 Transmission spectra of silica

Much of the technology and understanding of TDFLs stems from erbium-doped fibre laser (EDFL) research. A significant amount of research has been done on EDFL's due to Erbium's 1550 nm emission spectrum overlapping with silica fibres very low loss transmission window. Figure 10 illustrates a spectral loss diagram for silica. The steep rise in the spectral loss diagram towards 2000 nm is partly due to the first overtone vibration of OH^- at 1900 nm [27].

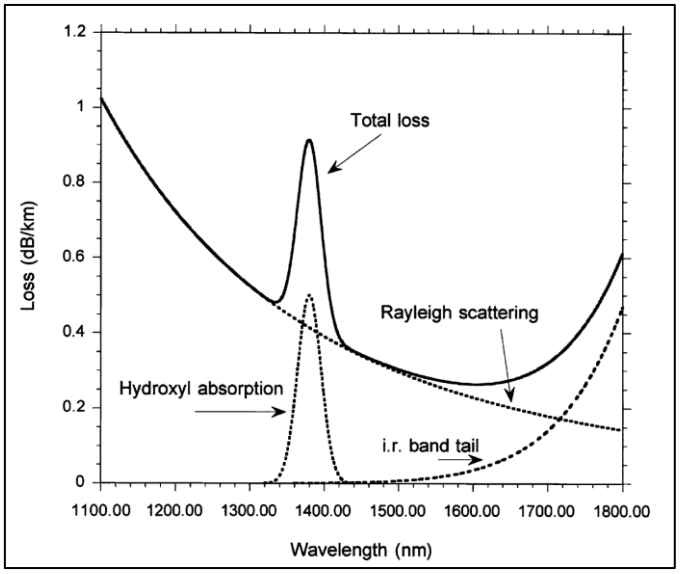

Figure 10: Graph of transmission losses in silica fibre [20].

OH^- ions are introduced into the fibre during production. Since TDFLs typically operate between 1850 nm and 2050 nm, OH^- absorption is a loss mechanism. As a result of OH^- absorption in silicate fibres, alternate "soft glass" hosts such as fluoride, tellurite, and germanate glasses have been tested. Unfortunately, mechanical constraints limit high power scalability in these hosts.

Another motivation for using the "soft glasses" mentioned above is their lower phonon energies. Silicate has phonon energy of approximately 1100 cm^{-1} which is higher than germinate (900 cm^{-1}), tellurite (700 cm^{-1}) and fluoride (500 cm^{-1}) based glasses [30]. Higher phonon energies facilitate unwanted phonon decay processes, potentially reducing laser efficiency and performance and limiting the possible laser transitions to phonon-terminated transitions [16].

1.6 Self-pulsing in TDFLs

The self-pulsing nature of highly doped TDFLs at low pump powers has been reported by several sources in literature [31,32]. The self-pulsing in heavily doped TDFLs and EDFL's for that matter has

similar behaviour to lasers with intra-cavity saturable absorbers [33] where the laser outputs are damped due to relaxation oscillations. As a result, intra-fibre loss mechanisms leading to possible saturable absorber effects have been investigated. It has been shown that clustering or pairing of dopant rare-earth ions such as Er^{3+}, Nd^{3+} and Tm^{3+} within the silica host reduces laser efficiency. To overcome ion clustering (as much as possible) TDF's are co-doped with Al^{3+}. Co-doping with Al^{3+} modifies the silica network increasing absorption of Tm^{3+}. It was reported by Jackson [21], that a ~fivefold increase in Al^{3+}:Tm^{3+} concentration resulted in a fivefold increase in slope efficiency. In a separate paper by Jackson [34] it was shown that bi-directional pumping (both ends) of a TDFL reduced the pump power required for cw output and increased laser slope efficiency, indicating directly that the loss mechanism responsible for saturable absorption is a reabsorption process linked to the unpumped regions of the doped fibre.

One such process is pair-induced quenching [32]. Pair-induced quenching, stated simply, is the inter-ionic energy transfer process between two neighbouring ions both with electrons in the metastable $^3F_4$ upper state laser level. The donor ion transfers its energy to the acceptor ion (upconversion) which rapidly undergoes phonon decay back to the $^3F_4$ upper laser level. The result of this quenching process is the loss of one laser photon. Figure 11 is a simple illustration of this process taken from a theoretical model by El-Sherif and King [32]. In this model, the time evolution of the excited state population dynamics of Tm^{3+} and Tm^{3+} paired ions, as well as ESA processes are considered. Modifications were also made to the emission and absorption cross section ratios, as well as the upper state lifetime of the paired ions. The relaxation oscillation frequency (damped) calculated using this model was close to the measured results. Affects such as heat which also modifies the emission and absorption cross sections[35], was not considered in the model.

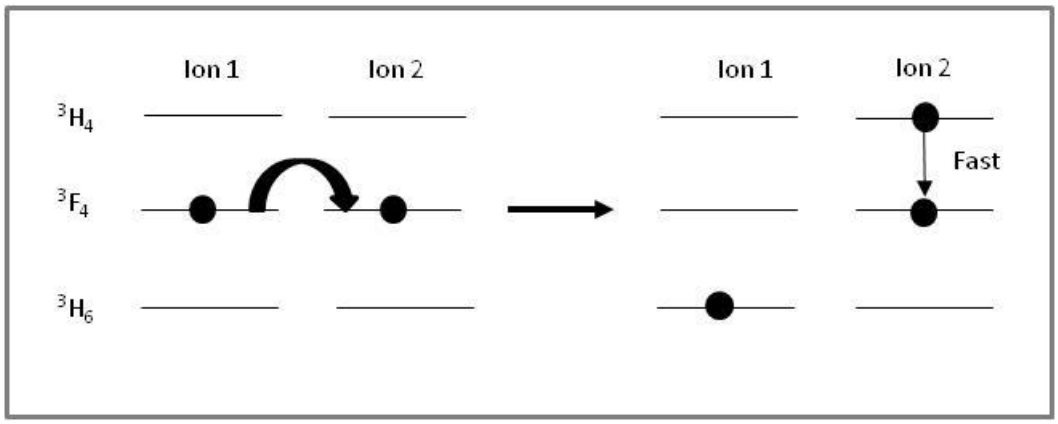

Figure 11: A simplified energy diagram depicting the pair-induced quenching effect [32].

The relationship between quenching processes and phonon cut-off energies is discussed by Kenyon [20] wherein it is states, as a guideline, that if the phonon cut-off energy exceeds 25 % of the band gap energy, the upper state will be completely quenched and therefore depopulated. For 10 % to 25 % ratios, the luminescence lifetime will become temperature dependent and for < 10 %, quenching is negligible. The smallest band gap energy from the $^3H_4$ level to the $^3H_5$ level corresponds to a wavenumber of 4350 cm^{-1} [16]. The phonon energy of silica is approximately 1100 cm^{-1} [30]

which is approximately 25 % of the band gap energy. Accordingly, phonon relaxation and quenching processes from the $^3H_4$ are temperature dependent in TDFLs.

1.7 Wavelength selection

For certain applications a specific laser output wavelength is desirable. For applications such as LIDAR or long distance free space communication, it is essential that the wavelength of the laser radiation be within an atmospheric window. An atmospheric window is wavelengths of the electromagnetic spectrum that be transmitted through the atmosphere with reduced attenuation to the signal strength. Conversely, for some applications such as medical surgery, it may be beneficial that the wavelength coincides with a water absorption line. Figure 1 illustrates a low resolution atmospheric transmission spectrum for radiation in the 1.5 to 2.5 µm wavelength range. From the illustration, there are large atmospheric windows are from ~1.5-1.7 µm and ~2.1 ~2.3 µm wavelength regions.

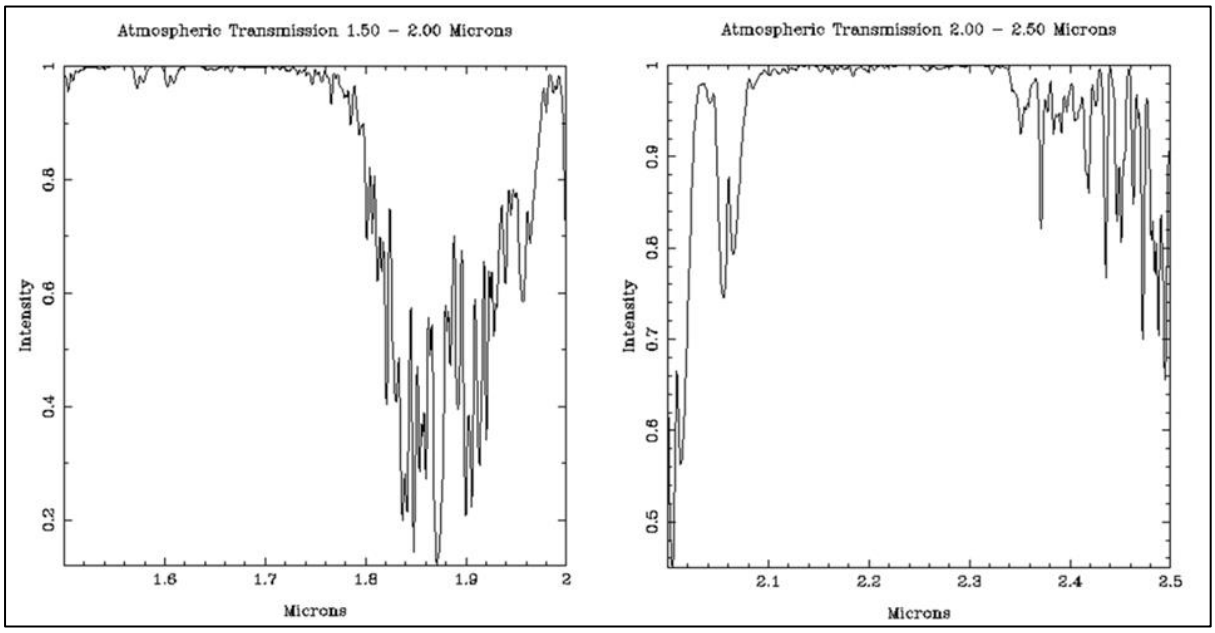

Figure 12: Atmospheric transmission spectra (left) in the 1.5 to 2 µm wavelength range and (right) the 2 to 2.5 µm wavelength range [36].

Wavelength selection in the context of fibre lasers can be achieved with fibre Bragg grating (FBGs) [37] or volume Bragg grating (VBGs)[38]. For this dissertation the focus is on free space coupled Tm-doped fibre lasers and therefore VBGs were implemented.

Chapter 2: Introduction to large mode area (LMA) thulium-doped fibre lasers (TDFLs)

2.1 Introduction

This chapter aims to highlight, by way of theory and discussion, how the physical properties of the TDF influence the expected spatial and temporal behaviour of the TDFL output. Attention is given to both cw and pulsed (Q-switched) regimes which is emphasised in the literature review at the end of the chapter. Technical details and standards regarding beam quality measurements performed in this dissertation are also addressed.

2.2 Numerical aperture (NA)

Figure 13 illustrates a light ray being guided within the core of a step index fibre. For total internal reflection to occur at the core cladding interface, the (angle β) must exceed the critical angle (section 1.1). In this instance, the numerical aperture (NA) for the fibre core is defined as the sine of the maximum acceptance angle (angle α) of a ray incident on the fibre facet such that the ray is guided in the core of the fibre. Mathematically, the NA is given by,

$$NA = \sin(\alpha) = \frac{1}{n_o}\sqrt{n_1^2 - n_2^2} \quad ...(2)$$

where α is the maximum angle at which total internal reflection occurs for a given interface and n_1 is the refractive index of the fibre core, n_2 is the refractive index of the fibre cladding, and n_o is the refractive index of the medium outside of the fibre where $n_1 > n_2 > n_o$. For the case in Figure 13, rays incident on the fibre tip exceeding the NA of the fibre core will decouple into the first cladding.

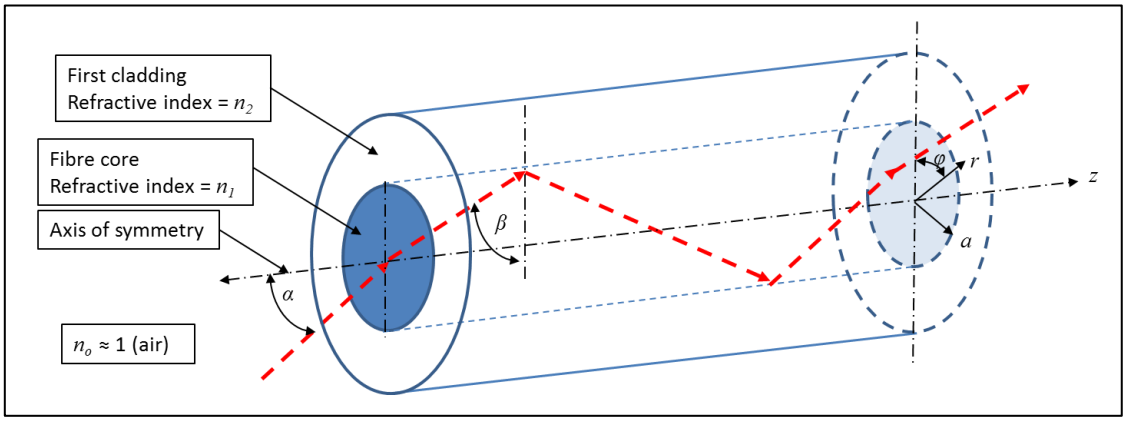

Figure 13: Ray of light passing through a simple step index fibre.

2.3 Transverse modes in optical fibres and the *V* parameter

The transverse spatial distribution of light waves propagating in a step index fibre, as illustrated in Figure 13 can be solved using electromagnetic theory. This is done by solving the electric and magnetic field distributions using Maxwell's equations with the appropriate boundary conditions. It follows from Maxwell's equations that the magnetic and electric field components must satisfy the Helmholtz equation. Equation 3 is the Helmholtz equation expressed in cylindrical coordinates [39]

$$\frac{\partial^2 U}{\partial r^2}+\frac{1}{r}\frac{\partial U}{\partial r}+\frac{1}{r^2}\frac{\partial U^2}{\partial \phi^2}+\frac{\partial^2 U}{\partial z^2}+n^2k^2U=0 \quad ...(3)$$

with $n = n_1$ for the fibre core ($r < a$), and $n = n_2$ for the fibre cladding ($r > a$). The wavenumber $k = 2\pi/\lambda$ where λ is the wavelength of the monochromatic light. $U(r,\varphi,z)$ represents axial components of the electric field (E_z) and magnetic field (H_z). Assuming $U(r,\varphi,z)$ has a periodic azimuthal (φ) dependence, and propagates down the fibre as a travelling wave, it takes on the form $U(r,\varphi,z) = u(r)e^{-jl\varphi}e^{-jz\beta}$ where $u(r)$ is the complex amplitude, l is an integer and β is a propagation constant. By substitution U into Equation 3 and subsequently solving for $u(r)$, the piecewise, spatial distribution of U can be determined for the fibre core and cladding. For more details on solving fibre modes the reader is referred to Appendix A. For this dissertation, it will suffice to focus on the results of the analysis with no loss of continuity.

The spatial distribution (mode structure) of light intensity within a step index fibre is described mathematically by Bessel functions. The mode structure can be approximated by two linearly polarised modes known as LP_{lm} modes. The subscripts l and m are integers that describe the spatial distribution of the mode. The number of modes that will propagate in the core of a particular fibre is proportional to the square of the V parameter (derivation in Appendix A) given by,

$$V = 2\pi \frac{a}{\lambda} NA \ldots (4)$$

where NA is the numerical aperture as defined in Equation 2. Equation 4 reveals important information relevant to optical fibre design. It reveals that a reduction in NA or core diameter (α) reduces the number of modes that can propagate in the core. A V parameter can also be associated with a specific LP mode as in Table 1.

Table 1: V parameters for LP_{lm} modes for l = 0, 1 and m = 1, 2, 3.

	m = 1	m = 2	m = 3
l = 0	0	3.832	7.016
l = 1	2.405	5.520	8.654

For a particular LP mode to be guided within a fibre core, the V parameter associated with that LP mode must be less than the V parameter of the fibre (Equation 3). It is evident from Table 1 that fibres with V parameters less than 2.405 will only guide the LP_{01} mode.

Figure 14 illustrates the calculated modes for a step index fibre with a 25 µm core diameter and 0.09 NA [40] (online calculator), like the fibres used in this dissertation. Due to the weak guidance in fibre optics (because $(n_1 \approx n_2)$, light guided by the fibre is approximately parallel to the fibre axis resulting in longitudinal components of the magnetic field being much weaker than the transverse components. We can therefore approximate the LP_{01} mode in Figure 14 to a Gaussian mode. Modes with a non-zero l numbers, like the LP_{11} in Figure 14 have two linearly independent solutions.

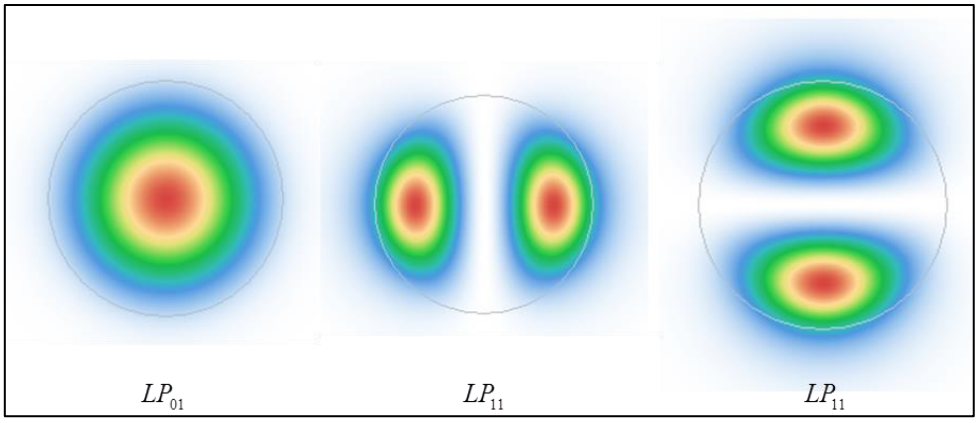

Figure 14: Calculated modes for a step index fibre with a NA of 0.09 and core radius of 12.5 µm.

2.4 Large mode area (LMA) fibres

The lasers presented in this dissertation were developed for high power applications at ~2000 nm output wavelengths. Good beam quality (single mode output) was also essential. In this section the choice of fibre is analysed with respect to power scalability and beam quality.

We firstly consider LMA and single mode fibres. Table 2 lists some important fibre parameters for a few commercial single mode (SM) and LMA fibres. The first parameter of particular importance in this section is the mode field diameter (MFD). The MFD is essentially a measure of beam diameter within a fibre. The single mode, mode field diameter can be estimated using the Marcuse equation,

$$\frac{w}{a} \approx 0.65 + \frac{1.619}{V^{\frac{3}{2}}} + \frac{2.879}{V^{6}} \quad \ldots(5)$$

where w is the mode field radius. Figure 15 illustrates the MFD's for a LMA fibre (left) and a SM fibre (right) [40] where it can be seen that the MFD for the SM fibre is larger than the fibre core.

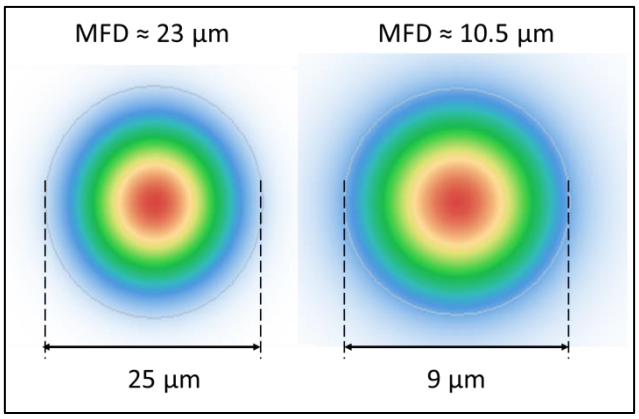

Figure 15: Comparison of single mode beam diameters (grey circles) with respect to normalised core diameters for a (left) LMA fibre and (right) single mode fibre.

Some factors which limit scaling to high powers are [41]:

- Scattering and absorption losses due to fibre imperfections
- Parasitic laser modes and spontaneous amplified emission (ASE)
- Thermal effects such as heating and quenching
- Nonlinear effects such as self-focusing, Raman and Brillouin gain
- Optical breakdown of the silicate host

By increasing the effective mode area of a fibre, as in the case with LMA fibres, light intensity dependent effects such as nonlinear effects, optical breakdown and some thermal effects can be reduced with little compromise to the beam quality.

Another advantage of LMA fibres over most SM fibres for high power scalability is cladding pumping. Comparing the first cladding diameters and the fibre pumping schemes in Table 2, it should be clear that the LMA fibres can be pumped with much higher intensities than SM fibres before "negative" effects are introduced. From an optical breakdown point of view, the 400 µm LMA cladding can support around 494 times higher pump intensity at the fibre tip than the 9 µm SM fibre core. Also, pumping the 0.46 NA cladding allows for pumping with multimode diode lasers. The $NA's$ of typical 793 nm laser diodes are around 0.22 whereas core pumping requires $NA's$ of less than 0.15 (Table

2). Being able to use multimode laser diodes as pump sources reduces pump laser complexity and cost.

Cladding pumping in LMA fibres relies on pump light guided by the fibre cladding intercepting with the active fibre core. As a result the cladding geometry in the LMA fibres listed in Table 2 have octagonal geometries. The octagonal geometry of the LMA fibres assists with directing skew rays propagating through the fibres to intercept the core. The octagonal geometry of the 25/400 LMA fibre can be clearly seen in Figure 17. Figure 16 illustrates a skew ray propagating through a fibre. Other schemes for breaking the symmetry of the cladding include D shaped claddings and off centre cores, to mention a few [42].

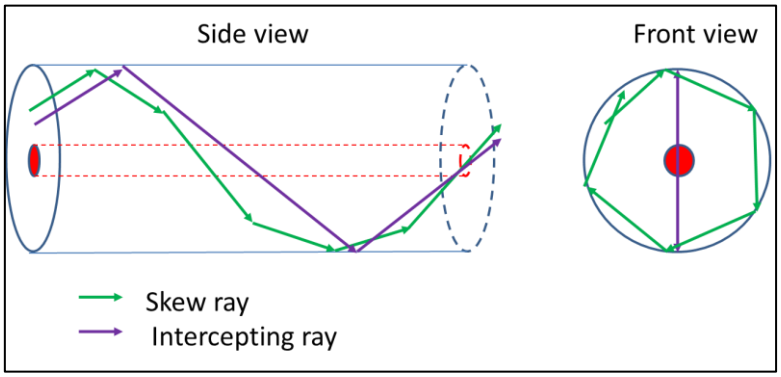

Figure 16: Example of a skew ray and intercepting ray propagating through a cladding pumped fibre with circular cladding geometry.

Table 2: Table of parameters for some commercial SM and LMA thulium-doped fibres [43].

Fibre type	9/125 SM	5.5/125 SM	25/250 LMA	25/400 LMA
Operating wavelength (nm)	1900-2100	1900-2100	1900-2100	1900-2100
Core diameter (µm)	9	5.5	25	25
Outer cladding diameter (µm)	125	125	250	400
Core NA	0.15	0.24	0.09	0.09
Outer cladding NA	NA	NA	≥ 0.46	≥ 0.46
Fibre pumping scheme	Core	Core	Cladding	Cladding
Absorption (dB/m) @ 793 nm	27	340@1560 nm	9.5	1.8
Cladding geometry	Circular	Circular	Octagonal	Octagonal
Number of claddings	1	1	2	2
Cutoff wavelength	~1750	*Unknown	*Unknown	*Unknown
V parameter	*~2.1	*~2.1	*~3.4	*~3.4
Mode field diameter (µm)	10.5	*Unknown	23	23

*= Calculated

The LMA double clad fibres also have a thin cladding (pedestal) around the core with a refractive index only slightly higher than that of the core resulting in the low NA (Equation 1). The NA between the pedestal and the silica cladding needs to be around 0.23 for efficient pump to laser conversion [44]. The double clad design is a good compromise between laser efficiency and near single mode

beam quality and a large single mode, mode field diameter (Equation 5). This is because the increased core size is offset by the lower NA (Equation 4). The NA of some commercial fibre coupled ~793 nm laser diodes is 0.22 which allows for pump light propagation within the fibre pedestal. Figure 17 illustrates a cross section of a Nufern 25/400 LMA thulium-doped fibre, as listed in Table 2. Not shown in Figure 17 is the (~150 µm thick) low index polymer coating which initially surrounds the cladding. The low index polymer coating has three major functions, which are, to protect the inner cladding surface (section 1.1), increase flexibility and ease of handing the otherwise brittle silicate fibre, and to avoid contact and therefore decoupling of light propagating in the fibre.

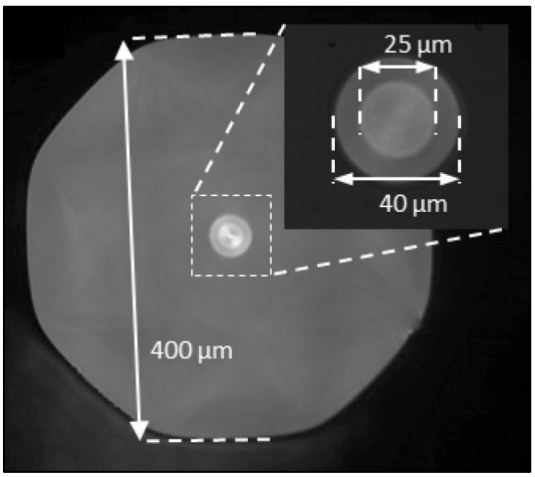

Figure 17: Cross section, excluding the polymer coating, of a Nufern 25/400 thulium-doped fibre showing the core and pedestal dimensions [44].

Thus far, only the benefits of LMA fibres have been discussed. There are however certain drawbacks and challenges relating to fibre laser development with LMA fibres that should be considered. By reducing the NA of the fibre core to offset the potential for multi-modal beam propagation in LMA fibres, fibre bend losses are increased. Single mode fibres are much less prone to bend losses since their NA's are higher (Table 2).Bend loss in fibre lasers is unwanted since it limits how tightly coiled, and therefore how compact the laser can be developed. However, it has been shown that higher order modes are more susceptible to bend losses than lower order modes [45]. The higher order modes illustrated in figure 14 were calculated for a straight (uncoiled) 25/400 LMA fibre (25/400 Table 2). By coiling this fibre to an appropriate diameter, the higher order modes can potentially be suppressed improving beam quality whilst allowing for compact laser design [46].

Another drawback of LMA is their incompatibility with certain laser components. One example of this incompatibility is when an LMA fibre is spliced (joined) to a single mode fibre. Due to the mismatch in mode field diameters of the two fibres, splicing of LMA fibres to SM fibres results in significant optical losses. To minimise the loss, the mode field diameter of the LMA fibre must be modified with an intermediary component such as a mode field adaptor [47]. Another possibility is to use free space optics to couple fibres with mismatched mode field diameters.

LMA fibres generally have higher laser thresholds. This is partly due to the small core diameters in single mode fibres (~10 µm versus ~25 µm) because laser gain increases with pump intensity which is inversely proportional to fibre diameter [48]. There are also limitations to the minimum linewidth achievable with LMA fibres. One explanation for reabsorption in LMA fibre is as follows: Consider Figure 1, the mode field diameter of the single mode fibre extends beyond the core diameter, the opposite is true for LMA fibres. Part of the laser mode in a single mode fibre therefore does not interact with the doped core therefore reducing reabsorption losses [46].

2.5 Beam quality

In this dissertation, beam quality is measured by calculating the beam quality factor (M^2 value) of a given beam. The M^2 is the measure of the far field divergence (spreading) of a real laser beam (measured) relative to that of an ideal Gaussian laser beam with the same waist diameter [49]. Figure 18(b) shows two Gaussian beam traces, a red trace which represents an ideal beam (Gaussian) and a green trace representing a random real beam containing higher order modes. To measure the M^2 of the green trace we need to measure how much more the green beam diverges than our ideal beam if both beams are focused down to a minimum radius (waist) w_0. The divergence angle for our ideal beam is given by θ_1 and for the green trace θ_2. The term Z_R shown for the ideal beam in Figure 18(b) is known as the Rayleigh length. The Rayleigh length is the distance from z_0 where the beam diameter has increased by.$\sqrt{2}$ w_0. From Figure 18(b) it should be clear that the Rayleigh length for the green trace is shorter than z_R due to its higher divergence angle. The Rayleigh length for the ideal beam is given by,

$$z_R = \frac{\pi w_0^2}{\lambda} \quad \text{...(6)}$$

and the M^2 of our green trace is simply the ratio of the two Rayleigh lengths [46],

$$M^2 = \frac{z_R}{z_{Rm}} = \frac{\pi w_0^2}{z_{Rm}\lambda} \quad \text{...(7)}$$

where z_{Rm} is the measured Rayleigh length of the green trace. Pure Gaussian laser beams are called "diffraction limited" because they diverge less, and can be focused to smaller beam diameters than higher order mode beams. For this reason, real laser beams will always have M^2 values greater than or equal to unity. Gaussian laser beams are therefore desirable for many applications such as fine cutting, and materials processing.

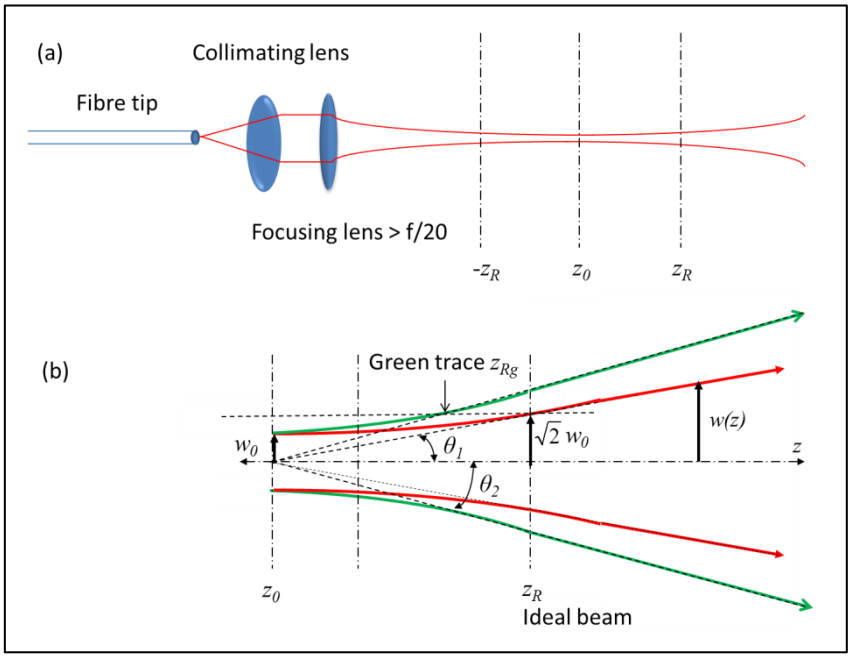

Figure 18: (a) Shows a typical setup for a M^2 measurement done in this dissertation. (b) Illustrates some important parameters concerning Gaussian beams.

M^2 measurements performed for this dissertation were done according to the ISO (International Organisation for Standardisation) standard (11146-1, first edition, 2005) [50]. Figure 18(a) shows a typical setup for a M^2 measurement as done in this dissertation. According to the ISO standard the final lens in the focusing assembly must have an f-number of greater than 20. Also at least 5 measurements must be performed for a minimum of 10 points with a minimum of 5 points between z_0 and $-z_R$ or z_0 and $+z_R$. The remaining 5 points must be measured outside of $-z_R$ and z_R, with an even spread between measurements if possible. The standard also requires that when measurements are performed with a camera, the measured beam diameters should exceed the minimum resolution of the camera. For this dissertation, the Spricon Pyrocam III thermal camera could measure minimum beam diameters of 1 mm. Therefore lenses were selected such that the beam diameters at the beam waist were in excess of 1 mm. Lastly the ISO standard recommends using the second moment (or D4σ method) to measure the beam diameters. This was the method used in this dissertation.

In order to measure the Rayleigh length, a series of measurements must be taken according to the ISO standards mentioned above. These points were then plotted on a graph with the z position on the abscissa and beam radius $(w(z))^2$ on the ordinate. A least squares, second order polynomial fit was then applied to trace out the resulting parabolic curve. Equation 8 can then be applied to calculate the unknowns z_0, w_0 and M^2 or solved directly from the least squares fit with some simple algebra.

$$w(z) = w_0\sqrt{1+\left(\frac{M^2\lambda(z-z_0)}{\pi w_0^2}\right)^2} \quad ...(8)$$

2.6 Longitudinal modes in fibres

Thus far only transverse modes have been discussed. We will now briefly look at some basic concepts concerning longitudinal or "axial" modes in a fibre cavity. The round-trip phase or frequency condition only allows for standing wave solutions within the fibre cavity. That is, the laser will only oscillate at axial mode frequencies separated by a discrete frequency given by,

$$v = \frac{c}{2nl} \quad ...(9)$$

where c is the speed of light, n is the refractive index of the fibre and l is the fibre length.

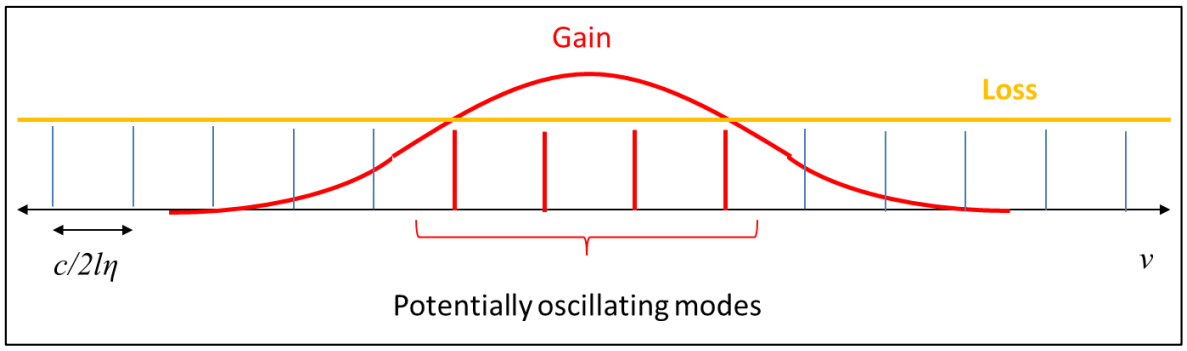

Figure 19: Potential longitudinal modes for an arbitrary fibre laser in the frequency domain.

Figure 19 demonstrates the favourable longitudinal modes within a laser cavity. The red trace in Figure 19 represents the gain curve and the yellow trace the loss. As discussed in section 1.3, laser action will only take place when the round trip laser gain exceeds the cavity losses, and since the gain for a specific gain material is wavelength dependent, only certain wavelengths where the gain to loss ratio exceeds unity will potentially oscillate within the cavity [49].

The fibre lasers developed in this dissertation have lengths in the order of metres. The frequency spacing v, which is indirectly proportional to the length of the gain material (Equation 9), is therefore approximately 2 orders of magnitude smaller in fibre lasers than in typical solid state lasers. Due to the small frequency spacing combined with broad spectral bandwidth (~1850-2100 nm) [51] and high round trip gains (20-30 dB) [46], it should be expected that the spectrally free running TDFLs developed in this dissertation will be highly multimodal (longitudinal modes).

The superposition of two or more longitudinal modes can form beat notes known as "mode beating". When many longitudinal modes with a fixed phase relationship are superimposed, a single pulse can be generated. This phenomenon is known as "mode locking". The resulting mode locked pulse will have a pulse length much shorter than the cavity round trip time and move through the cavity at the group velocity of the central mode. The pulse repetition rate of the mode locked pulse is v (Equation 9). Mode locking can be achieved actively [52], passively [53], and also as a consequence of the gain material and cavity configuration, known as self-mode-locking [54].

2.7 Q-switching

The Q in Q-switching refers to quality factor of an optical resonator given by,

$$Q = v_0 T_{rt} \frac{2\pi}{l} \quad ...(10)$$

where v_0 is the optical frequency, T_{rt} the round trip time of the cavity and l is the cavity loss. Equation 10 reveals that when l is high, Q is low, and referred to as a low-Q cavity. The opposite is true for a high-Q cavity. A Q-switch is essentially any loss mechanism that can be introduced into a laser cavity, either passively or actively, resulting in a low-Q cavity for some instance and high-Q cavity otherwise. Figure 20 illustrates a laser pulse being generated in a pulse pumped, Q-switched laser. The parameter $N(t)$ represents the population of the upper state laser level. N_i, N_f and N_{th} represent the initial, final and threshold upper state laser populations for the low-Q regime. Let's first consider the high-Q regime (Q-switch off). If the pump rate is high enough such that there is a population inversion, the small signal gain will exceed the cavity losses and laser action will take occur. For the low-Q regime (Q-switch on), significantly more gain and hence a much higher N_{th} needs to build up in the cavity before laser action can occur. Laser action is essentially "held off" with the Q-switch on and before the laser "breaks through", the Q-switch is switched off. Within 10's of nanoseconds (AOM) the cavity changes from a low to high-Q cavity resulting in the highly populated upper state laser level quickly depopulating by emitting a giant laser pulse.

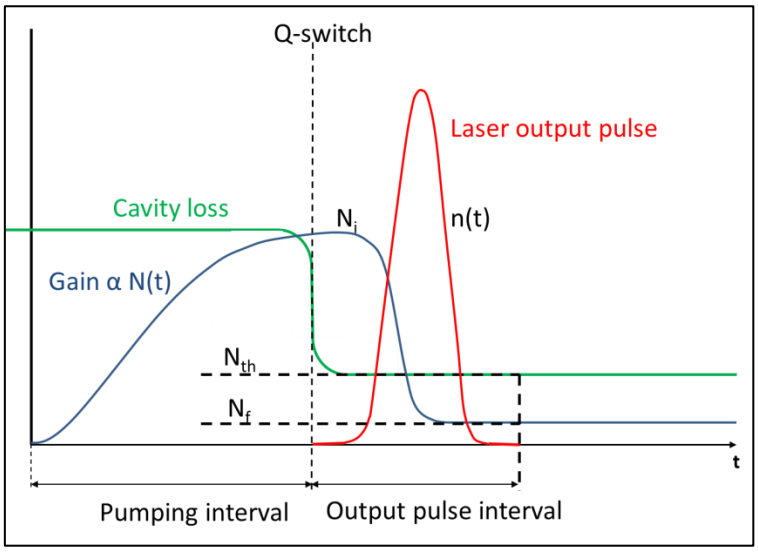

Figure 20: Simplified, schematic illustration of Q-switching population dynamics and laser signal pulse generation when pulse pumped.

Several Q-switching mechanisms exist such as rotating mirror, electro-optic, acousto-optic, saturable absorber, distributed Brillouin scattering, self Q-switching and thin-film absorber [49]. Acousto-optic and electro-optic are both active Q-switching methods. For high power pulse generation in TDFLs either can be used. Electro-optic modulators (EOM's) have several distinct advantages over AOM's,

namely, they have faster switching times (< 10 ns) and higher induced losses resulting in improved hold off [55]. Acousto-optic modulators (AOM's) on the other hand have relatively simple electronic circuitry, robust construction, reduced electromagnetic interference, and are generally less expensive. Also, when considering active Q-switching devices, switching time does not play a significant role in restricting pulse lengths but rather the fibre parameters. Pulse length is given by,

$$\tau_p = \left(\frac{r\eta(r)}{r-1-\ln r}\right)\left(\frac{2L}{cl}\right) \quad \ldots(11)$$

where, $\eta(r)$ is the energy extraction efficiency, l is the cavity loss for a single pass, r is the ratio of pump power to threshold power and L is the optical cavity length. Analysis of Equation 11 reveals that increasing r and decreasing L will decrease τ_p. In lieu of these facts, short TDFLs have been developed with laser output pulse lengths shorter than 50 ns [56]. The choice of fibre in these instances is usually a core pumped, single mode fibre similar to the SM fibres listed in Table 2. Since the fibres are core pumped, pump absorption is high which increases r and decreasing L. There are some drawbacks however. Core-pumping requires near single mode pump light and the laser output power of such short lasers is typically quite low. To overcome these limitations these lasers are typically pumped in-line with EDFL's and used as seed lasers for single or multiple stage amplification [57].

Gain switched TDFLs have also been shown to develop high peak powers (~100 kW) with pulse lengths in the order of picoseconds. Gain switching is typically achieved by modulating the pump diodes of a TDF seed laser for a single or multiple stage amplifier(s) [58].

The aim of the Q-switched TDFL developed in this dissertation was to develop high average power, short pulse length (~100 ns), 2 µm source. LMA thulium-doped fibre lasers, Q-switched with an AOM have been shown to offer high levels of extractable energy and pulse lengths shorter than 100 ns [12].

2.8 Literature review on continuous wave and pulsed TDFLs

2.8.1 High power cw TDFLs

In this literature review the author analysed some notable TDFLs that have been developed over the years. The various fibre laser architectures will also be analysed with special emphasis placed on design simplicity, pulsed or cw output characteristics, high output power and laser efficiency. The pulsed lasers analysed were all designed for pumping OPO crystals and therefore all have pulse lengths in the tens of nanoseconds range (Table 3).

A short list of commercially available, high power cw and pulsed TDFLs available in the market place has been included (table ref). The pulsed lasers in table have pulse lengths in the tens of nanosecond range.

The first reported TDFL was a free space coupled laser with cw output. It was developed in 1988 by Hanna [19]. This early TDFL was made up of a 27 cm long, single mode, 0.15 NA fibre with a core diameter of 9 µm. The fibre was pumped by a 797 nm dye laser and dichroic mirrors were used as input and output couplers. The TDFL developed by Hanna was at the time the longest wavelength ever reported in a silica fibre. The paper also highlighted several important outcomes;

- Due to the broad fluorescence spectrum at 2000 nm, a wide tuneable range could be available.
- A reduction in fibre cooling resulted in a wavelength shift towards longer wavelengths due to self-absorption in the fibre.
- Pumping with ~800 nm AlGaAs laser diodes should be possible.
- Increasing the doping concentration could reduce the long wavelength limit within the silica host.

The predicted outcomes listed above were all correct. A TDFL has been tuned with a volume Bragg grating (VBG) from 1947 nm to 2052 nm [59] and heat effects do reduce laser performance, as experiments show in chapter 3. TDFLs are now often pumped with readily available AlGaAs laser diodes (Table 3). Highly doped TDF's are also readily used. The high doping concentration does indeed reduce fibre length required and therefore absorption by the host as well as promote cross-relaxation processes.

To date the highest reported output power for a cw TDFLs is 1000 W (laser 2 in Table 3) [8]. The laser system was an all fibre, master oscillator power amplifier (MOPA). The master oscillator (seed laser) was a 50 W single mode laser with an output wavelength of 2045 nm. The two stage amplifier was pumped with six laser diodes per amplifier stage and coupled to each of the 8 m, low doping concentration TDF's with (6+1)x1 pump-coupling optics. The doped fibres had core and cladding diameters of 20 and 400 µm's respectively. The resulting slope efficiency of the MOPA was 53 %.

To date, the next most powerful cw, TDFL developed, was a bidirectionally pumped free space coupled laser with a maximum power output of 885 W [7]. Each pump was capable of delivering 1 kW of ~790 nm laser output. The TDF used in the experiment had a doping concentration of approximately 4 wt. % and core and cladding diameters of 40 and 635 µm respectively. The V parameter for this fibre was 12.3 and as a result, the measured M^2 values were poor, ranging between 6 and 10.

Free space coupled MOPA's with high output powers and near diffraction limited beam quality has been developed. One such a laser was developed by Goodno which had an output power exceeding 600 W and a measured M^2 of 1.05 [60]. The TDF used for the amplifier stage was 3.1 m in length and had core and cladding diameters of 25 and 400 µm respectively.

Table 3: cw and pulsed TDFLs.

#	TDFL description	Pump description	Output laser wavelength [nm]	Average output power [W]	Peak pulse power [kW]	Pulse energy [uJ]	PRF [kHz]	Pulse length [ns]	Slope efficiency [%]	Main Author (Year)
1	Free space coupled, CW output, Fabrey Perot cavity	2 x 1 000W , 793 nm laser diodes	2040	885	-	-	-	-	49.2	Moulton [7] (2009)
2	All fibre, CW, MOPA	2 x (6 x 150 W), 793 nm laser diodes	2045	~1000	-	-	-	-	53.2	Ehrenreich [8] (2010)
3	Free space coupled, MOPA	2 x 793 nm laser diodes and 16 W, 2040 nm 3 stage pre-amplifier seed laser	2040	608	-	-	-	-	54	Goodno [59] (2009)
4	Free space coupled, CW output, Fabrey Perot cavity	70 mW, 797 nm dye laser	1880-1960	0.0027	-	-	-	-	~13	Hanna [19] (1988)
5	All fibre, gain switched	2 stage EDF amplifier with 1550 nm seed pulse from laser diode	2000	21.1	7.03	211	40	40	43	Creeden [60] (2008)
6	All fibre, gain switched	2 stage EYDF amplifier seeded by 1550 nm seed diode	2044	8	1.00	35	300	25	~55	Simakov [62] (2012)
7	Free space, gain switched	4W 1919 nm Tm:YLF seed pulse, 2 x 230 W 793 nm laser diode pumped amplifier	2020	100 (@max)	138 (@max)	>10000 (@max)	0.5-500	>75	52	Tang [62] (2010)
8	AOM Q-switched, Free space coupled, Fabrey Perot cavity	Bidirectional pumped with 2 x 793 nm laser diodes	1983	30	*6.9	270	100	41	37	Eichhorn [63] (2007)
9	EOM Q-switched, free space coupled, Fabry Perot cavity	3.5 W, 1.319 nm, Nd:YAG laser	~2000	-	3.3	2300	0.07	320	30	El-Sherif [55] (2003)
10	AOM Q-switched, free space coupled, Fabry Perot cavity	1 X 793 nm 300 W laser diode	1992	28	*2.28	360	100	115	40	Willis [65] (2010)
11	AOM Q-switched, free space coupled, Fabry Perot cavity	Bidirectionally pumped with 2 X 793 nm, 100 W laser diodes	2024	23	*8.31	*575	40	65	32.5	Kieleck [12] (2015)
12	AOM Q-switched, free space coupled, Fabry Perot cavity, photonic crystal fibre	100 W, 793 nm laser diode	~2000	-	8.9	435	10	49	26	Kadwani [65] (2012)

*Calculated

Table 4: List of commercially available TDFLs in the marketplace

Manufacturer Model#	TDFL description	Average output power [W]	Pulse energy [uJ]	PRF [kHz]	Pulse length [ns]	Selectable Wavelength range [nm]
IPG TLR-200,	cw, single transverse mode output	200	-	-	-	1800-2100
IPG TLR-500	cw, multi transverse mode output	500	-	-	-	1900
NP Photonics 2 micron high power fibre laser source	cw, < 0.1 nm spectral bandwidth, single transverse mode output	25	-	-	-	1900-2000
IPG TLPN-1-1-20-M	Nanosecond pulsed, single transverse mode output	20	1000	20-50	1-100	1900-2050
Advalue Photonics AP-QS1-MOD	Q-switched TDFL (assumed), single transverse mode output	10	500	10-30	20-200	1920-2000

2.8.2 Discussion on high power CW TDFLs

At high lasing powers, nonlinear scattering effects such as Stimulated Raman Scattering (SRS) and Stimulated Brillouin Scattering (SBS) can set in. The maximum powers before the onset of these nonlinearities can be approximated by,

$$P_{\max}^{SRS} \approx \frac{16A_{eff}}{g_R L}\ln(G) \quad \text{...(12)} \qquad \text{and} \qquad P_{\max}^{SBS} \approx \frac{17A_{eff}}{g_B L}\ln(G) \quad \text{...(13)}$$

where A_{eff} is the mode field area, g_R and g_B are the Raman and Brillouin gain coefficients, L is the fibre length and G is the fibre gain [46]. Advantages of TDFLs when considering SBS and SRS thresholds include their reduced fibre lengths (L) owing to their high doping concentrations and increased mode field areas (A_{eff}) with no compromise to the beam quality. The increased mode field area is a result of the longer operating wavelengths of TDFLs (Equation 4). In the paper by Goodno *et al*.[60], the calculated SBS limited maximum obtainable output power was calculated to be ~275 W. The laser produced in excess of 600 W of output laser power indicating that SBS is suppressed in TDFLs. The likely mechanism for the SBS suppression was shown to be pump-induced thermal gradients in the active fibre [67]. It was therefore suggested that for scaling to even higher powers the pump absorption coefficient should be decreased by reducing the core to cladding ratio, thus reducing pump absorption. The reduction in pump absorption could then be offset by using longer lengths of active fibre. An added benefit to this suggestion was an increased cladding area for coupling pump light. Comparison between the fibre parameters of laser 2 and laser 3 (Table 3) suggests that these where valid recommendations. Another solution to reducing nonlinear scattering would be to increase A_{eff} , as with laser 1. This approach however reduces beam quality.

From a design perspective, the free space coupled lasers (lasers 1 and 4 in Table 3) are the simplest. They rely on Amplified Spontaneous Emission (ASE) to initiate laser action and the free space configuration is relatively simple to set up. Scaling to high powers in excess of 200 W with a narrow output spectrum (< 1.5 nm) has been demonstrated [51]. The major advantage of all fibre systems is they are more robust, that is, they cannot be misaligned or be perturbed by atmospheric

interference. Pumping with multiple diode lasers also allows for continued operation if a diode fails which advantageous for turnkey systems where reliability is important.

2.8.3 Pulsed nanosecond TDFLs

The first fibre-pumped optical parametric oscillator (OPO) was developed by Creeden *et al.* (laser 5 in Table 3)[61]. The laser was a resonantly pumped, gain switched TDF. The seed pulse for the TDF was rather elaborate. It was made up of another gain switched TDF, seed pulsed by a 1550 nm laser diode. The seed pulse was amplified by a two stage erbium-doped amplifier pumped by 790 nm laser diodes. The end result was 211 µJ pulses with 40 ns pulse lengths. The beam quality was measured to have a M^2 value of 1.08. A Zinc Germanium Phosphide (ZGP) (OPO) crystal was pumped with the laser and 2 W of mid-IR radiation with a conversion efficiency of 20 % was produced. Since the OPO pump source was unpolarised, only 60 % of the beam contributed to mid-IR conversion resulting in the poor conversion efficiency.

A polarised, pulsed source was later developed by Simakov *et al*. [62]. The laser design was similar to that of Creeden's. The two stage amplifier was made up Erbium-Ytterbium Doped Fibres (EYDF's). The gain switched TDFL consisted of a 20 cm TDF with a high reflecting input coupler and 5 % reflectivity output coupler. The gain fibre and FBGs were all panda type polarisation maintaining (PM) fibres Single linear polarisation output was enforced by splicing the output coupler FBG at ninety degrees to the TDF. This laser was later amplified to pump a ZGP OPO. The resulting conversion efficiency was 25 % [61].

A pulsed 2020 nm source was developed by Tang *et al*. [63] which when tuned, produced maximum peak powers of 138 kW and 10 mJ of energy at a minimum pulse length of 75 ns. The laser was made up of a two stage gain switched TDF amplifier. The pulse source was an AOM Q-switched Tm:YLF slab laser. The entire laser was made up of free space-coupled elements. 1 mm Silica endcaps were fusion spliced to 0.4 mm fibre tips to avoid optically-induced catastrophic damage to the fibre tips.

The lasers discussed thus far are relatively complex. Simpler designs consisting of a Q-switched, Fabry-Perot cavity have also been developed (lasers 8-12 in Table 3). A non-polarised source was developed by Eichhorn *et al.*[64] using a LMA TDF with a 20 µm core and 300 µm diameter. Power scaling was limited to ASE build-up in the laser despite 8 % angle cleaves and the < 80 % deflection efficiency of the AOM. The laser produced 240 µJ, 41 ns pulses. A polarised, single frequency source incorporating a 20/300 µm TDF was developed by Kieleck *et al.* [12]. Although this laser was similar the one developed by Eichhorn et al. it operated at a lower PRF's. The lower PRF translates to higher peak pulses and energies despite the lower average power.

An EOM Q-switched TDFL was developed by El-Sherif and King (laser 9 in Table 3). For this experiment a 2 m, 17/125 TDFL was used. The laser was pumped with a 1319 nm Nd:YAG laser with a maximum available power of 3.5 W. The EOM restricted the switching time to < 100 Hz. At 70 Hz operation the 320 nm pulses had peak powers of 3.3 kW corresponding to 3.2 mJ of energy. The stable, low frequency operation of the Q-switched TDFL is a testament to the EOM's superior hold off limit. Pulse length reduction has been shown to decrease with increased pump power and given the low pump power available for this experiment, it is unclear how well this laser performed.

An AOM Q-switched TDFL was developed by Willis *et al.* [65]. A 25/400 polarised TDF was used for the experiment. At 100 kHz pulse repetition rate the laser produced 360 µJ pulses with pulse lengths of 115 ns. The optical feedback element for this source was a 2 µm high reflection mirror.

The last nanosecond pulse TDFL to be discussed in this dissertation is an AOM Q-switched photonic crystal fibre (PCF). The PCF had a 0.04 NA, 50 µm radius core. The pump source was a 793 nm diode laser. The low NA allowed for near single mode behaviour (M^2 <1.15) despite the large mode field area. The large core to cladding ratio of the PCF offers high gain in relatively short lengths of fibre. This PCF TDFL produced output pulses with peak powers of 8.9 kW and pulse lengths of 49 ns, making it to date, the most powerful Q-switched TDFL ever developed. The pump absorption for the PCF was ~ 5.8 dB/m and the thulium doping concentration was a relatively low 2.5 wt. % indicating that The PCF could produce higher powers and shorter pulse lenghts.

2.8.4 Discussion on pulsed nanosecond TDFLs

Table 5 lists in order of length some fibre parameters for the Fabry Perot AOM Q-switched TDFLs discussed in this literature review.

Table 5: Correlation between cladding radius and pulse length for three AOM, Q-switched TDFLs.

Laser	Core radius [µm]	Cladding radius [µm]	Fibre length [m]	Minimum pulse with [ns]
Eichhorn [64]	20	300	2.3	41
Kieleck [12]	20	300	3.1	65
Willis [65]	25	400	4	115
Kadwani [66]	50	250	2.7	49

Comparison of fibre length with output pulse length indicates very clearly that decreased cavity length results in shorter pulse lengths (Equation 11). It should also be noted that for the shorter fibres the core to cladding ratios are higher. Increasing the core to cladding ratio increases pump light absorption per unit length thus compensating for the shorter TDF geometry.

Chapter 3: Design, cavity and temperature considerations for TDFLs

3.1 Introduction

In order to develop a high power, (> 50 W) TDFL which is efficient, has good spectral, spatial and temporal stability (cw output), and a near diffraction limited beam divergence, some level of technical expertise and fundamental understanding of TDFL behaviour is required. The experiments in this chapter were aimed at addressing these requirements. The technical aspects such as fibre preparation and laser design are covered in section 3.2 wherein a basic TDFL is developed using a short "test" TDF. Fundamental understanding of TDFLs is addressed in the experiments that follow, namely, the "optimisation of the TDFL cavity" (section 3.3.3) and "effect of air cooling on power, temporal stability and spectral output" (section 3.3.1). In the first experiment, the effect of changing the output coupler mirror reflectance on spectral stability, and output power is analysed. This experiment along with the discussions was included to gain understanding into power scaling limitations with respect to the choice of fibre length, pump absorption, and cavity configuration. In the second experiment, temporal stability, spectral stability, and laser efficiency is analysed with and without a simple air cooling scheme. The discussion based on this experiment aims to expand on current knowledge regarding the relationship between reabsorption, temperature, and self-pulsing in TDFLs with the aim of assessing various factors that contribute to temporal instability in TDFLs.

Conclusions based on the findings and recommendations found in this chapter were implemented further, and will be discussed in chapter 4 to develop the high power cw TDFL.

3.2 Experimental design and setup

This section will introduce the relevant components, fibre preparation techniques and design considerations involved in the development of a simple TDFL. Stripping, cleaving and cleaving techniques are discussed as well as the pump design and performance. TDFL design considerations and, laser development techniques relevant to this dissertation are also discussed.

3.2.1 Fibre parameters and preparation techniques

A 0.9 m long 25/400, LMA, Tm-doped double clad fibre was used for this experiment. The fibre parameters are listed in Table 2 (Chapter 2) and the cross sectional profile of the fibre is shown in Figure 17 (Chapter 2).

Fibre preparation is an essential first step when building a fibre laser. For the efficient launching of pump light into the fibre, the facets at the fibre tips must have a mirror-like finish and be free of any dirt or grit. Contaminants on the fibre facet impedes light transmission and if exposed to high intensity laser or pump light, cause permanent burns on the surface reducing laser performance.

Several fibre preparation techniques are required namely stripping, cleaving and cleaning of the fibre tip.

Stripping the fibre of its low index polymer coating is the first step in the preparation process and is done for several reasons. If not removed, the high intensity pump beam will burn the coating resulting in a dark residue on the fibre surface. This dark residue can in turn decouple and absorb incident pump light, decreasing laser efficiency.

Several techniques for stripping the protective coatings of optical fibres are available such as, hand held mechanical fibre strippers, auto-strippers, and blades to name a few. For this dissertation, fibre was stripped by first soaking the coated fibre tip in acetone for ~10 minutes after which the softened polymer coating was easily removed with a plastic tweezers. This method was decided on since there is only slight mechanical stress and scraping of the fibres outer cladding surface. Another benefit of this method is that it reduces the chances of accidentally breaking the fibre tip, reducing waste. Figure 21 illustrates the modified dropper bottle used for soaking the fibre tips in acetone.



Figure 21: Fibre tip soaking in acetone.

After the removal of the protective coating, the tip was cleaned several times with lint free tissues soaked in isopropanol to remove any remaining coating on the silica surface.

The next step in the fibre preparation process is to prepare the fibre tip facets. It is essential that the tip facets have a clean, mirror-like finish to ensure efficient coupling of light in and out of the fibre. The tip faces can either be mechanically polished or, as was the case for this dissertation, cleaved. The basic process of cleaving is to place a tension along the optical axis of the fibre and then scribe the surface, (perpendicular to the optical axis) with a diamond tipped scribe or blade. The induced “scratch” then breaks the surface tension of the fibre and a crack propagates to the opposite end of the fibre resulting in a perpendicularly cleaved fibre facet. For smooth glass-like cleaves, the cleaver must be optimised for different fibre types. For instance, if the tension applied on the fibre is too

high, a shock wave will propagate through the fibre resulting in “mist”, and in severe cases “hackle” [68]. Also if the tension is too low, the blade can chip the fibre. Figure 22 illustrates the formation of mist and hackle as tension is increased in 25/400 LMA passive fibre (Table 2).

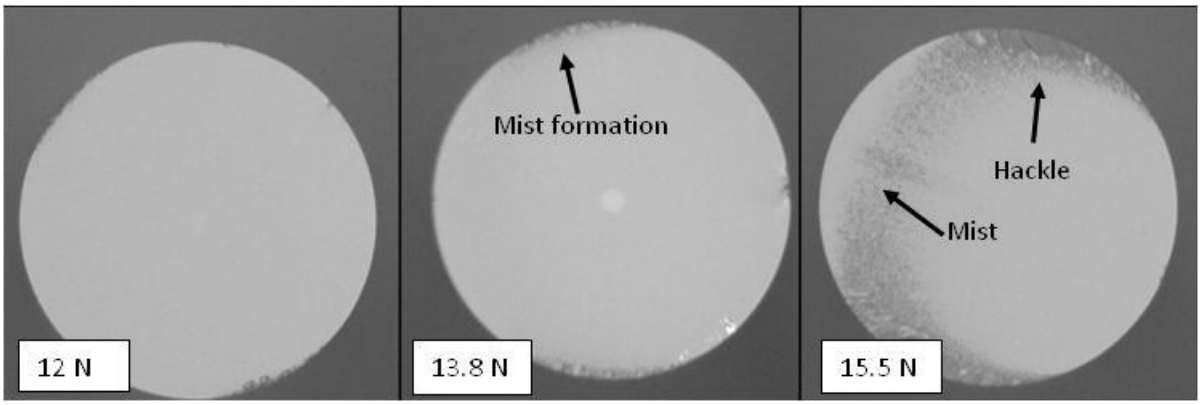

Figure 22: Optical microscope images of the fibre facets at various tension settings performed on a Nufern, LMA 25/400 passive fibre (Table 2).

All cleaving in this dissertation, including those illustrated in Figure 22, was performed with a 3SAE LCC2-A cleaver. The basic operation of the cleaver is as follows. An internal heating element melts the ingot into which the fibre tip is placed. The ingot then solidifies and clamps the fibre tip in place. A second clamp then closes onto the fibre about 15 cm above the ingot and applies an adjustable tension to the fibre. Figure 23 (right) shows a fibre under tension clamped between the ingot and the mechanical clamp (above the ingot). Once the tension reaches its set point, a diamond tipped blade moves into position to scribe the fibre surface. The scribing action is enhanced by the vibrating action of an internal piezo electric crystal [69]. Figure 23 (left) shows a fibre under tension with the blade and backstop in the cleaving position. The backstop prevents the fibre from flexing

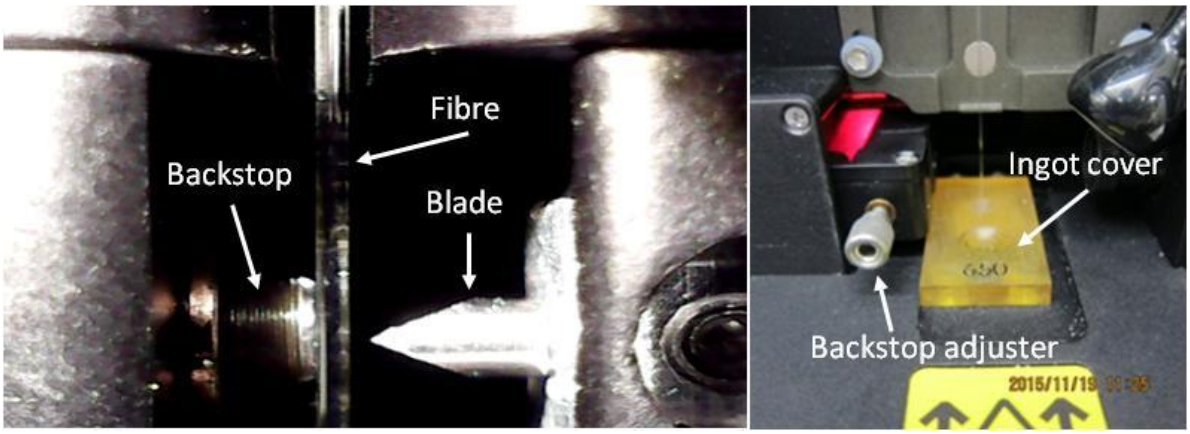

Figure 23: (left) Blade in position to cleave a fibre and (right), the blade / backstop assembly with ingot cover / fibre guide.

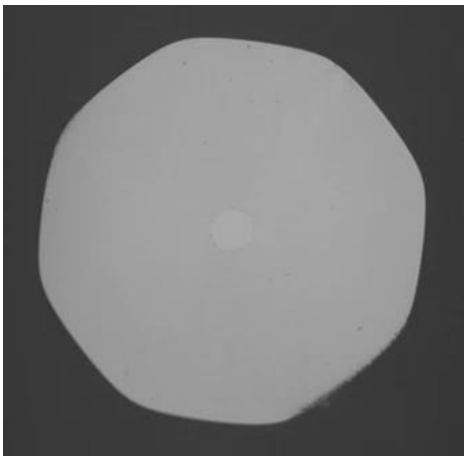

Figure 24: A clean mirror-like cleave of a LMA 25/400 thulium-doped fibre as used in this dissertation.

Cleave optimisation was performed by varying the tension applied to the fibre. The remaining settings were left at the factory default settings for cleaving LMA, 400 µm diameter fibres. The settings are listed in Appendix B. After cleaving, the facets were inspected under a microscope. The result was clean mirror-like facets as in Figure 24.

Flat cleaves are readily used as output couplers for fibre lasers. This is due to the ≈ 4 % Fresnel reflection at the glass to air interface. For some fibre designs, the 4 % feedback of the flat cleave is not desired. In these cases the fibre tip is instead angle cleaved to ~8° to reduce Fresnel reflection at the fibre facet [70]. If the fibre tip is not angle cleaved the laser will consist of two cavities, one provided by the optical feedback element and another from weakly reflecting flat cleave. This weak reflection causes parasitic lasing modes, that is, lasing modes with different properties, such as polarisation and wavelength, to the laser modes within the cavity enforced by optical feedback elements. Angle cleaving can be achieved, as is the case with the 3SAE LCC2-A cleaver, by twisting the fibre about its optical axis during the cleaving process. The resulting cleave angle was measured with a Zeiss, Axiocam fitted microscope as in Figure 25.

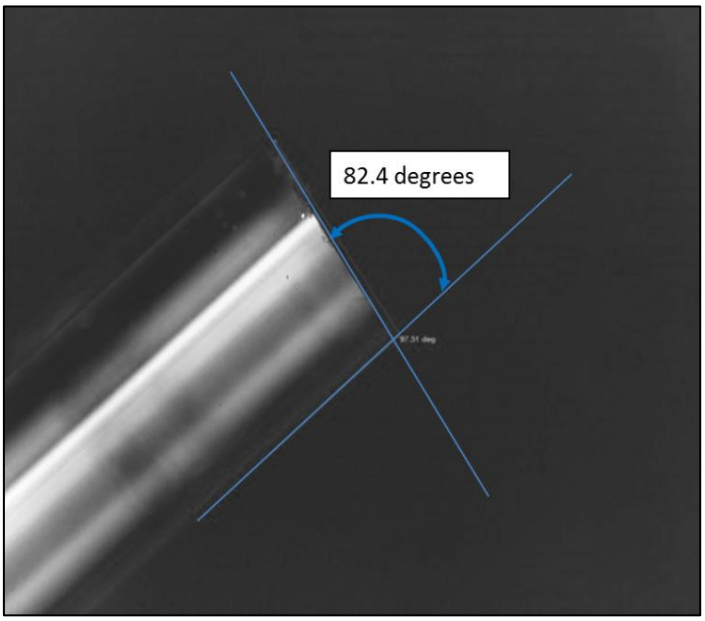

Figure 25: Microscope image of a 7.8^{o} (90°-82.4^{o}) angle cleaved Nufern 25/400 passive fibre.

3.2.2 Pump design and coupling efficiency

Coupling efficiency, in the context of this dissertation, refers to the efficiency with which light from a pump source is guided through free space into an optical fibre. In this and the following experiments, the coupling efficiency was measured by launching pump light into a passive fibre and comparing the transmitted (light exiting fibre) to the incident (light entering fibre) pump power. It is assumed that pump attenuation due to the silica fibre was negligible [43]. Also, the amorphous silica host was assumed to be polarisation independent and multimodal. Average transmitted power was measured on a power meter.

In order to maximise the coupling efficiency, suitable optics are important. The optics were chosen according to focal length, surface coatings, lens diameter and whether or not the lenses are corrected for spherical or chromatic aberrations. However, before such a choice can be made, the pump source, and the fibre being coupled into (target fibre), need to be considered.

The pump source was a DILAS, 150 W (limited to 130 W), cw, fibre-coupled multi-bar laser module, emitting at a central wavelength of ~790 nm (Figure 26). The wavelength of the pump source is shown to drift towards longer wavelengths with increasing pump power. Highly efficient TDFLs pumped at 790 and 800 nm have been demonstrated [71,72] in this range. The peak value in this absorption band is 790 nm [73].

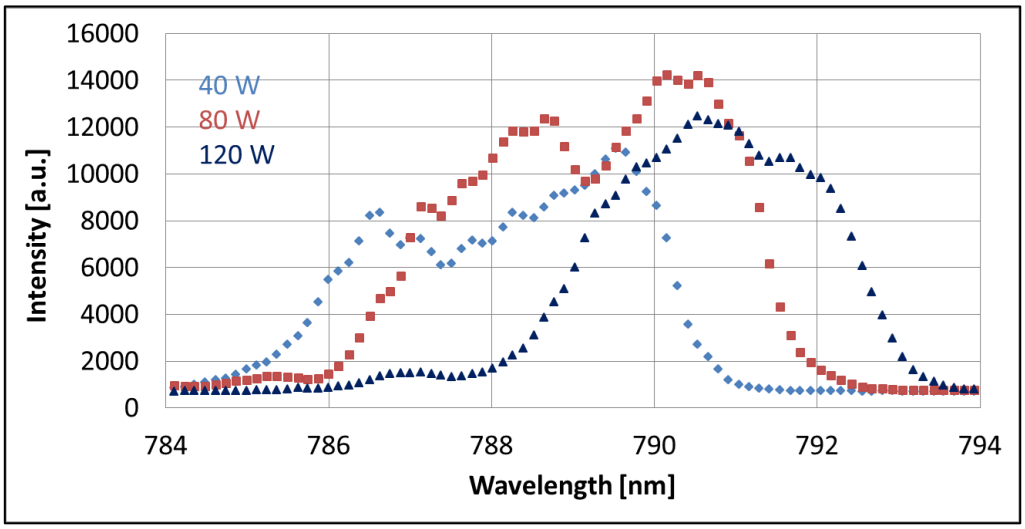

Figure 26: Output wavelengths for the FCLD at various pump powers.

The fibre-coupled laser diodes (FCLD's) delivery fibre had a diameter of 200 µm and a 0.22 NA. The fibre being coupled into was a Nufern LMA 25/400 passive fibre, specifically mode matched for the doped fibre specified in (Table 2).

To simplify the choice of optics a simple rule was followed, that is, the NA of the final pump optics lens must be less than or equal to the NA of the fibre being coupled into. If the NA of the lens is greater than the NA of fibre, any light travelling on a path with an NA greater than the fibre will simply decouple. Also, the focal length of the pump optic must be short enough such that the diameter of the diverging FCLD's pump beam is well within the lens diameter.

With this in mind, a two lens system was decided upon. The two lenses were both aspherically corrected 50 mm focal length lenses with lens diameters of 25.4 mm. The first lens would collimate light exiting the FCLD onto the second lens, which would focus the pump light into the target fibre. A quick approximation (beam diameter = 2 x focal length x NA) indicated that the beam diameter onto the pump optics would be 22 mm (< 25.4 mm), also the 1:1 magnification would result in a ~200 µm beam diameter being coupled into the ~400 µm diameter fibre. The lens substrate was BK7 optical glass coated for maximum transmittance in the ~793 nm wavelength range. The lenses were cage mounted and attached to a XYZ translation stage for ease of alignment with the fibre tip. Figure 27 shows the complete pump assembly which was used for this dissertation. The diagram illustrates the path of the pump light which is first collimated and then focused into the target fibre.

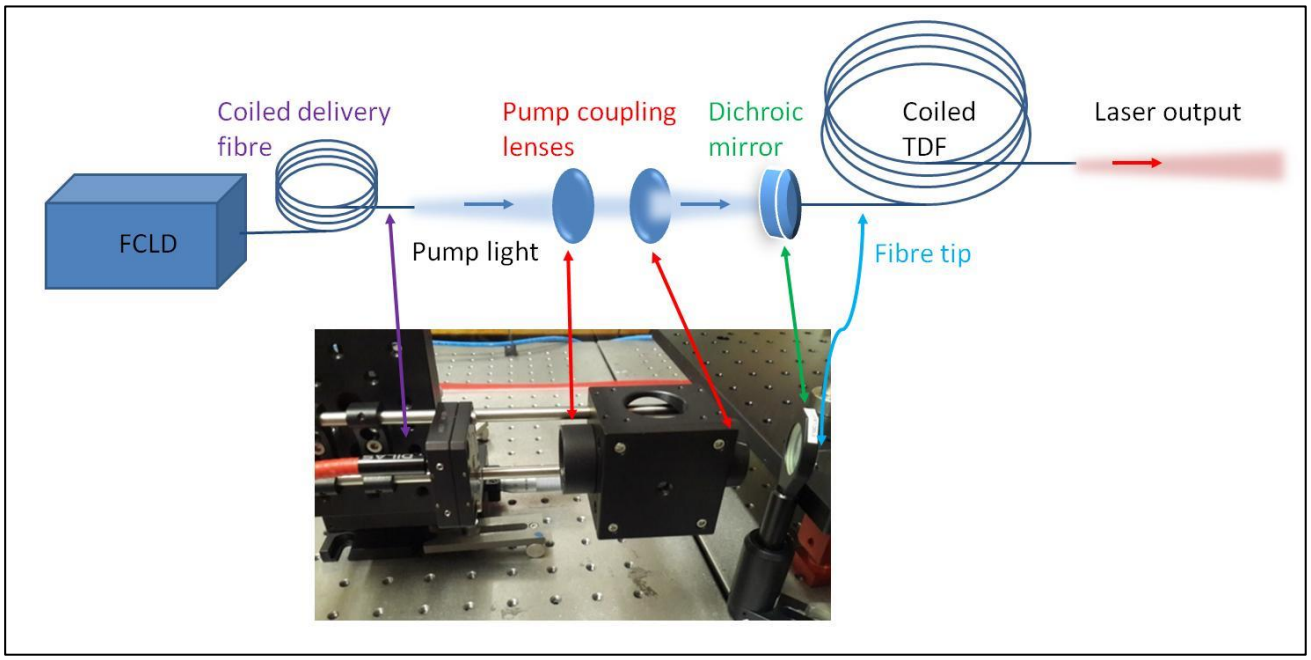

Figure 27: The complete pump assembly with a simple diagram illustrating the coupling of pump light into a target fibre through a dichroic mirror (input coupler).

The pump scheme performed sufficiently well. Losses due the optics were less than 4 % and the coupling efficiency was measured to be 93 % (Figure 28), of which at least 4 % loss can be attributed to Fresnel reflection at the fibre tip facets.

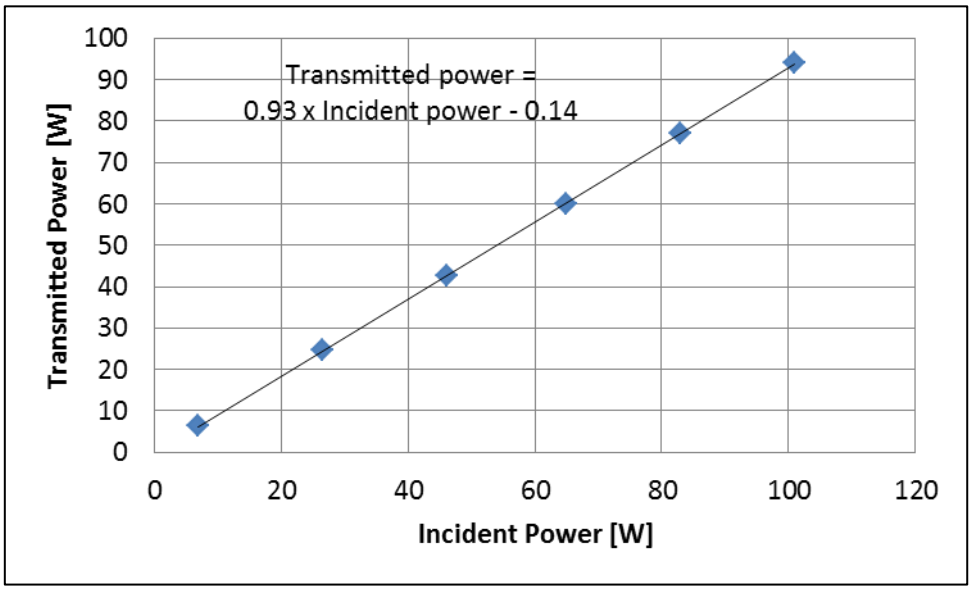

Figure 28: Graph of the measured coupling efficiency.

3.2.3 Laser design and setup

For this experiment, two basic fibre laser configurations were considered, namely configuration 1 and configuration 2 (Figure 29(i-ii)). The two designs differ in that for configuration 1, the laser output (thin red lines) and the pump input (blue lines) are in juxtaposition, whereas for configuration 2 they are on opposite ends of the thulium-doped fibre. For both configurations the TDF was flat cleaved at both ends and, DM1 and DM2 are both dichroic mirrors which are highly transparent for the 793 nm pump light but highly reflective for the 2 µm laser wavelength at zero degree incidence. Laser operation for configuration 1 worked as follows: Lenses L1 and L2 coupled FCLD pump light through the slightly offset (< 7°) dichroic mirror (DM1) into the thulium-doped fibre. Optical feedback of the laser signal was provided by DM2 (R ≈ 100 % @ ~2000 nm) which was butted (pressed against) against the fibre tip and the flat cleave (R ≈ 4 %) at the pump input fibre end. Similarly, for configuration 2, optical feedback was provided by DM1 and a flat cleave at opposite ends to that of configuration 1.

One benefit of using configuration 1 as opposed to configuration 2, is that the laser output and residual pump light (RPL) are completely separated. However, due to the confined space between the pump input end of the fibre tip and the lens L3 (f = 25.4 mm), configuration 2 was chosen for the cavity optimisation for ease of introducing the various reflectivity dichroic mirrors (output couplers) at the laser output end of the fibre.

Configuration 3 (Figure 29(iii)) is a modification of Configuration 2 and was used in the second experiment. Configuration 3 allowed the introduction of a volume Bragg grating (VBG) into the cavity, free of RPL, for wavelength selection. The VBG was introduced into the cavity by replacing the HR mirror with a VBG. DM1 in configuration 3 was a dichroic mirror highly transmittive for the pump light and highly reflective for ~2 µm wavelength laser light at 45° of incidence. The fibre tip labelled AC in Figure 29(iii) was angle cleaved to reduce parasitic laser action. The fibre was wrapped around a 13 cm diameter square grooved aluminium mandrel (details of the mandrel are covered in section of chapter 4.2.1). The fibre tip was then lightly fastened to an aluminium holder with approximately 1 cm of stripped fibre protruding over the holder's edge. The aluminium holder was then mounted onto a XYZ-translation stage. The TDFL set up in configuration 3 with an intracavity VBG is illustrated in Figure 30.

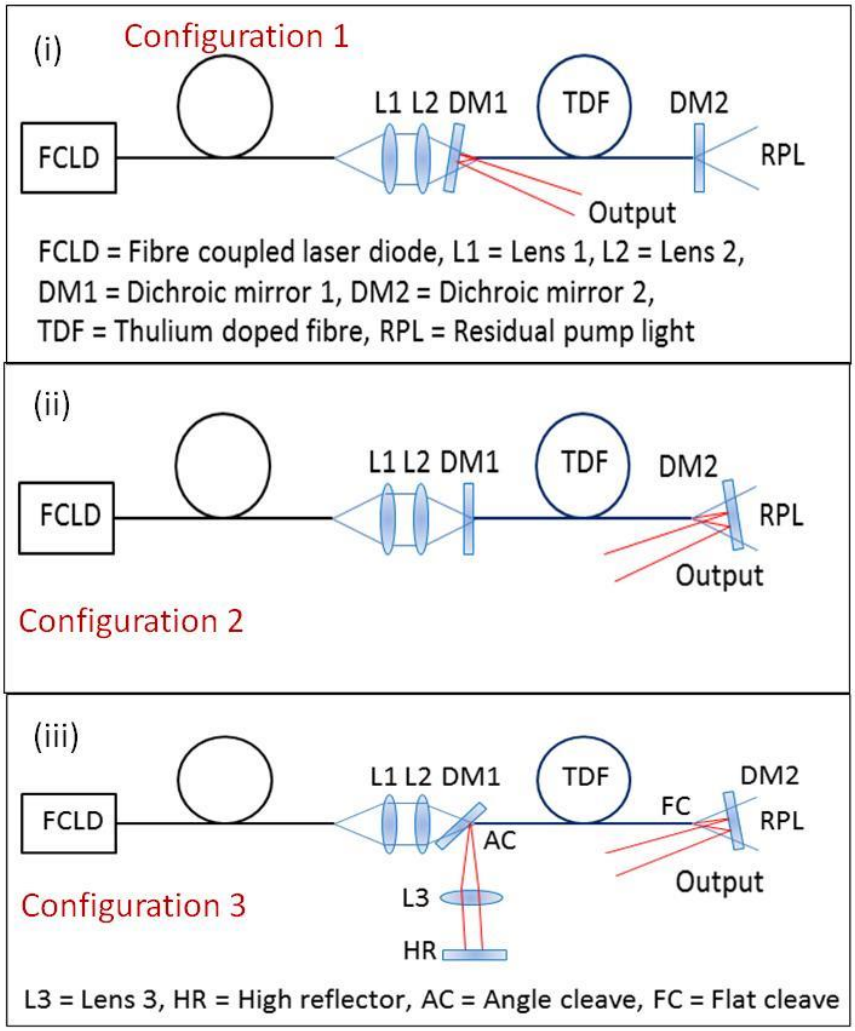

Figure 29: Various laser design configurations for the cw TDFLs developed in this dissertation.

VBGs are tip and tilt sensitive, so light falling onto the VBG must first be collimated. Collimation was achieved by adjusting the position and orientation of the lens L3 which was a 2 µm wavelength transmissive, 25.4 mm focal length, 12.7 mm diameter lens. A rough collimation was first performed visually with a pump light viewer. This was achieved by first coupling the pump light into the output end of the fibre (right side of the fibre in Figure 29(iii)). The residual pump light reflecting off DM1 was bright enough to be clearly observed with the viewer. L3 was then placed in the path of the reflected pump beam at approximately 25 mm from the fibre tip. The fibre tip to lens distance was adjusted with the XYZ-translation stage. Pump light passing through the lens was projected onto a white wall 1.5 m away. The fibre tip to lens distance was adjusted until the light converged to the smallest possible spot on the wall which was an image of the fibre tip approximately 2.5 cm in diameter. The lens orientation was adjusted until the image was symmetric and sharp. With the lens roughly in the correct position, the pump was returned to its original position and recoupled into the TDF. The pump power was then adjusted until amplified spontaneous emission (ASE) being reflected off DM1 could be observed on thermal paper. An HR mirror (HR in Figure 29(iii)), optimised for high

reflection in the 2 µm wavelength region was mounted on a tip and tilt stage and positioned in the path of the ASE signal. A power meter was positioned at laser output end of the fibre to monitor power. The tip and tilt of the HR mirror was then adjusted in a raster-like fashion (aided by a LED back reflecting off the HR onto a white page) until a surge in the output power was observed indicating laser action. By simultaneously adjusting the fibre to lens distance whilst ensuring that pump to fibre coupling was optimal, the TDFL could be optimised for maximum laser output power. After the TDFL was optimised for maximum output power, it was assumed that the lens L3 was correctly collimated and therefore suitable for VBG placement.

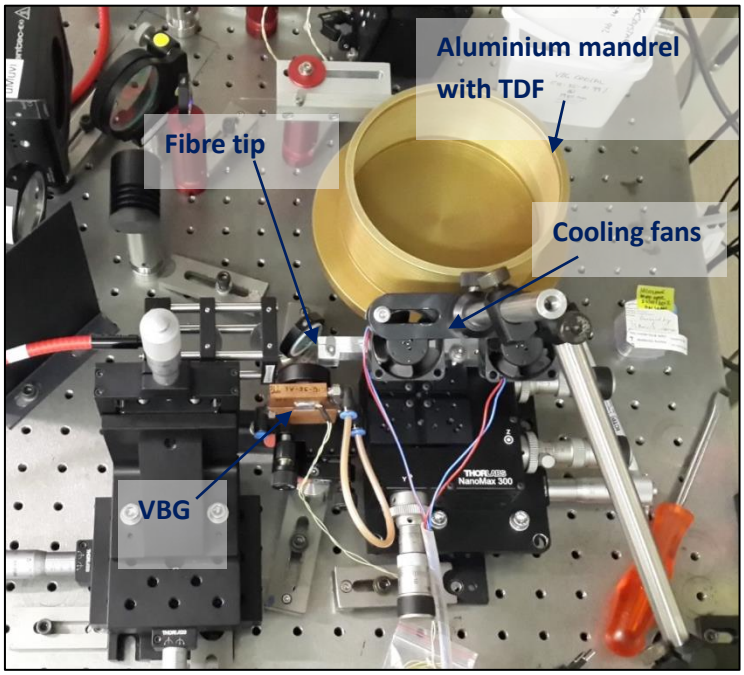

Figure 30: The TDFL set up in configuration 3 with the cooling fans and intracavity VBG in place.

3.3 Experimental results and discussions

3.3.1 Optimisation of the TDFL cavity

A fibre laser cavity consists of a high reflector mirror or FBG at one end (input coupler), and a partially reflective output coupler or FBG at the other (output coupler). Both the input and output couplers are wavelength specific in accordance with the specific gain material and usually both elements are highly transmissive to the pump light wavelength.

In this experiment the laser was setup in configuration 2. The fibre was not cooled or wrapped around the aluminium mandrel, but instead cooled by the ambient environment (25 ^{o}C). A dichroic mirror (DM1 in Figure 29(ii)) was used as the high reflector input coupling mirror, and mirrors with varying 2 µm wavelength reflectivities were used as output couplers. The aim of the optimisation

was to determine which choice of output coupler resulted in the best overall laser performance for the free running, ambient cooled (25 °C) TDFL. Laser performance was assessed according output power and spectral stability.

Similar experiments have been performed in literature where slope efficiencies of TDFLs were compared for varying reflectivity (laser wavelength) output couplers [73,74]. However, the author found no reports of spectroscopic measurements performed for various cavity configurations in literature. Also, although not much variance was expected, there were no reports for this experiment using this particular fibre. It was therefore decided to conduct the experiment to more fully characterise the fibre at hand and gain additional insight into the spectral behaviour of TDFLs with various cavity configurations.

Output power measurements were performed as a function of incident pump power. The output slope efficiency measurements for the respective output couplers can be seen in Figure 31.

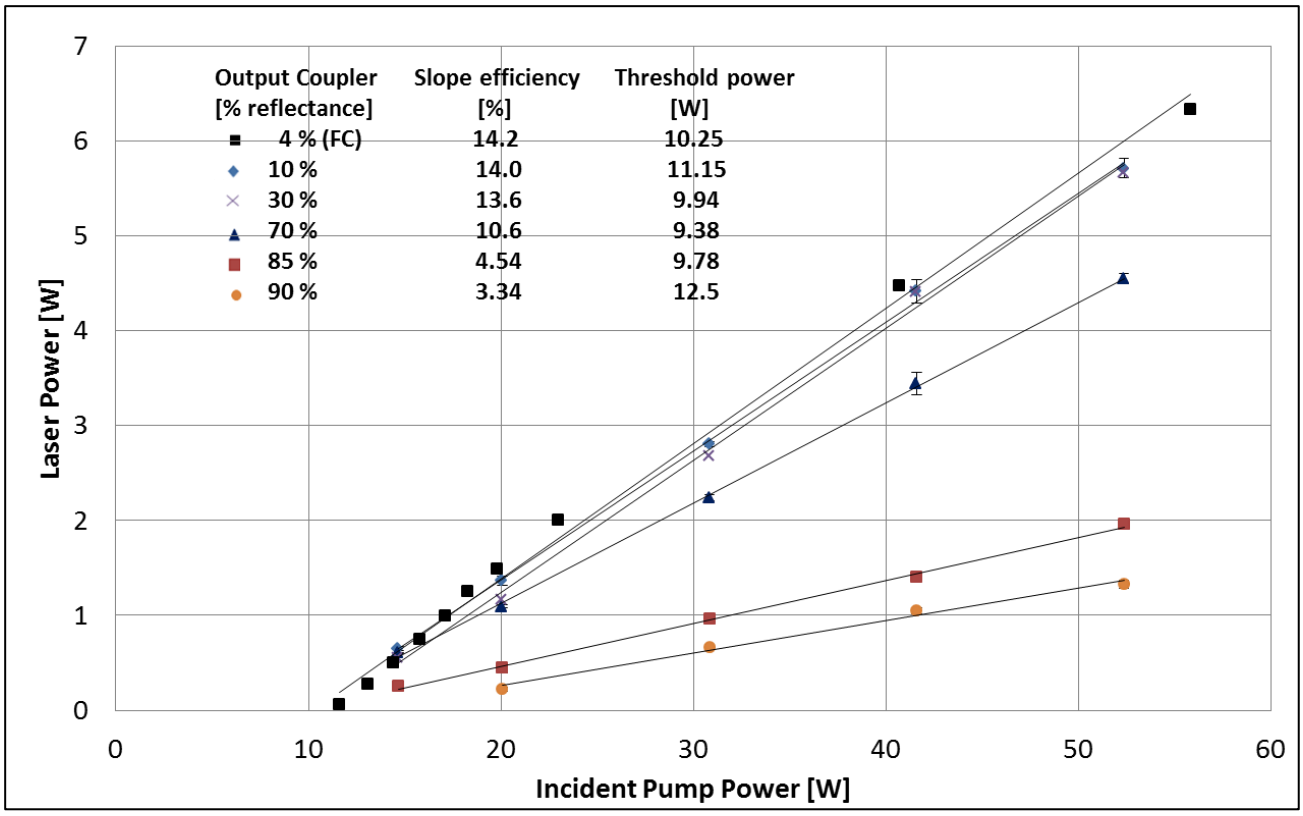

Figure 31: Laser output powers as a function of incident pump power for various output couplers butted against the flat cleave output.

Spectroscopic measurements were performed with a flat cleave (4 %), 30 %, 70 % and 90 % reflectance output couplers. The tests were performed with 43.5 W of incident pump power. Spectroscopic measurements were collected with an Avantes NIR256-2.5TEC spectrometer. The spectrometer had a spectral resolution of 4 nm and the integration time was set to 2 ms for near

real time analysis of the output spectra. Figure 32 shows the output spectra for the various output couplers.

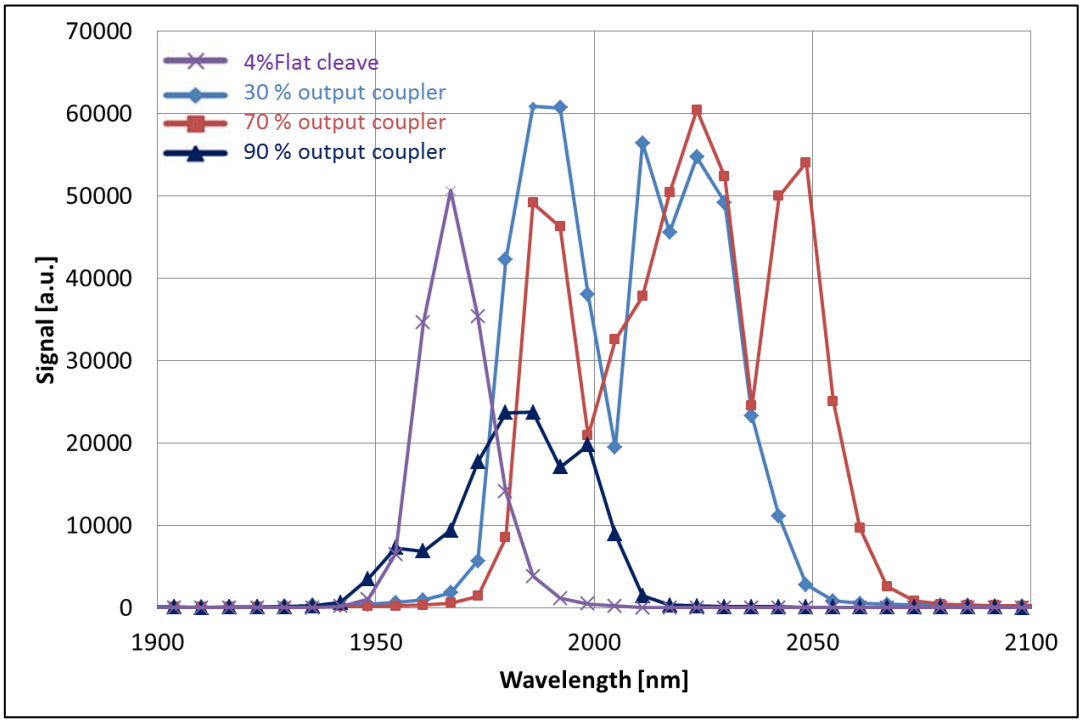

Figure 32: Spectral output for of the short fibre laser with various output couplers at 43.5 W of incident pump power.

A measurement of the residual pump power (unabsorbed) is illustrated in Figure 33.

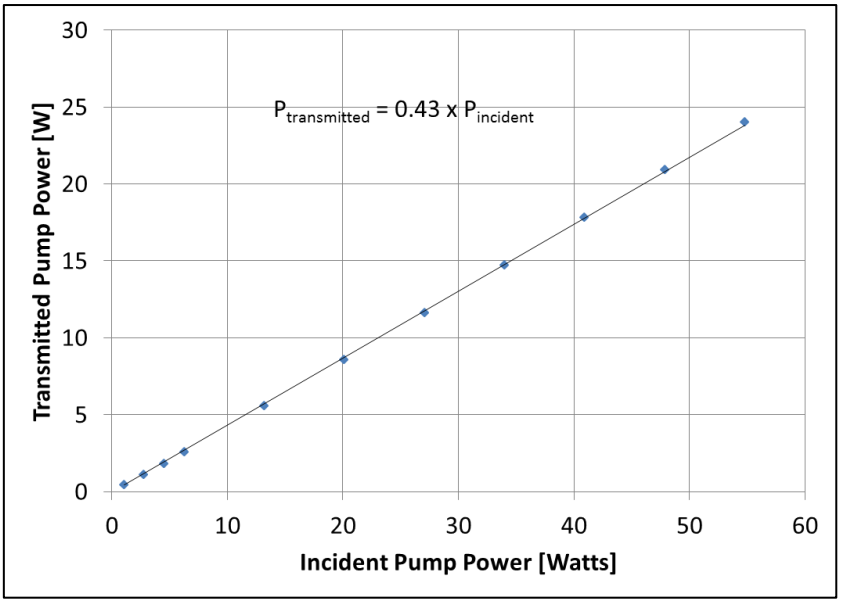

Figure 33: Plot of the residual pump power measured against the launched pump power.

Real time analysis of the output laser spectra revealed the following; The laser output spectra with the flat cleave as output coupler was mostly single peaked (at the resolution) and temporally stable. The peak would occasionally split into two peaks increasing the full width at half maximum (FWHM) measurement. The output spectra with 30 %, 70 %, and 90 % output couplers had multiple peaks (Figure 32) which were temporally unstable. The temporal instability was observed as multiple peaks interchangeably rising and diminishing. Laser output power was highest with the flat cleave as output coupler (Figure 31). The temporal instability is illustrated in figure 34 which is a time series of sequential spectral measurements (T1 through T4) measured at arbitrary time intervals. A 70 % output coupler was used for the measurements.

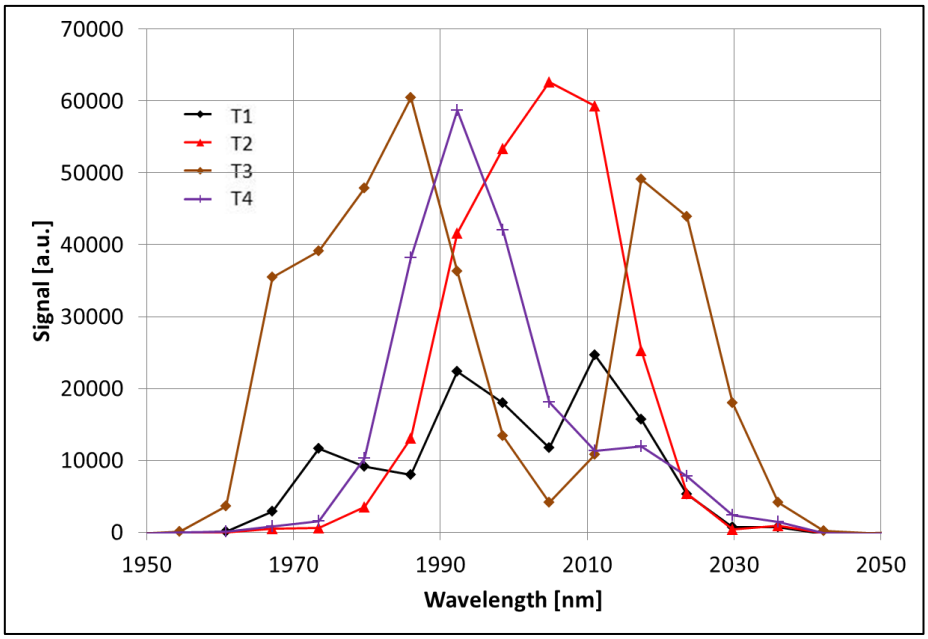

Figure 34: A time series of sequential spectral measurements (T1 through T4) measured at arbitrary time intervals

The laser output power was also most stable with the flat cleave as output coupler (~4 %) where negligible power fluctuation was observed. The power instabilities can be seen as error bars in Figure 31.

Thulium lasers are prone to reabsorption due to their quasi three-level nature [75]. Reabsorption of laser photons as they traverse the laser cavity shifts the output laser spectra to longer wavelengths with lower effective absorption cross sections. The wavelength shift due to reabsorption has been shown to increase rapidly after 1940 nm [76]. Addition of an output coupler to the laser system increases reabsorption due to the increase in the average photon cavity lifetime. This can be seen in Figure 32 where increasing the output coupler reflectance with the exception of the 90 % output coupler, shifts the output spectra to longer wavelengths. The 90 % output coupler produced the lowest output power (Figure 31) indicating that stimulated emission was limited and therefore the laser output had high ASE content. Peak broadening with increased output coupler reflectance was also observed, further evidence of reabsorption effects in the TDFL.

The decreased power with increased output coupling reflectivity (Figure 31) is consistent with reported literature. Comparison of a 4 % (flat cleave), 5 % and 10 % as output couplers in a 2 wt. % doped TDFL has been reported by Tang and Xu [77]. The reported data from this paper indicates that the slope efficiency was highest with a flat cleaved as output coupler despite an increase in the threshold power. Comparison of the slope efficiencies and threshold power (Figure 11), shows the same trend. In a paper by Zhang et al. output coupler reflectance is varied by polishing the fibre tip facet at angles of 0, 5.4, 25.5 and 40.4 degrees [74]. Again the 0 degree (flat cleave) polished fibre face resulted in the highest measured slope efficiency.

3.3.2 Effect of air cooling on power, temporal stability and spectral output

In this experiment the effect of cooling on temporal stability and laser efficiency was investigated. The aim of the experiment was to assess the relationship temperature related reabsorption affects the temporal stability of the TDFL laser output. This was achieved by measuring the laser spectra, laser output power, and temporal stability of the laser with and without air cooling. Measurements were performed for the free running laser and wavelength selected (1939.8 nm VBG) laser outputs.

The laser was set up in configuration 3 (Figure 29(iii)) with the TDF wrapped around an aluminium mandrel. Active cooling was provided by two 5 W fans (Figure 30) which were directed at the pump input end of the fibre where fibre temperatures would be at their highest. The free running laser had a HR mirror as optical feedback element which was later swapped out with a VBG for wavelength selection. The VBG was set up for first order reflection at 1939.8 nm. Output stability was measured with a 20 MHz Thorlabs InGaAs photodetector connected to a 1 GHz Tektronix oscilloscope.

Figure 35 shows the slope efficiency measurements for the air cooled and uncooled TDFL. Both sets of measurements were performed for the free running TDFL and with the VBG as optical feedback element. Air cooling of the TDFL improved the slope efficiency of the laser for both the HR mirror and VBG as intracavity optical feedback elements.

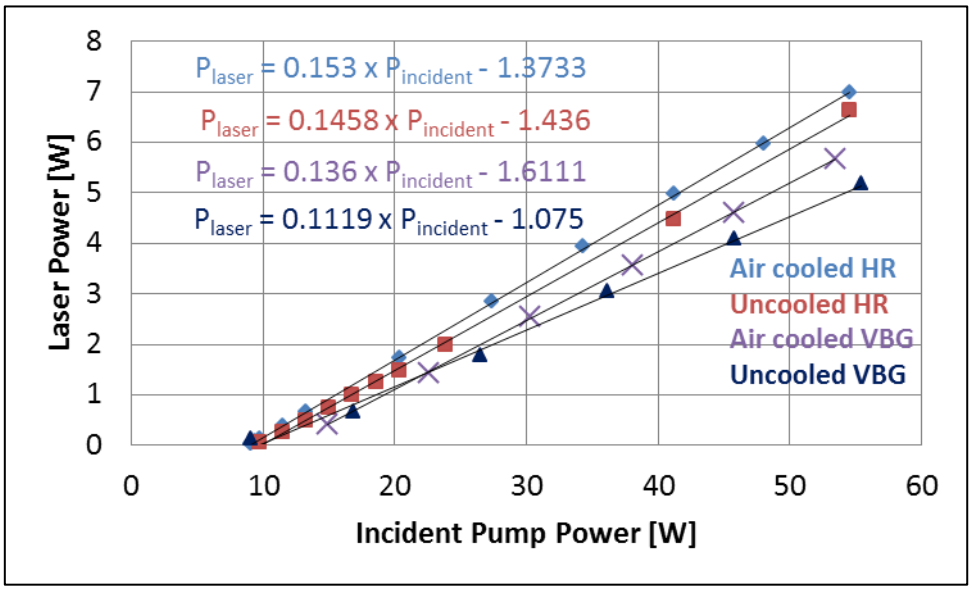

Figure 35: Slope efficiencies for the air cooled and uncooled laser with an intracavity high reflector mirror and VBG.

At low pump powers, irrespective of the presence or absence of cooling or intracavity feedback element, the TDFL output was self-pulsing. Figure 36 shows a typical low pump power, pulse train measurement. For this measurement, the laser was air cooled and optical feedback was provided by an intracavity HR element. The measurement was taken with the pump power approximately 1.17 times the laser threshold incident pump power (~9 W). Pulse lengths and repetition rates were approximately 2.5 µs and ~175 kHz respectively.

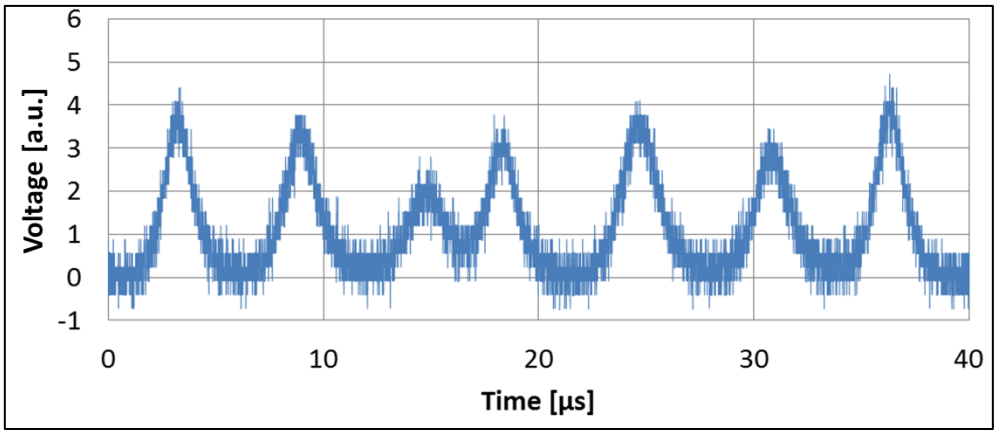

Figure 36: Typical self-pulsing pulse train observable at 1.17 times the laser threshold incident pump power.

Figure 37 and Figure 38 are laser output stability measurements for the air cooled and uncooled laser with an intracavity HR mirror and VBG, respectively. Increasing the pump power reduced the pulse lengths to ~1.7 µs and increased the repetition rate to ~550 kHz as in Figure 37 and Figure 38 where the 43.5 W of pump light was 5.5 times greater than the threshold pump power. Quasi cw

output was only achieved for the air cooled systems at pump powers 5.5 times the laser threshold pump powers. Output power also improved with air cooling. The highest output power (7 W) and slope efficiency (15.3 %) was recorded when the laser was air cooled with optical feedback from intracavity HR mirror (Figure 35). Spectral broadening was reduced under air cooling and displayed less peak splitting of the peak centred at ~1970 nm (Figure 39).

There was no visible improvement on the temporal stability of the laser output with the introduction of a VBG. This can be seen by comparing the uncooled temporal outputs in Figure 37 and Figure 38 indicating that longitudinal mode instability had little impact on output laser's temporal stability.

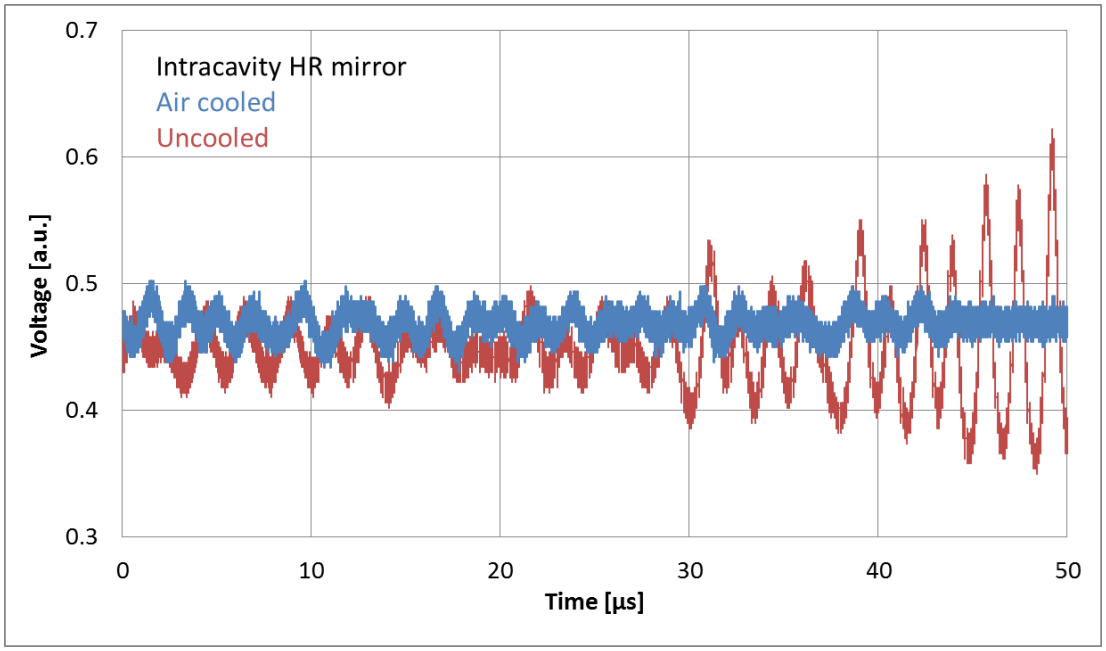

Figure 37: Temporal stability for the air cooled (blue) and uncooled (red) laser with an intracavity high reflector at 43.5 W of incident pump power.

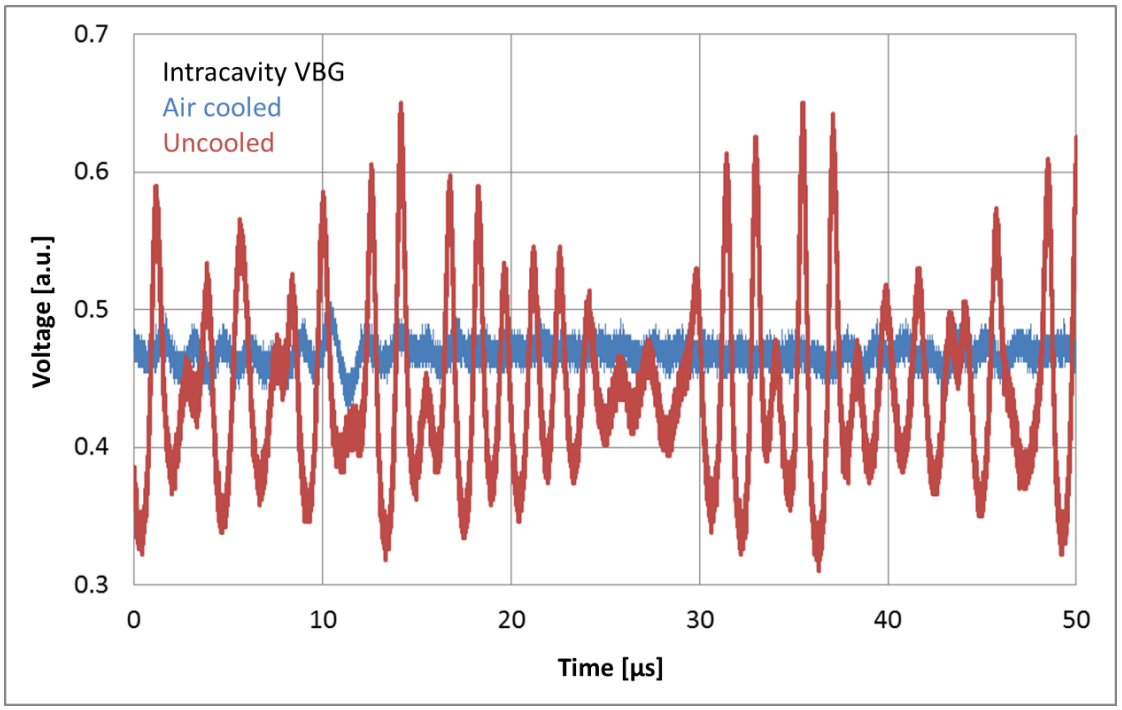

Figure 38: Temporal stability for the air cooled (blue) and uncooled (red) laser with an intracavity VBG at 43.5 W of incident pump power.

The laser output spectra of the uncooled and air-cooled systems are shown in Figure 39. The measurements were performed with an Avantes NIR256-2.5TEC spectroscope. Measurements were first performed with the HR mirror providing optical feedback. The integration time on the spectroscope was set to 2 ms and pump power to the laser was 43.5 W. When the laser was uncooled, peak splitting (at the resolution) was observed. Turning the fans on (air cooling) collapsed the split peak into a single peak effectively narrowing the output spectra. Spectroscopic measurements were also performed with 1939.8 nm VBG as the optical feedback element. Irrespective of cooling, the output spectrum with the VBG was observed to be narrower and more stable than in the previous measurements.

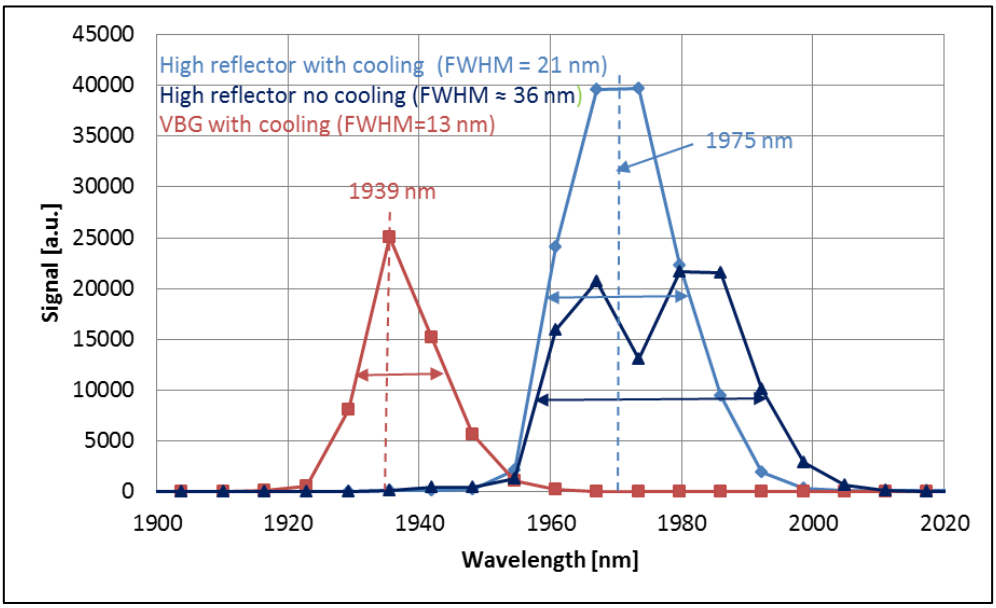

Figure 39: Output laser spectra for the air cooled and uncooled system with an intracavity high reflecting mirror and VBG at 43.5 W of pump power.

TDFL laser output transitioning from a self-pulsing chain to a quasi cw laser output with increasing pump power has been reported in literature [78]. As discussed in section 1.6, the TDFL behaves as though the unpumped regions of the fibre acting like a saturable absorber. Increasing the pump light intensity reduces this "saturable absorber effect" and hence the laser output transitions to quasi cw. It was further discussed in section 1.6 that possible dynamical loss mechanisms leading to saturable absorption effects were related to reabsorption effects in the TDFL.

Experimental results taken with this short "test" fibre, seem to further indicate that self-pulsing is indeed related to reabsorption effects. As discussed in section 1.3, for quasi 3-level systems there is always a possibility of having electrons present in the Stark split lower laser manifold at any given temperature. Insufficient cooling of the TDFL further increases the likelihood of electrons populating the lower laser energy manifold increasing laser reabsorption. Comparison of the cooled and uncooled spectra with intracavity HR mirror (Figure 39) indicates that there is a slight shift of the central wavelength to longer wavelengths (~1970-~1975 nm), and peak broadening in the uncooled scheme. This change in output spectra shows that reabsorption effects are enhanced in the uncooled TDFL scheme (Figure 37 and Figure 38). Since the threshold at which the laser output transitions from self-pulsing to quasi cw is also increased for the uncooled TDFL scheme, it seems plausible that reabsorption effects could be directly related to the self-pulsing behaviour in TDFLs.

The reduction in slope efficiency with the intracavity VBG, evident in Figure 35 is most likely not due to the spectral shift from the natural lasing wavelength (~1970 nm) to (≈1940 nm) as there is an increase in the emission cross section and reduction in the absorption cross section at this wavelength [16]. Instead, it is probably due to the diffraction efficiency of the VBG introducing approximately 9 % extra loss to the fibre cavity [46] (Appendix B). Evidence of possible light

scattering off the 1939.8 nm VBG is covered in section 3.3.5. It was also found that although addition of a VBG improves the spectral stability of the laser, it had little impact on output laser stability. The slope efficiency of the air cooled TFDL with an intracavity VBG was ~12 % less than the air cooled free running laser. For applications requiring output laser wavelengths at 1939.8 nm, this is an acceptable loss considering the diffraction efficiency of the VBG.

It can be concluded from this experiment that even moderate cooling schemes (air cooling) affected the temporal behaviour and pump to laser conversion efficiency of the TDFL. Also, there is sufficient evidence from this experiment and literature (section 1.6) to suggest that TDFL temporal stability improves when there are less “unpumped” regions in the fibre. It can therefore be concluded that mitigation, or at least, reducing reabsorption affects is imperative for temporally stable and efficient pump light to laser conversion. This can be achieved with an adequate cooling and if possible, a pump scheme that allows for better distribution of the pump light in the TDFL. The exact amount of cooling and pump distribution required for optimal TDFL performance remains unclear.

3.3.3 TDF length and cavity considerations

Thus far, only output couplers reflective to the laser wavelength and transmissive to the pump wavelength have been considered. For such cavities, higher reflectivity output couplers (> 4 %) promote laser signal reabsorption which reduces laser efficiency. Output couplers that are highly reflective to the pump light (retro reflectors) also need to be considered. Longer TDF’s where residual pump light is minimal will not benefit from such a pumping scheme, however, shorter fibre lasers with higher levels of RPL could. By retro reflecting the pump light shorter fibres could be implemented with similar output laser efficiencies and powers. Also the temporal stability would improve due to reduced reabsorption losses in the lesser pumped regions of the TDF.

The “test” TDFL could not be used for this experiment because the RPL levels were too high (43 %, Figure 33) and retro reflecting the RPL would be detrimental to the FCLD. From literature [73] shorter TDFLs with retro reflecting pumping schemes performed similarly to longer fibres in terms of laser efficiency. This is to be expected since the total amount of pump light absorbed by the fibre will be similar. However, high efficiencies were only obtainable when the output couplers reflected between ≥ 10 % and ≤50 % at the laser signal wavelength. By comparison, longer fibres are more efficient in combination with low output coupler reflectivities, such as a 4 % flat cleave. Power scaling limitations also need to be considered when choosing the correct TDF length and cavity configuration/pumping scheme. For retro reflected pumping schemes (high RPL), the maximum amount of pump light is limited. This is because too much pump light will damage the FCLD.

When considering longer TDF’s, lower reflectivity output couplers have been shown to supress temporal instabilities such as self-pulsing [73]. The length of the fibre should also not be too long as this leads to reabsorption of the laser signal and hence, a reduction is laser efficiency [77,79]. Another consideration when choosing the optimal fibre length is the desired output laser wavelength. Longer fibres, due to reabsorption effects generally favour longer output laser wavelengths. The tuneable range (spectral range) lies between ~1850 nm to ~2050 nm [57]. Short

40-150 cm, single mode, TDFLs have been demonstrated to have output laser wavelengths in the range of (1840-1940 nm) [80] and longer 5 m fibres lase at around 2042 nm with similar slope efficiencies but vastly different output powers.

For this dissertation a longer fibre (~4 m for the LMA 25/400 TDF) with a low reflectance output coupler (4 % flat cleave) was decided upon for the following reasons: Implementing a flat cleave as an output coupler simplifies the laser design since there is no need for an output coupler mirror or FBG. This cavity configuration would not compromise the laser's efficiency and allows for scaling to higher laser output powers. Temporal stability with this cavity configuration was expected to be sufficient since cw laser output was expected at high levels of pump power.

3.3.4 Beam quality

The beam quality factor of the TDFL set up in configuration 3 with an intracavity VBG was measured. Details of the measurement technique are covered in section 2.5. The measurements required for the determination of the beam quality factor are illustrated in Figure 40.

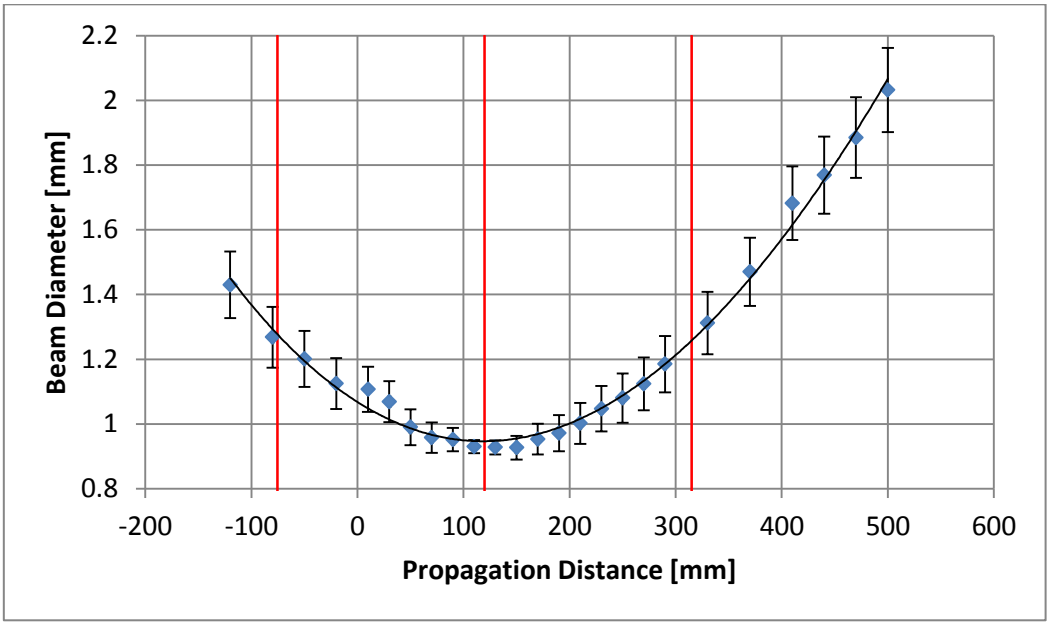

Figure 40: Second order polynomial fit for beam quality factor measurement performed for the air cooled TDFL in configuration 3 with an intracavity VBG.

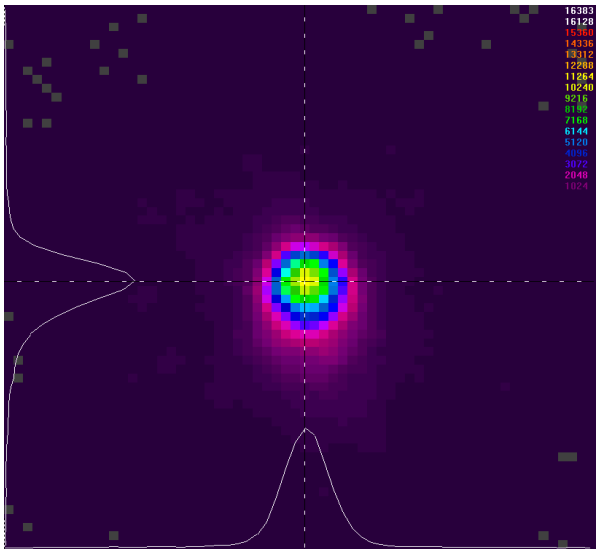

Figure 41: Profile of the beam waist of the air cooled TDFL in configuration 3 with an intracavity VBG at 60 W of pump power and 6.6 W of laser output power.

The M^2 value was measured to be ≤ 1.6. A contributing factor to the less than ideal beam quality was thermal blooming. Thermal blooming was observed and identified by its characteristic, time dependent distortion of the output beam. The thermal blooming effect occurred due to the overlap of the lasers 1939.8 nm VBG output overlapping with atmospheric water absorption lines (Figure 12) [36]. The presence of cladding light is also visible in Figure 41. Cladding light is weak multimodal cladding modes most likely caused by spherical aberrations of the collimating lens (L3 in Figure 41) or backscatter from the VBG optical feedback element being amplified by the TDFL.

3.4 Conclusions

From the experiments covered in this chapter, several outcomes concerning the development of a high power TDFLs are considered. From the cavity optimisation experiment it was concluded that implementation of a long TDFL with a low reflectivity output coupler was favourable for scaling to high laser output powers. From the second experiment which focused on the effect of cooling on laser efficiency, temporal and spectral stability, it was found that the temporal stability and slope efficiency of the TDFL improved when cooled. Spectral stability was shown to be most stable with the implementation of a VBG. However, introducing the VBG reduced laser efficiency by approximately 8 %. The beam quality measurement revealed that cladding light was present in the laser output. The cladding light could be introduced via scattering or spherical aberration from the collimating lens L3 (Figure 29) or light backscattered off the VBG. Laser efficiencies in these experiments was low, this was due to the relatively short length of LMA TDF used in the experiments. Measurements of the residual pump light with the laser setup in configuration 3 and intracavity VBG revealed that 43 % of the coupled pump light was not being absorbed (Figure 33). Increasing the fibre length will increase pump absorption and hence laser efficiency.

Chapter 4: Development of a high power cw TDFL

4.1 Introduction

In chapter 3, the performance of a TDFL was evaluated with respect to the temporal stability of its output power, laser efficiency, spectral stability, and beam quality. Based on these results, the recommendations were to increase the Tm-doped fibre length to increase pump absorption and therefore improve laser efficiency, implement an effective cooling scheme to reduce reabsorption thereby improving laser efficiency and laser output temporal stability, introduce a VBG to improve the lasers spectral stability, and improve the beam quality by introducing appropriate lenses for intracavity optical feedback. In this chapter, these recommendations were implemented into the design and demonstration of a high power, high efficiency cw TDFL.

In this experiment, the aim was to develop a high power (±60 W) cw TDFL. This laser could then later be used for experiments requiring 2 µm wavelength laser output. One possible experiment would be an atmospheric transmission experiment utilising the 2 µm wavelength laser output. Atmospheric propagation experiments have been performed with a 25/400 LMA TDF [81]. Such a laser would need to have high output power (>200 W), be tuneable (grating or VBG) and preferably be portable (robust and compact). To this end a bespoke VBG, wavelength selective for first order reflection at 2036.1 was procured. This particular experiment is outside the scope of this dissertation, and instead the effect of this VBG on temporal stability, spectral stability, beam quality and output laser efficiency was analysed.

4.2 Experimental setup and procedures

In this section, the various components and design considerations relating to the TDFL thermal management scheme are discussed. Experimental results and discussions related to thermal management are also covered.

4.2.1 Thermal management of the Tm-doped fibre

As demonstrated in chapter 3, cooling of the TDF is essential for efficient pump to laser output conversion [76]. An in-house cooling system was developed consisting of 13 cm diameter, solid aluminium mandrel and copper fibre holders. The base of the mandrel was 0.8 cm thick and 16 cm in diameter. Four holes were machined into the base for attaching the mandrel to a water cooled optical breadboard. A 600 by 600 µm, square cut groove, was spirally machined into the mandrels outer surface. The groove allowed for the ~550 µm diameter (with coating) TDF to be wrapped around the mandrel. To effectively cool the fibre holder at the pump input fibre end where cooling is most critical, the author designed a 12 cm long copper fibre holder with a water cooling channel and

a rounded end and copper lid to fully enclose the fibre. A square groove (700 by 700 µm) large enough to house a recoated fibre (diameter 650 µm) was machined into the copper holder. A second, 12 cm long, copper holder with the same groove diameter was designed for the pump output end of the fibre. This holder was not rounded and had no lid because cooling at the pump exit end of the fibre is not as critical. A water cooling channel was included for the initial design of this holder (Figure 43) but later deemed unnecessary. A CAD rendering of the rounded end, copper fibre holder in its assembled and disassembled form is illustrated in Figure 42.

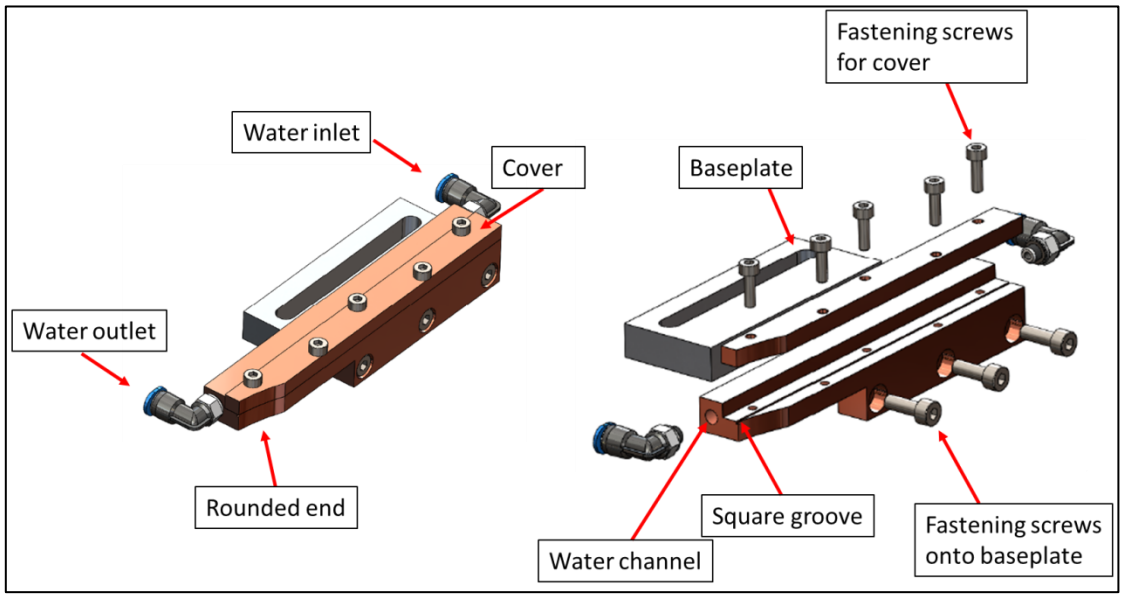

Figure 42: (left) CAD rendering of the assembled copper fibre holder with rounded end and water cooling channel. (right) Disassembled view.

The diameter of the rounded fibre holder matched that of the aluminium mandrel for a flush fit with the fibre positioned tangentially to the mandrel. This ensured that the entire input end of the TDF was in thermal contact with cooled surfaces. A CAD rendering of the assembled cooling system and wrapped TDF is illustrated in Figure 43.

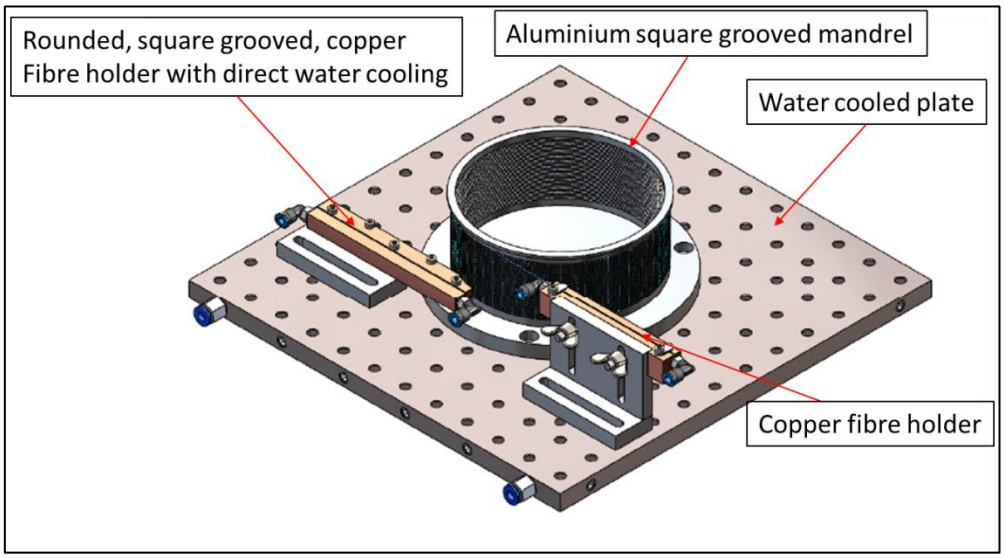

Figure 43: CAD rendering of the cooling scheme implemented in the development of the high power TDFL.

Chilled water was supplied to the various cooling components by a Neslab chiller, at a flow rate approximately 2 L/min. To determine which temperature the chiller should operate at, a simple fibre laser was built with the unspliced TDF and the output lasing power monitored at several temperature and power supply current set points. The results are shown in Figure 44.

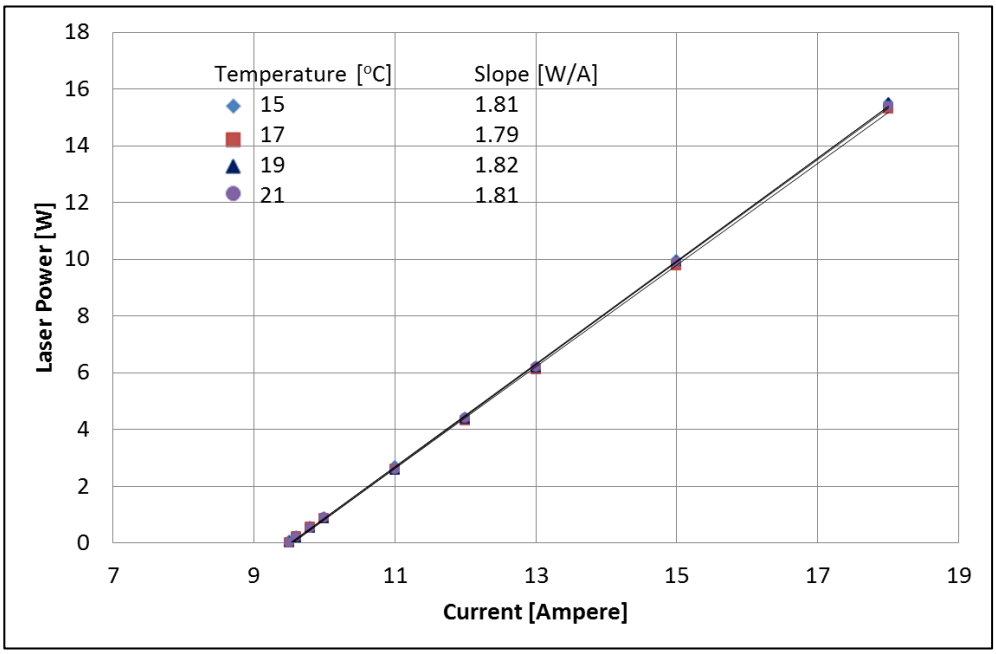

Figure 44: Laser output power at various current and chiller temperature settings.

There was no discernible difference in the average output lasing power at the various temperature settings. By comparison, the common choice of temperature settings as seen in literature is in the 10 to 20 ^{o}C temperature range [37,60], [78–89].

It was decided to set the chiller temperature to 16 ^{o}C. At this temperature, the TDFL would be cooled sufficiently to reduce reabsorption affects, but not so cool that at any given time, the temperature would be below the dew point of the laboratory causing water condensation on the TDFL setup.

4.2.2 Thermal management of the TDF tip

The pump power available for the experiment was ~130 W and it was uncertain what effect this level of pump power would have on the Tm-doped fibre. If the Tm-doped fibre, set up in the new cooling scheme was able to withstand ~130 W of pump power, development of the TDFL at the corresponding power level, would be simplified. It was therefore necessary to know, at which pump power levels thermal management of the Tm-doped tip would become a necessary consideration in the fibre laser design.

To test this, the fibre was set up in configuration 1 (Chapter 3), as illustrated in Figure 45. The laser cavity consisted of a butted dichroic mirror, DM2, and a flatly cleaved fibre end as output coupler. Approximately 2 cm of the low index polymer coating was stripped off the fibre tip at the pump input fibre end to avoid burning the coating. The fibre ends were clamped into their respective holders with only the stripped tips protruding. Pump light from the FCLD was then coupled into the Tm-doped fibre and laser action induced.

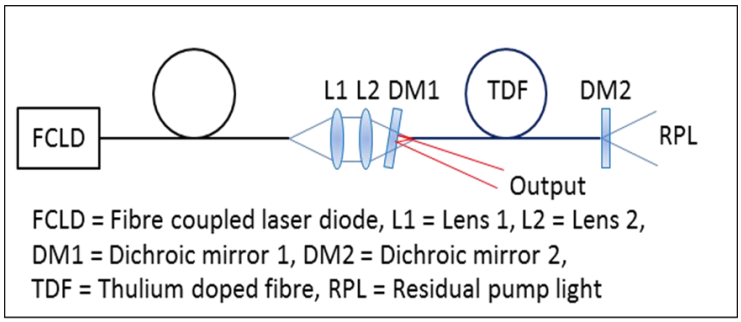

Figure 45: Laser configuration for testing the thermal load limits of the TDFL fibre tip.

The pump light was increased incrementally until catastrophic, thermally induced damage 3 mm from the fibre facet was observed with ~56 W of incident pump power (Figure 46). It is possible that the damage occurred at the focal point of the pump light.

A second test was performed with 3 mm of the fibre tip protruding the holder. This increased the damage threshold to ~70 W of pump light before the fibre tip shattered.

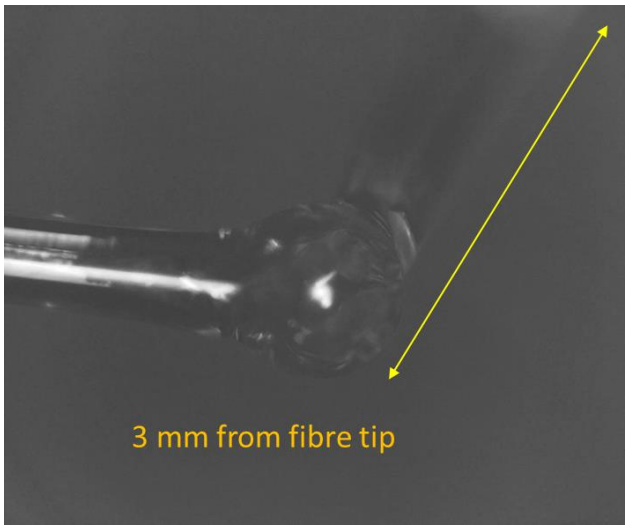

Figure 46: Thermally induced damage of the TDFL tip without splices at approximately 56 W of pump power.

Possible explanations for the thermally induced damage are as follows. Thulium-doped fibre lasers pumped at 793 nm, have relatively poor quantum defects [94] despite their CR assisted high quantum efficiencies. The excess energy is converted into heat by non-radiative decay processes. They also exhibit a thermally dependent emission cross section which deceases with increased heat. The reduced emission cross section will reduce stimulated emission processes and therefore useful energy extraction by way of laser action. As a result of the poor quantum defect and reduced stimulated emission cross section, heat rapidly increases at the fibre tip where pump light is most intense [94].

It was concluded from this experiment that thermal management of the fibre tip is imperative for scaling to high laser powers.

4.2.3 Splicing

To overcome thermal damage at the fibre tip, a length of mode matched, 0.5 m long passive fibre was spliced (joined) to the TDF (Table 2). The spliced fibres could then be recoated at the splice joint. Splicing of the TDF to a passive fibre followed by recoating of the splice joint had two distinct advantages pertaining to thermal management of the fibre tip. Firstly, the pump light intensity entering the doped fibre via the spliced passive fibre is less intense. Before splicing, the one to one magnification pump coupling lenses focused pump light into the doped fibre tip with a beam diameter of ~200 µm. After splicing, pump light entering the TDF will have a beam diameter approximately equal to that of the cladding diameter (~395 µm) reducing the initial pump intensity by a factor of ~4. This reduction in pump light intensity increases the level of pump light intensity required before the onset of thermally induced damage. Secondly, and most significantly, the recoated, spliced region could be placed in a copper holder allowing for active cooling of the entire Tm-doped tip.

Recoating of the spliced region has two additional benefits. The tough, flexible, low index polymer assists with flexibility at the splice reducing the chances of accidental flexing and breaking at the splice joint. It also reduces the chances of decoupling or scattering pump light when other materials come into contact with the surface of the fibre cladding.

The outer cladding diameter of the mode-matched passive fibre was ~395 µm, slightly less than the 400 µm cladding diameter of the TDF. The slight reduction in cladding diameter is to assist with pump light transmission at the splice joint. Recoating of the splice was performed with a Nufern low index polymer using a Vytran PTR-200-MRC re-coater. The parameter settings for the recoating process are listed in Appendix B.

To achieve high quality splices with low pump light and laser signal transmission losses requires splice optimisation specific to the fibre types and method of splicing. The fibre types in this experiment were the LMA 25/400 Tm-doped fibre and a mode-matched, LMA 25/395 passive fibre. The splicing method employed was fusion splicing. To avoid excessive loss of Tm-doped fibre, a "rough" optimisation was first performed between two arbitrary lengths of LMA 25/395 passive fibres. It was assumed that although the optimal splice parameter settings (fusion splicer settings) required to splice two passive fibres would not be exactly the same as between a passive fibre and the doped fibre, these splice parameter settings would be close enough to be a starting point for a "fine" optimisation process between the doped and passive fibre. The "rough" optimisation was done by comparing the images of successive splices until a visually acceptable splice was achieved. The fine optimisation was done as follows, starting with the "rough" splice parameter settings a length of passive fibre was spliced to the Tm-doped fibre. To test the integrity of the splice, a simple laser, set up in configuration 1 was built. The slope efficiency of the laser was measured with and without the splice and compared to account for any power losses incurred due to the splice. This process was repeated for various splice parameter settings until comparable slope efficiencies was achieved.

Splicing was performed with a 3SAE LDS fusion splicer [95]. The basic fusion splicing process between the two lengths of passive fibre is as follows: For each length of fibre, a fibre end was flatly cleaved and inspected under a microscope for chipping and grit on the facet. If the fibre facet was mirror like, clean, and free of chips, this end of each fibre was placed in a fibre clamp of the splicer and fastened. The pitch and yaw of one fibre is then adjusted until the surfaces of the two fibre facets are parallel. The optical axis of each fibre was then centred relative to one another (still parallel), within 2 µm of error. After alignment, the gap between the two fibres (set gap) was adjusted to 50 µm (Figure 47(f)). Heating of the fibres was done by three plasma generating electrodes, uniformly spaced about the fibre axis.

The splicing process happened in three steps: First the fibre was pre-heated. The splice parameter for adjusting the arc intensity set point and duration of the pre-heating was prefuse power and prefuse time respectively. After pre-heating one fibre would be pushed into the other. In this step the arc intensity set point, push distance and push time could be adjusted. The respective splice parameters were arc power 1, push time 1 and push distance. After pushing the fibres together,

there is a pause (no travel) at an arc power set point (arc power 2) for a time (arc time2). In this time the two fibres effectively fused together. After fusion, the fibres can be pulled at an arc power set point (pull power) for a time (pull time) over a distance (pull distance). Pulling is not required for the splicing process but rather for tapering of fibres so the splice parameters related to pulling were all set to zero. Time sequence images depicting the relevant steps in the splice process for the successful "rough optimisation" splice and associated arc power parameters are illustrated in Figure 47. Figure 49 illustrates the "rough optimisation "splice program with the relevant splice parameters. The graph is scaled according to distance in the vertical, and time in the horizontal directions.

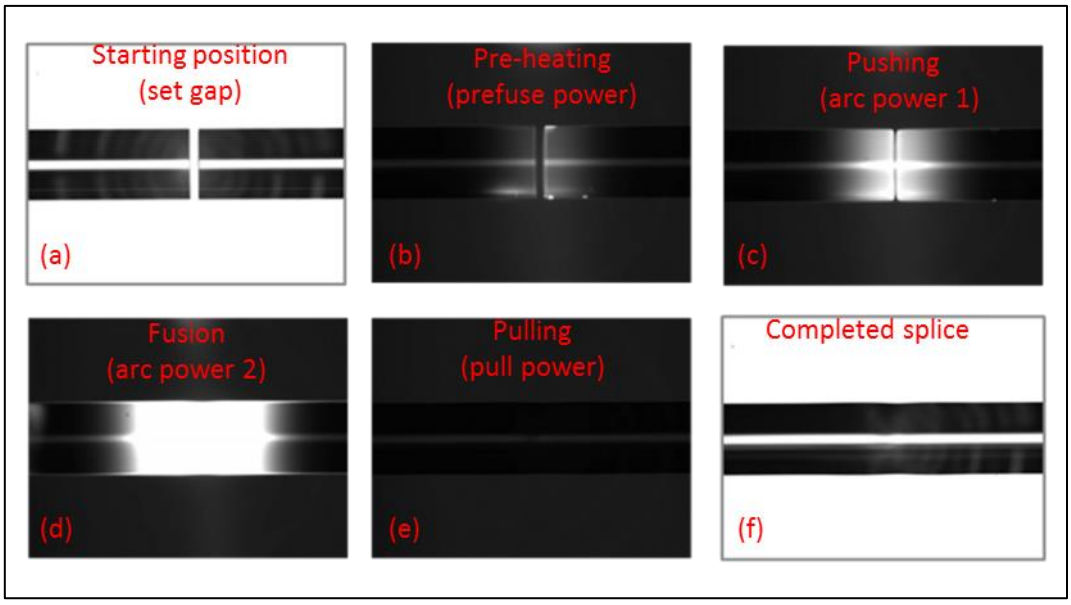

Figure 47: (from left to right, top to bottom) Time sequence images of the splicing of two mode-matched passive fibres for a rough splice optimisation. (f) A successful splice is achieved.

Splices deemed as unsuccessful had a visible seam at the splice joint and or non-parallel fibre edges. An unsuccessful splice is illustrated in Figure 48 where the edges are acceptably parallel; however, there is a visible seam at the splice joint (within yellow ellipse). It should be noted that the thick white line visible in the centre of splice images is not the fibre core but actually a lensing effect of the fibre.

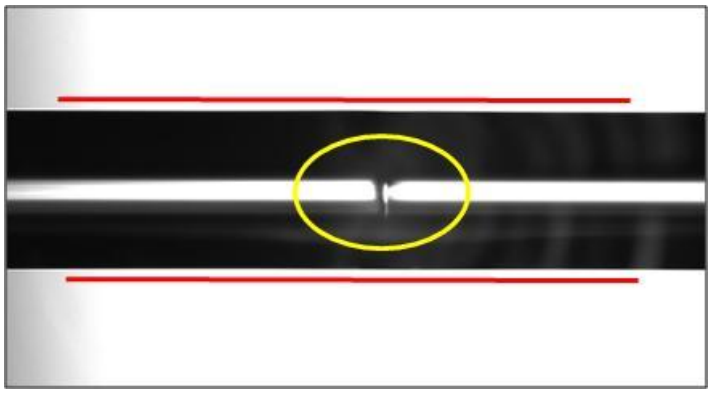

Figure 48: An unsuccessful splice for the "rough" optimisation. The fibre edges are parallel, however fusion at splice joint visible as a seam within the yellow ellipse, was unacceptable.

.

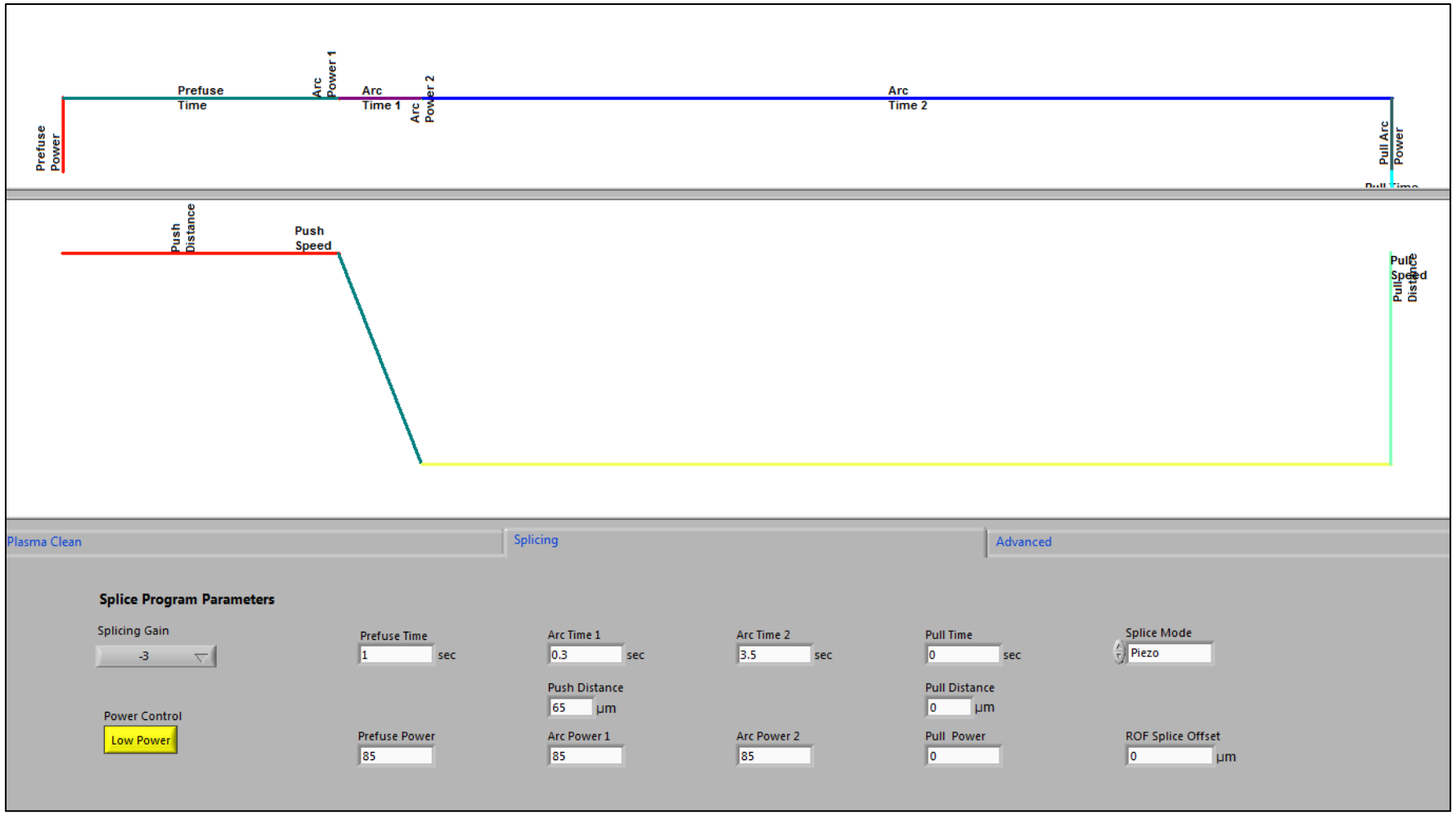

Figure 49: Splice program and relevant spice parameters used for the successful splice in the "rough" splice optimisation process.

Fine optimisation of fibre parameters was performed between the mode matched passive fibre and the TDF. The three arc power set points (prefuse power, arc power 1, and arc power 2) were kept the same for each adjustment as recommended by the supplier. Using the "rough" optimisation as the starting point (set point 85), several splices between the TDF and passive fibre were performed. Splices were performed with the smallest possible arc power increment.

After each splice, the resulting spliced fibre was then set up in configuration 1 and the laser output power measured. Power measurements were taken with the TDF in forward (splice at position A in Figure 50) and reverse orientations (splice at position B in Figure 50). That is, with a single splice located at the pump input end and at the opposite end.

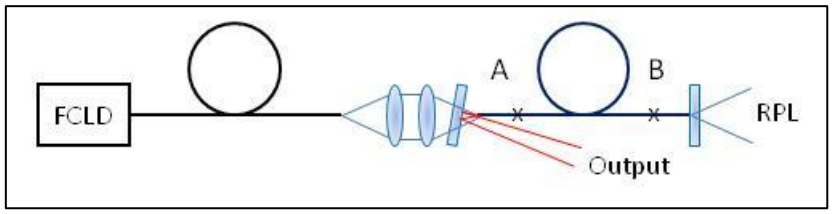

Figure 50: Fibre orientation for the fine splice optimisation measurements.

This was done in lieu of laser output measurements performed on a spliced fibre (passive to Tm-doped using factory default parameters) in the preliminary stages of the laser development. It was noticed that for poor splices performed at high arc power set points, laser output power measurements for the forward and reverse directions differed significantly, which can be explained a follows. At high arc powers the fibres fuse together at the centre of the fibre (area around the core) and less so at the extremities (outer cladding area). Light propagating down the fibre will experience little loss in the core regions of the splice and high losses in the cladding region. With a high power, poor splice oriented away from the pump source, pump light propagates down the doped fibre with negligible loss. Laser action continues in the core of the spliced fibre since the core regions of the doped and passive fibre are fused together. For the reverse orientation, significant amounts of pump light are attenuated at the splice joint before entering the doped fibre, reducing the lasers performance. An extreme example of an attempted splice performed at high arc powers is illustrated in Figure 51.

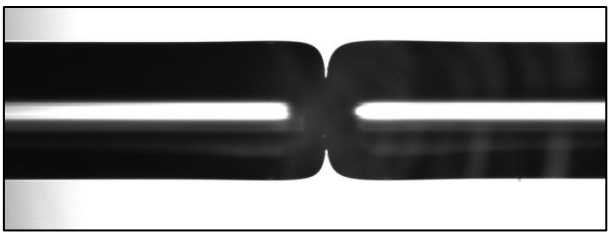

Figure 51: Unsuccessful splice attempt at a high arc power set point.

The splices performed for the fine optimisation were all of a reasonable quality and did not exhibit this problem. Double measurements were therefore taken as a precautionary measure and to increase measurement accuracy. The results of the fine splice optimisation can be seen in Figure 52.

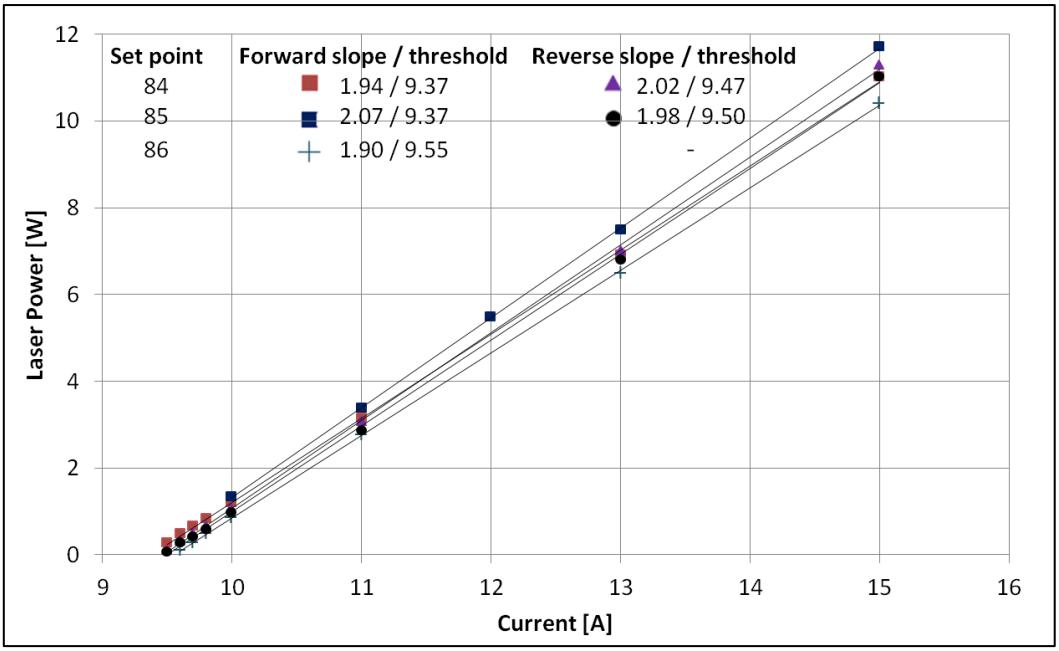

Figure 52: Laser slope efficiency measurements for the fine splice optimisation.

For each splice in the fine optimisation process, the fibre needed to be cut at the splice joint and re-cleaved before the next splice in the experiment, with each cleave removing 26 mm of fibre. If the doped fibre was re-cleaved six times in the optimisation process, the laser output power would be ~4 % lower due to the loss of doped fibre alone. To minimise these power losses and thus enable reasonable comparison between the various measurement setups, care was taken to keep the doped fibre loss to a minimum. This was achieved by cleaving the doped fibre end with the splice still attached. The loss of doped fibre was reduced from 24 mm to ~4 mm per cleave and 20 mm of passive fibre (Figure 53). A total of six cleaves were performed on the doped fibre using this technique, resulting in an overall estimated (calculated) reduction in the laser power loss of ~ 0.6 % (-0.026 dB).

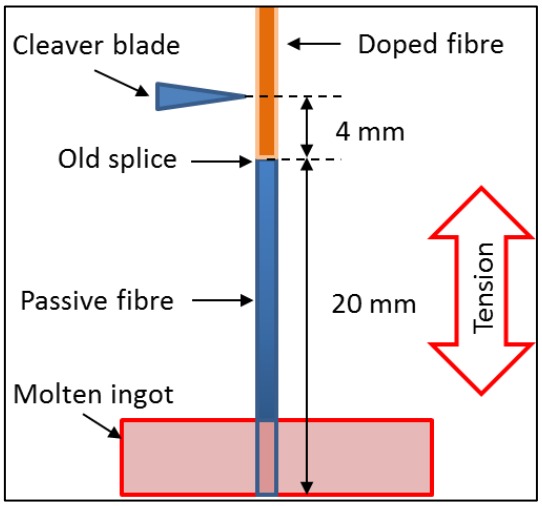

Figure 53: Illustration of the modified cleaving technique specifically devised for this work to minimise the loss of doped fibre in a splice between a doped and a passive fibre.

The arc power which resulted in the highest overall laser output power was at set point 85, the same as for the "rough" optimisation (Figure 52). This set point was used for the remainder of the splices in this dissertation.

After the fine splice optimisation, the second length of 0.5 m passive fibre was spliced to the doped fibre. The addition of the second length of passive fibre was not to address thermal damage of the fibre tip since pump light at this end of the doped fibre has been significantly attenuated. Instead it was added to conserve doped fibre length and allow for cooling of the entire length of doped fibre. Setting up the TDFL in configuration 3 requires that the fibre tip be cleaved at ~8 degrees to minimise Fresnel reflection at the tip. Several attempts at angle cleaving are usually required before an acceptable cleave is achieved. Due to the wastefulness of the process a passive fibre was first spliced to the doped fibre since shortening of the passive fibre does not reduce laser performance. Using the same rationale, any damage incurred to the passive fibre tip can simply be re-cleaved.

To effectively cool the spliced fibre within the copper holders when scaling to high pump powers (130W), a silver based thermal compound (Arctic silver 5 thermal compound) with a claimed cooling rate of 8 W/m.K and measured cooling rate of 0.9 W/m.K, was applied into the square grooves of the fibre holders. This improves the thermal contact and therefore cooling of the spliced regions within the square grooved copper holders. Application of the thermal compound within the copper fibre holder is illustrated in Figure 54.

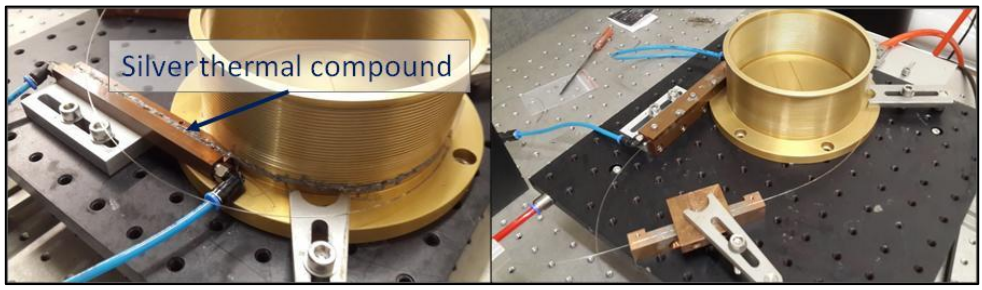

Figure 54: (left) Silver based, thermal paste applied into the holders, and (right) the complete cooling system.

4.3 Laser design

4.3.1 Fibre parameters and laser design considerations

The length of TDF used for this experiment was 3.7 m. The fibre parameters for the 25/400 TDF fibre can be seen in (Table 2). Two lengths (~0.5 m) of un-doped (passive) fibre were used in the experiment. Apart from doping, the only difference between the passive and doped fibre was the shape and slightly smaller (395 µm) inner cladding diameter of the passive fibre.

The same basic configurations listed for the short fibre laser developed in chapter 3 (Figure 29) were considered for the TDFL design. For ease of referencing they are again illustrated in Figure 55.

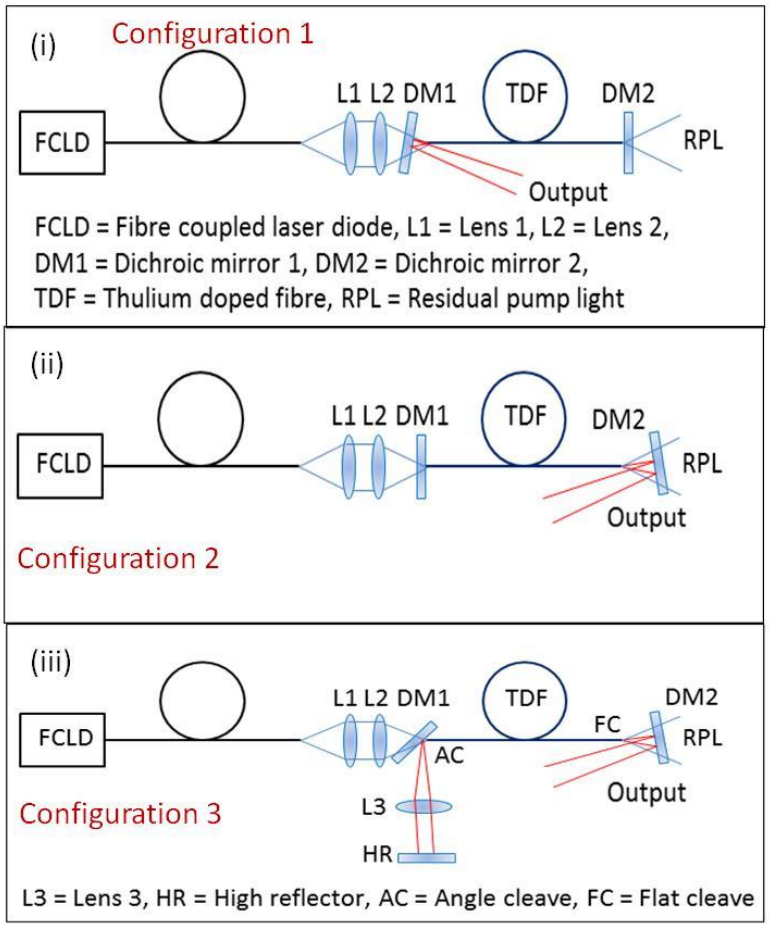

Figure 55: The various TDFL configurations used in the development of the high power cw TDFL.

Configuration 1 and configuration 2 due to the butted dichroic mirrors DM2 and DM1 respectively are relatively easy to set up. However, Configuration 1 has the distinct advantage that there is very little residual pump light in the laser output signal. The butted configuration of the high reflecting optical feedbacks elements will also reduce beam quality losses in both configurations. Configuration 3 is essentially configuration 2 with additional optical feedback elements. These optical feedback elements could also be added at the pump exit end of the fibre allowing for optical feedback of the laser signal and residual pump. Feedback of the residual pump light, which was measured to be approximately 8 % of the launched pump light, would increase the overall laser efficiency and hence increase laser output power. A bi-directional pumping scheme was also considered, however, the 8 % residual pump light was above the 5 % back reflection threshold of the Dilas FCLD's.

The different build configurations were considered and despite the possibility of increased laser output power, configuration 3 in Figure 10 was again selected; this decision was made with beam quality in mind. It was previously shown in chapter 3 that intracavity optical feedback elements may have introduced cladding modes into the laser output, reducing the TDFLs beam quality. In addition to this loss, it was expected that beam quality would be further reduced due to the addition of splices. With the addition of splices, even in lasers with excellent beam qualities ($M^2 < 1.2$), transverse cladding modes can develop [46], possibly due to core misalignment and or thermal

expansion of the doped fibre core [96,97].These are illustrated in Figure 56. A common method for removing cladding modes and residual pump light is using a cladding mode stripper[98].

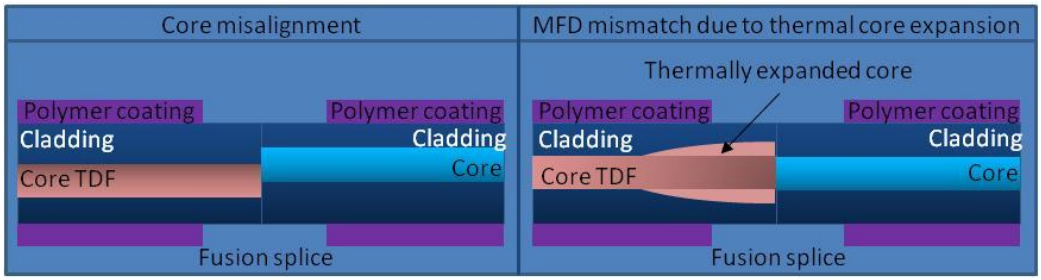

Figure 56: (left) Illustration of core misalignment and (right) thermal mismatching of the MFD, both of which initiate cladding modes in a fibre laser.

There are a variety of cladding mode stripping techniques including, chemical etching (roughing) of the fibre surface [99], re-coating or coating with a high index of refraction polymer [98] and high power monolithic cladding mode strippers [100] to name a few. The objective of all cladding mode strippers is to remove light propagating in the cladding, thus limiting the output signal to low NA signals propagating in the fibre core improving beam quality. This can be achieved by scattering light at the fibre surface (chemical etching), refracting light away from the fibre (high index polymer coatings) or attenuating the beam with a metal in contact with the cladding surface (monolithic cladding mode strippers). Figure 57 is a simplistic 2D representation of a chemically etched cladding mode stripper where it can be seen that light incident on the surface of the fibre cladding is scattered and no longer propagates through the fibre. Hence, reducing cladding modes and removing residual pump light from the laser output beam.

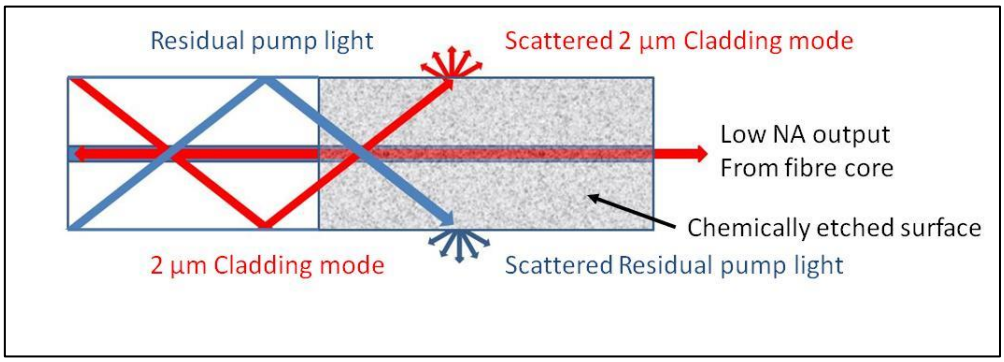

Figure 57: Simplistic representation of a chemically etched, cladding mode stripper scattering cladding light at the surface of the fibre cladding.

Due to the ease of adding a cladding mode stripper at the pump output end of the fibre, configuration 3 (Figure 55(iii)) was chosen to be the design of the TDFL. If the mode stripper was at the pump input end, pump light would be stripped off before propagating down the fibre.

4.3.2 Laser development process

All three configurations listed in Figure 55 were utilised in the development of the TDFL. Configuration 1 was used in the splice optimisation process. We now turn our attention to configurations 2 and 3. Characterisation of the TDFL set up in configuration 2 before moving over to

configuration 3 was an essential step in the TDFL development. As previously mentioned, the laser set up in configuration 2 will have excellent beam quality due to the butted configuration of the high reflecting optical feedback mirror. It can also be expected that the unspliced Tm-doped fibre set up in configuration 2 will be highly efficient since there will be no splice or optical feedback losses. This makes configuration 2 an ideal setup for comparing original beam qualities and laser efficiencies to later versions of the TDFL. This is particularly important when comparing laser efficiencies of the spliced and un-spliced versions of the laser. If the addition of splices were to significantly reduce the laser output efficiency, it could be assumed that there is significant loss of pump light or laser transmittance at the splice joint. The transmission loss will heat up the splice and potentially cause catastrophic damage to the laser at the splice joint. The Tm-doped fibre spliced to two lengths of passive fibre, set up in configuration 3 is illustrated in Figure 58. A doublet lens consisting of two 57 mm focal length lenses was implemented into the optical cavity in order to reduce aspherical aberrations as discussed in section 3.3.10.

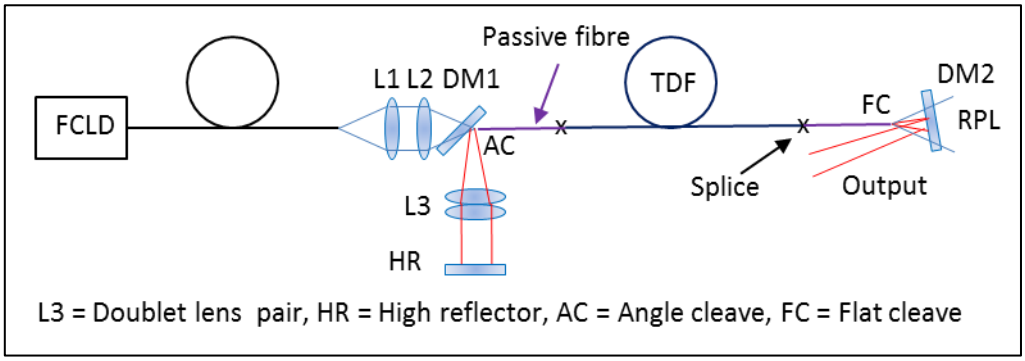

Figure 58: Tm-doped fibre spliced to two lengths of passive fibre, in configuration 3.

4.4 Experimental results and discussion

4.4.1 Laser development

The slope efficiency and beam quality factor measurements at various stages in the development of the high power cw TDFL, are illustrated in Figure 59 and Figure 60 respectively. The pump limited (117 W), highest laser output power (63 W) was achieved with the HR mirror as the optical feedback element. Average laser output power was measured to be stable. The laser was run at full power for one hour with the average output power never fluctuating more than 0.3 % above or below 63 W. The free running laser, which had a central wavelength at ~2017 nm showed no signs of beam wandering when propagating through ~2 m of free space.

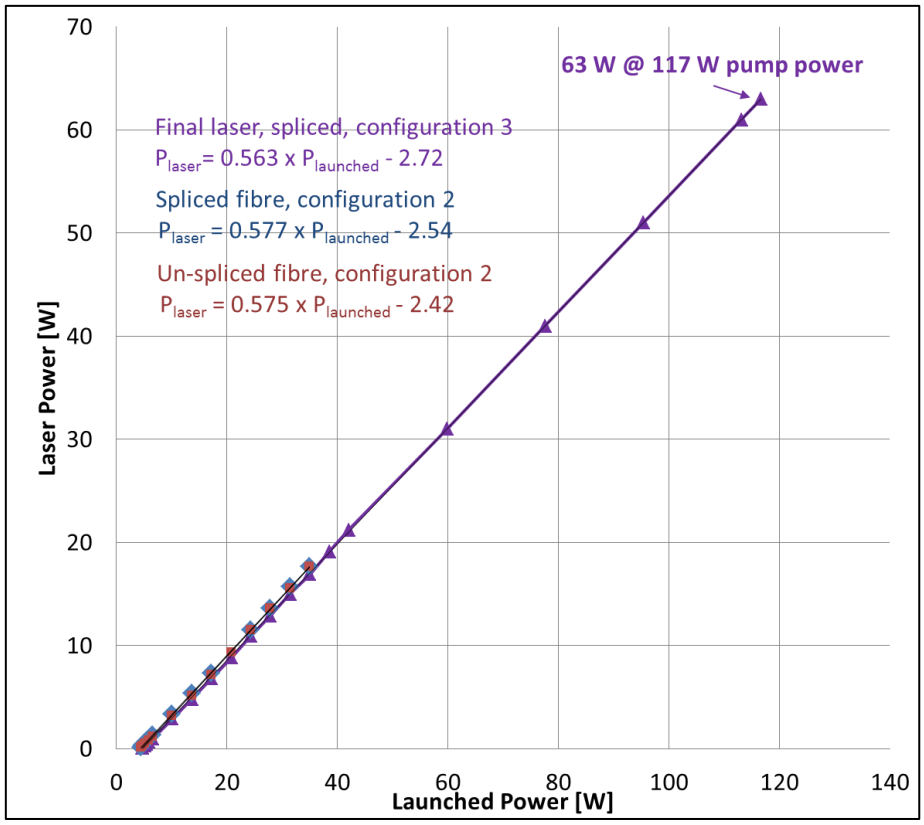

Figure 59: Comparative slope efficiencies for several reference measurements in the development of the high power cw TDFL with an intracavity HR mirror.

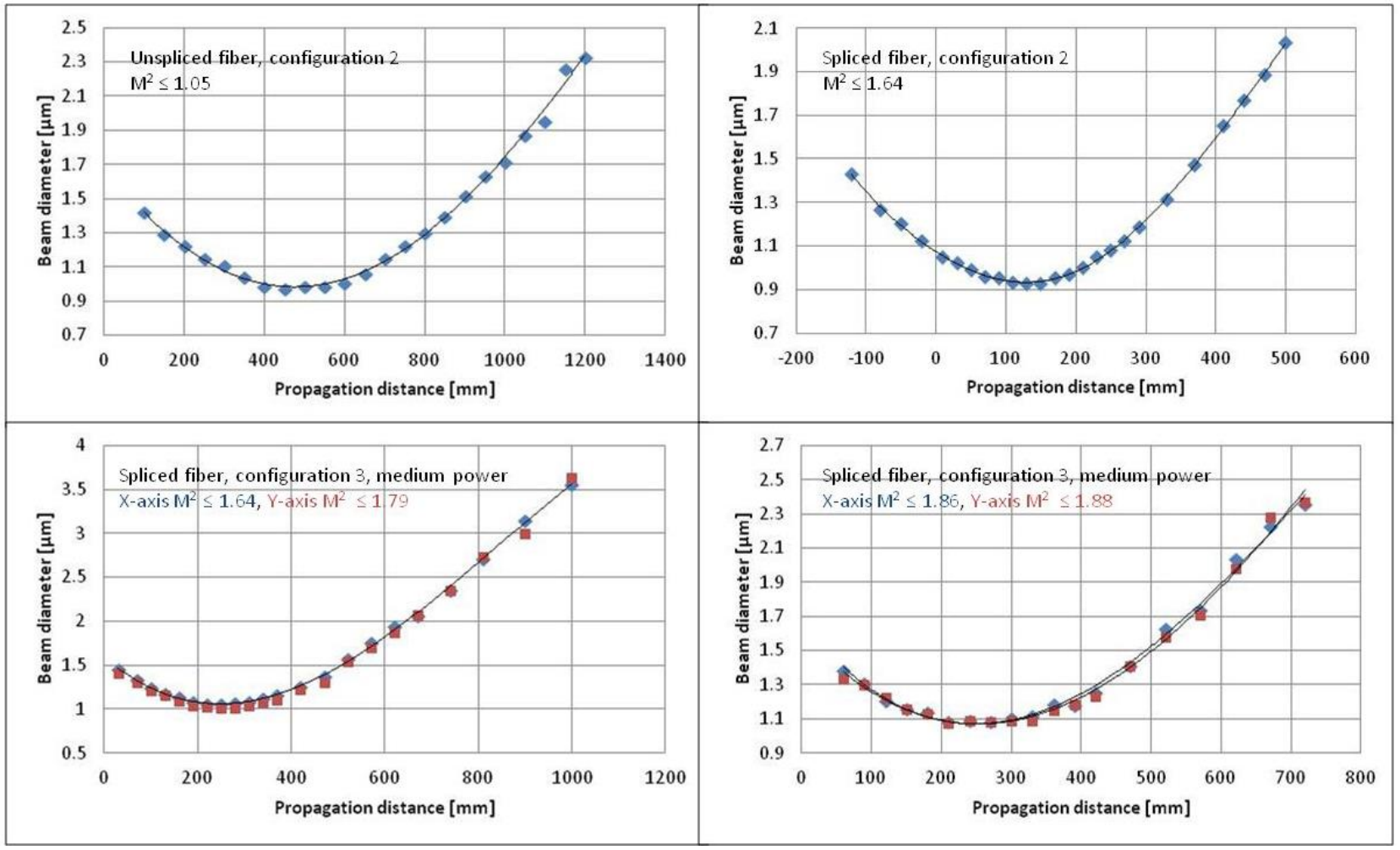

Figure 60: With reference to table 5, (top left) measurement 1, (top right) measurement 2, bottom left (measurement 3) and (bottom right) measurement 4 show comparative beam quality factors (M^2) for several measurements during the development of the high power cw TDFL.

The consolidated measurements for characterisation of the TDFL at several stages in the TDFL development process is listed in Table 6.

Table 6: Summary of measurements in the development of a CW TDFL

#	Configuration	Passive fibres attached	Threshold power [W]	Slope Efficiency [%]	Beam quality [M^2]	Pump power @ M^2 measurement [W]
1	2	N	4.4	57.5	≤ 1.05	38
2	2	Y	4.4	57.7	≤ 1.64	60
3	3	Y	4.8	56.4	≤ 1.75	60
4	3	Y	4.8	56.4	≤ 1.88	~118

Figure 61 shows several beam profiles captured on a Pyrocam III at various stages in the development of the high power TDFL.

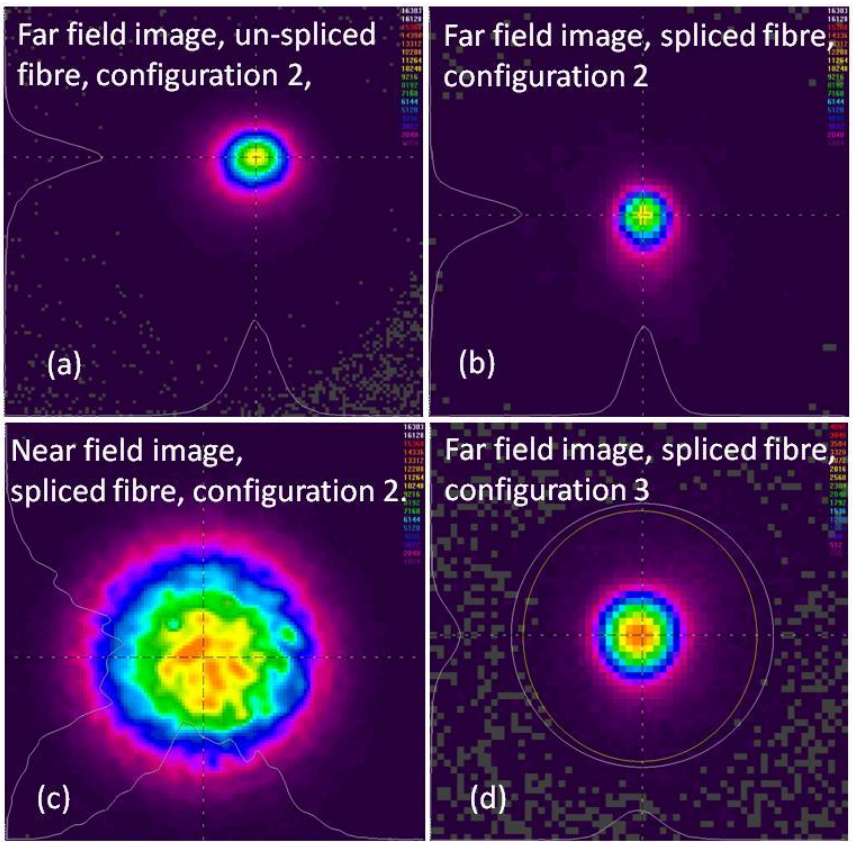

Figure 61: Beam profiles for various measurements (Ref) in the development of a high power cw TDFL.

An analysis of Table 6 reveals the potential loss mechanisms during the TDFL development process. Comparison between the slope efficiencies of measurements (2-3 in Table 6) indicates that laser efficiency improved with the addition of the passive fibres despite the decrease in beam quality. This can be attributed to effective cooling of the doped fibre tip. The variance for all the calculated slopes in Table 6 was ≤ 0.01. The beam quality drop (M^2) from 1.05 to 1.64 is most likely due to light scattering at the splice joints possible caused by core diffusion during splicing or, thermal mismatch

of the mode field diameters or mismatch of the fibre cores. The degradation in beam quality can be observed by the appearance of interference in the transverse beam profile (Figure 61(c)) [46], and an increase in cladding light at the outskirts of the beam profile (Figure 61(a-b)).The efficiency drop was most significant transitioning from configuration 2 to configuration 3 (2-3 in Table 6). The slight drop in beam quality after the addition of the optical feedback elements implies that the efficiency loss was in part due to optical feedback of the laser signal into the fibre cladding. However, due to the small decrease in beam quality factor, a more significant portion of the loss is most likely due to scattering, reflection and absorption losses introduced by the optical feedback elements. The slight decrease in beam quality from medium to full laser output power (3-4 in Table 6) is potentially due to thermal mismatch of the mode field diameter.

4.4.2 Output stability of the high power TDFL with an intracavity HR mirror

The output stability of the TDFL was monitored at various laser output powers using a 20 MHz Thorlabs InGaAs photodetector and a 1 GHz Tektronix oscilloscope. At low laser output powers a periodic chain of pulses (self-pulsing) was observed. Figure 62 shows two pulses measured at 2.9 and 4.8 W of laser output power respectively. Time divisions on the oscilloscope were set to 1 µs/div.

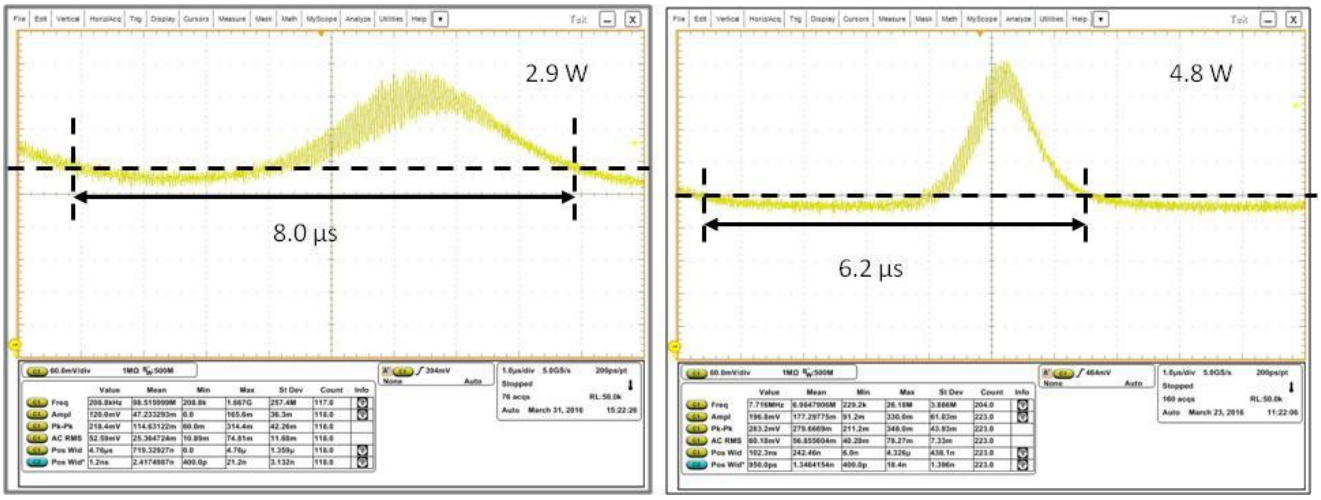

Figure 62: Screen shots recorded by the oscilloscope (@1 µs/div) for (left) 2.9 W and (right) 4.8 W of laser output power respectively.

The pulses themselves were also observed to be modulated. Figure 63(lower traces) illustrates two such pulses measured at laser output powers of 6.82 and 10.9 W. Figure 63 (upper traces) is an expanded view of the same pulses over a reduced time interval (4.5 down to 1 µs) clearly showing the modulation of the pulses. The frequency of the modulation was measured to be ~21 MHz.

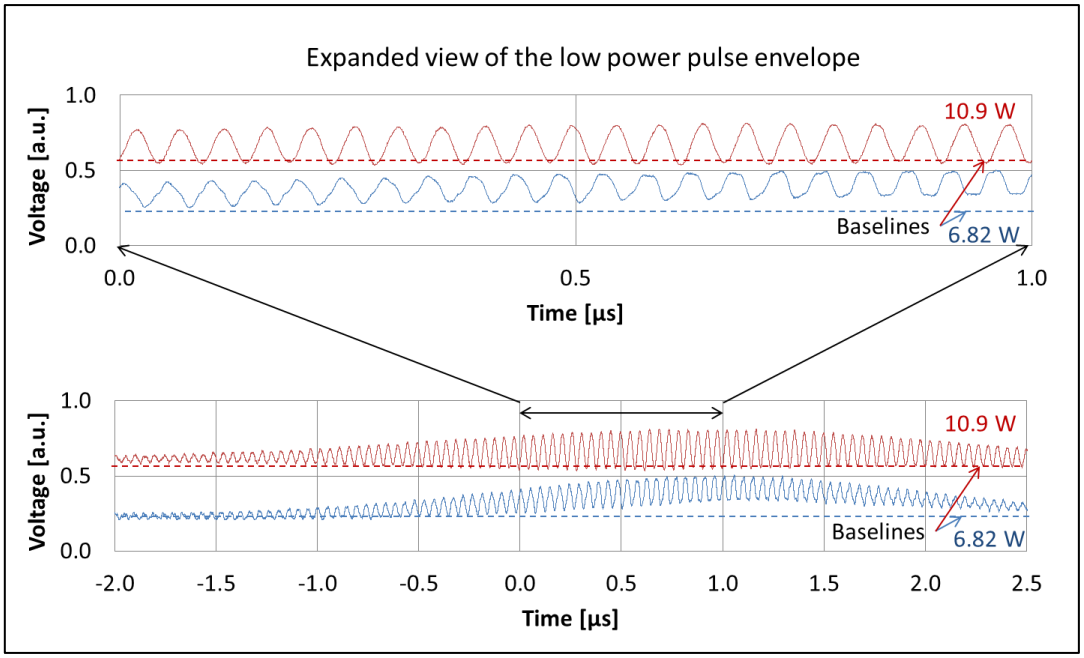

Figure 63: (lower traces) Single, periodic, pulse envelope as seen on the output of the 3.7 m TDFL at low output powers (6.8 W and 10.9 W). (upper traces) An expanded view of the low output power pulse envelope. The dotted lines represent the laser off (zero signal) baselines.

Figure 64 illustrates the temporal behaviour of the TDFL at high laser output powers (50 W). The laser output was observed to be cw with a periodic modulation. The intensity of the modulation for this measurement was measured to be ~12 % of the total laser intensity. The frequency of the modulation was measured again to be ~21 MHz.

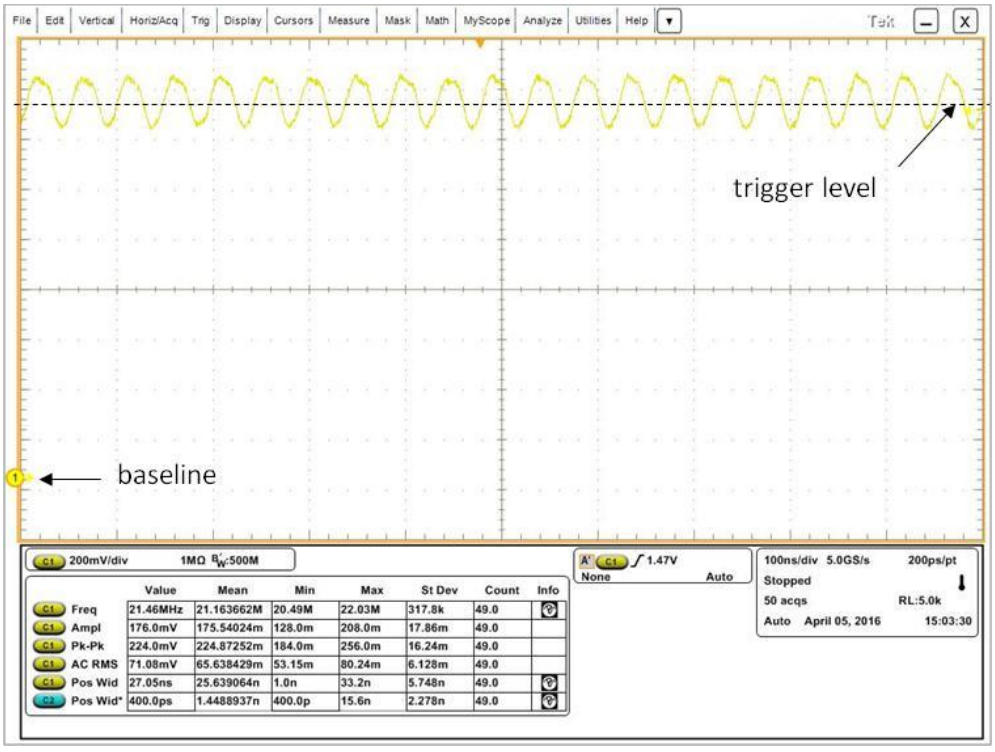

Figure 64: Screen shot recorded by the oscilloscope (@100 ns/div) for 50 W of laser output power.

Figure 65 illustrates the modulated TDFL output at various laser output powers.

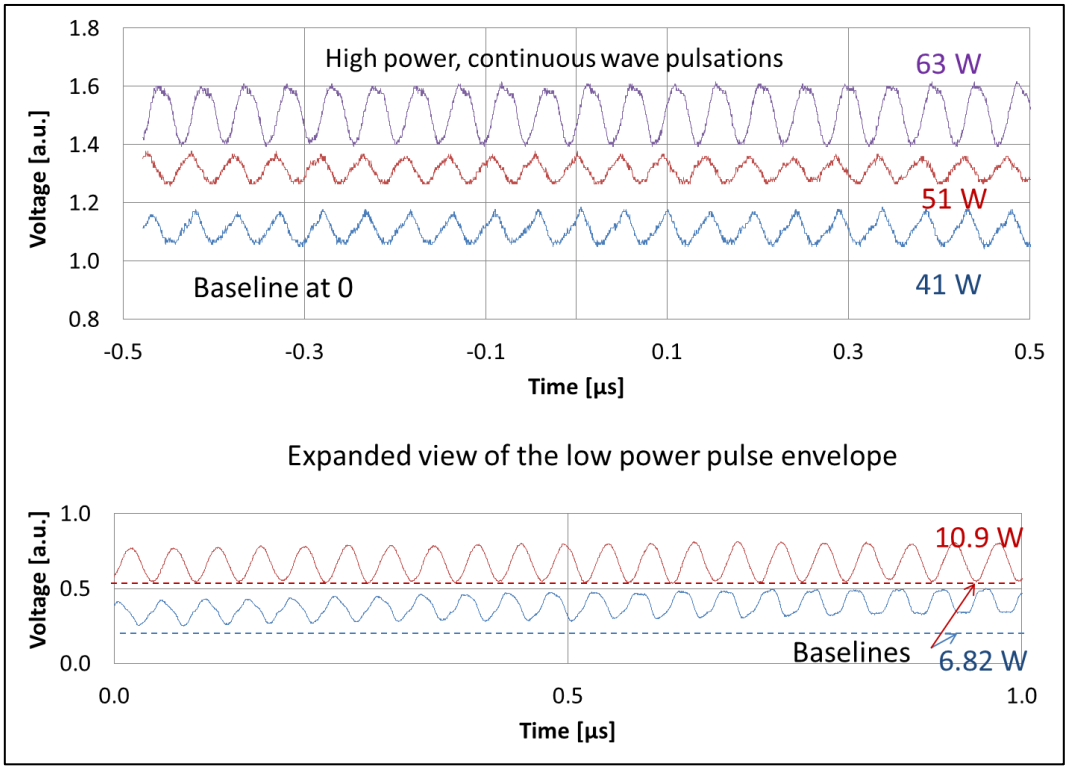

Figure 65 : (upper traces) Comparison of the periodic modulation of the TDFLs continuous wave output at high laser output powers and, (lower traces) the modulated pulse envelope at low laser output powers.

Figure 62 illustrates the self-pulsing of the TDFL at low laser output powers. The self-pulsing phenomenon in TDFLs was discussed in section 1.6. In this experiment, unlike the previous TDFL experiment (section 3.3.2), the periodicity of the self-pulsing was much better defined. This was most likely the case due to decreased reabsorption because of the 3.7 m TDFLs better thermal management scheme. The periodicity of the self-pulsing envelopes was measured to be in the 100's of kilohertz range (~200 kHz), again this correlates with similar results reported in literature (section 3.3.2).

More interestingly however was the frequency of the modulated self-pulsing envelopes at low laser output powers (Figure 63), and the modulated cw output (Figure 64) at high laser output powers. The frequency of this modulation was consistently measured to be approximately 21 MHz irrespective of the laser output power (Figure 65).

The measured modulation frequency corresponded very closely to the calculated round trip cavity frequency (Equation 9) of 21.37 MHz. The correspondence between the round trip cavity time and the amplitude modulation observed throughout this experiment has been identified several times in literature, e.g. Qamar and King who identified the phenomenon as self-mode-locking, [54,101]. Sub-200 fs pulses have been achieved by passively mode-locking (saturable absorber) Tm-doped fibre lasers [102] and a Neodymium-doped fibre laser [103].

Unfortunately, the Thorlabs photo detector available had a somewhat limiting bandwidth of 20 MHz. To determine whether the amplitude modulation is indeed self-mode-locking, an autocorrelator or

detector with a bandwidth twice the fundamental mode (Nyquist theorem) of the self-mode-locking (round trip frequency) would be required.

It is quite possible in the case of TDFLs, when considering intra fibre saturable absorption effects, that self-mode-locking can occur. This is certainly implied in literature [54]; however no explicit evidence of the phenomenon seems to have been reported.

4.4.3 Laser characterisation with intracavity 1939.8 nm and 2036.1 nm VBGs

In this section of the experiment, the intracavity HR mirror (Figure 58) was replaced in turn with two VBGs. The VBGs were designed for first order reflection at 1939.8 and 2036.1 nm respectively. The wavelength of the 2036.1 nm VBG was chosen to be within an atmospheric transmission window (Appendix B). The aim of this experiment was to assess the impact of wavelength selection on laser output power (efficiency), the spectral, and output laser stability.

Figure 66 illustrates the 2036.1 nm VBG placement between the 8° angle cleave and the HR mirror.

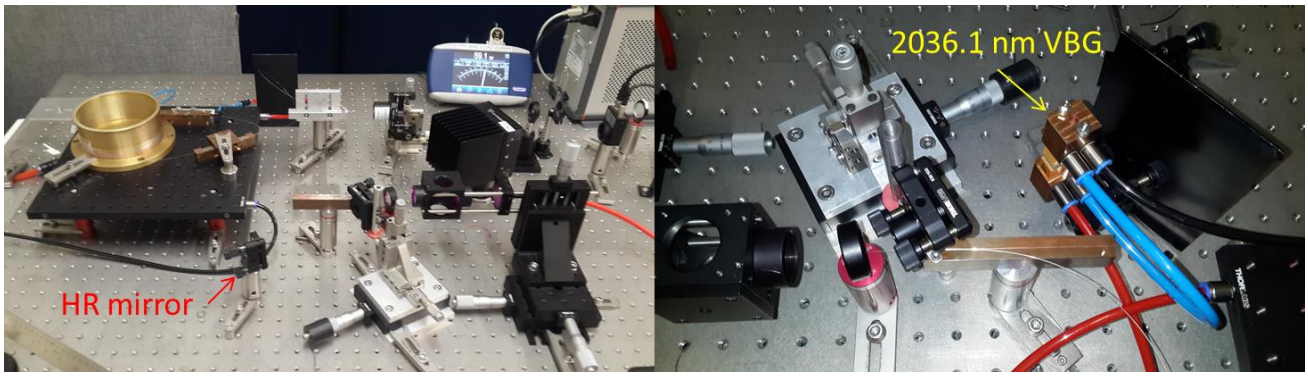

Figure 66: (left) Position of the HR mirror with respect to the passive fibre's angle cleaved input coupler. (right) After placement of the 2036.1 nm VBG between the HR mirror and input coupler.

The VBGs were set up for first order reflection and the output laser efficiencies (slope efficiencies) was measured for the two intracavity VBGs. A beam quality factor (M^2) measurement was performed with the intracavity 2036.1 nm VBG. The efficiency and measurement for the determination of the beam quality factor are shown in Figure 67 and Figure 68, respectively. The highest slope efficiency was recorded with the intracavity HR mirror as feedback element (~56 % slope efficiency). Introduction of the 2036.1 and 1939.8 nm VBGs reduced the slope efficiency by ~14 % (~48 % slope efficiency) and ~29 % (~40 % slope efficiency) respectively. The beam quality factor was also shown to reduce with the introduction of the 2036.1 nm VBG from an initial the M^2 value of ~1.75 (3 in Table 6) to ~2 (Figure 68).

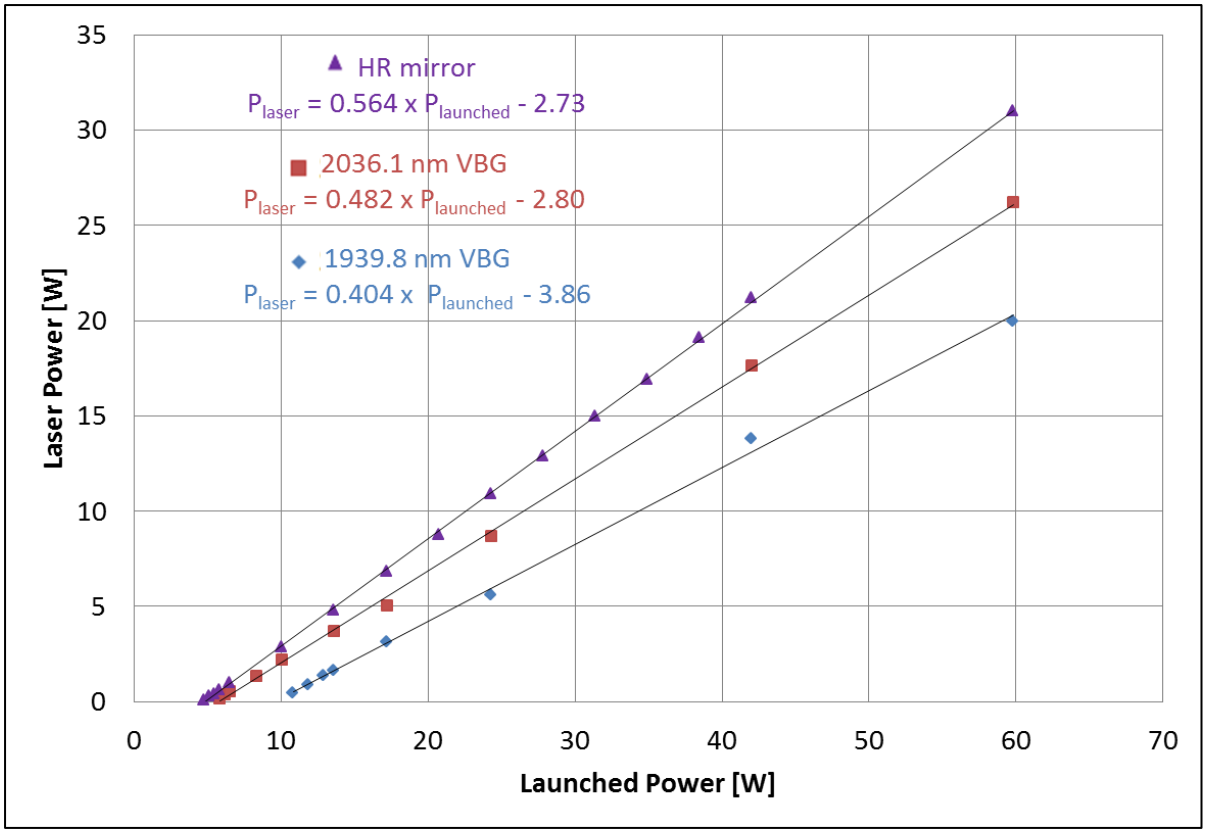

Figure 67: Slope efficiencies of the TDFL with various intracavity elements including a HR mirror, 1939.8 nm VBG and a 2036.1 nm VBG.

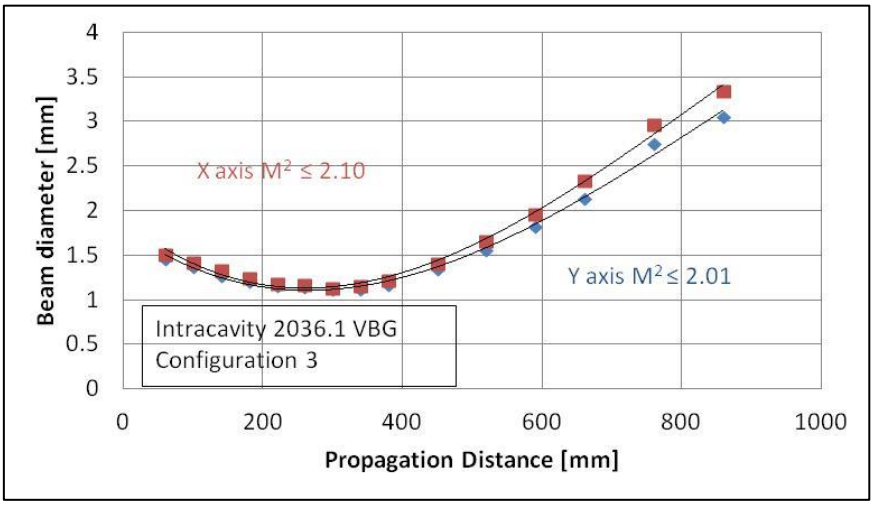

Figure 68: Measurements for the beam quality factor determination of the high power TDFL with an intracavity 2036.1 nm VBG.

Figure 69 is a beam profile of the intracavity ASE signal. Figure 69(b-c) are far field beam profiles of the laser output with the intracavity VBGs. Thermal blooming was observed with the intracavity 1939.8 nm VBG (Figure 69(b)). Cladding light was visible in the intracavity beam profile (Figure 69(a)), however, there seems to be more cladding light in the far field output shown in Figure 69(c) indicating light scattering off the VBG (2036.1 nm). The laser output beam with the intracavity 2036.1 nm VBG was observed to be very stable with no noticeable beam wander after 3m of free space propagation.

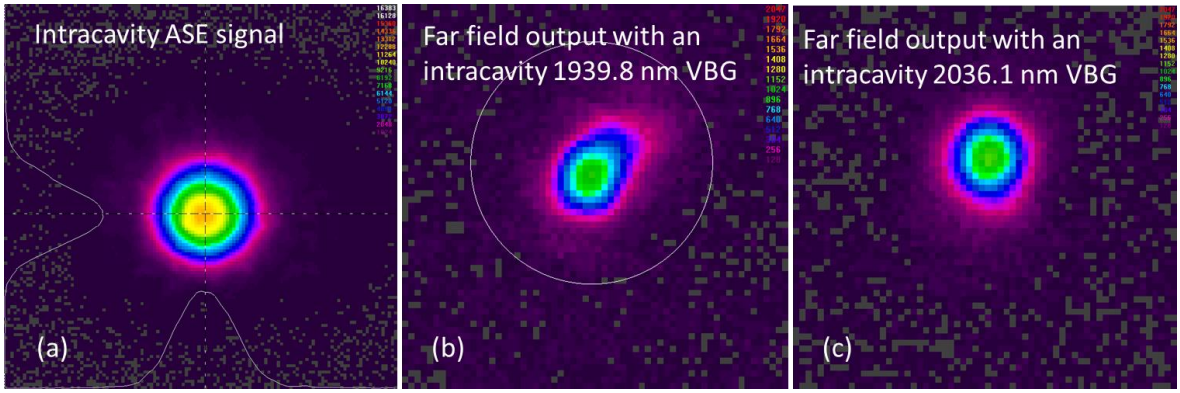

Figure 69: Beam profiles for the 3.7 m TDFL showing (a) the intracavity ASE signal and far field output signals for (b) a 1939.8 nm VBG and (c) a 2036.1 nm VBG.

The output spectra was measured for the free running laser, and the intracavity 2039.8, and 2036.1 nm VBGs. An Avantes NIR256-2.5TEC spectrometer was used for the measurements with the integration time set to 2 ms. The measured spectra are shown in Figure 70 where spectral narrowing (at the 6 nm spectral resolution) with the introduction of VBGs was observed. The central wavelengths of the spectral peaks corresponded with the first order reflection wavelengths of the respective VBGs. Real time analysis (at 2 ms integration time) of all three spectra showed no fluctuations in spectral intensity.

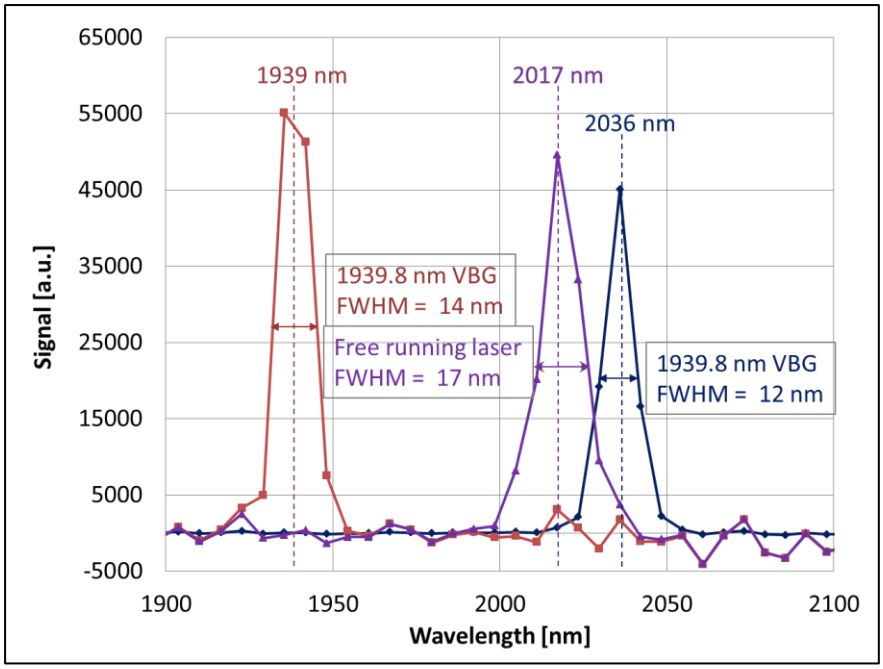

Figure 70: Spectroscopy of the 3.7 m TDFL with an intracavity HR mirror, 1939.8 nm VBG and 2036.1 nm VBG.

The output stability was monitored with both the intracavity 1939.8 nm and the 2036.1 nm VBGs. The setup was the same as before (section 4.3.2). Figure 27 shows screen captures recorded by the oscilloscope for some of the measured laser outputs traces. There was no significant (noticeable) change in the laser output stability where both self-pulsing and "self-mode-locking" was observed.

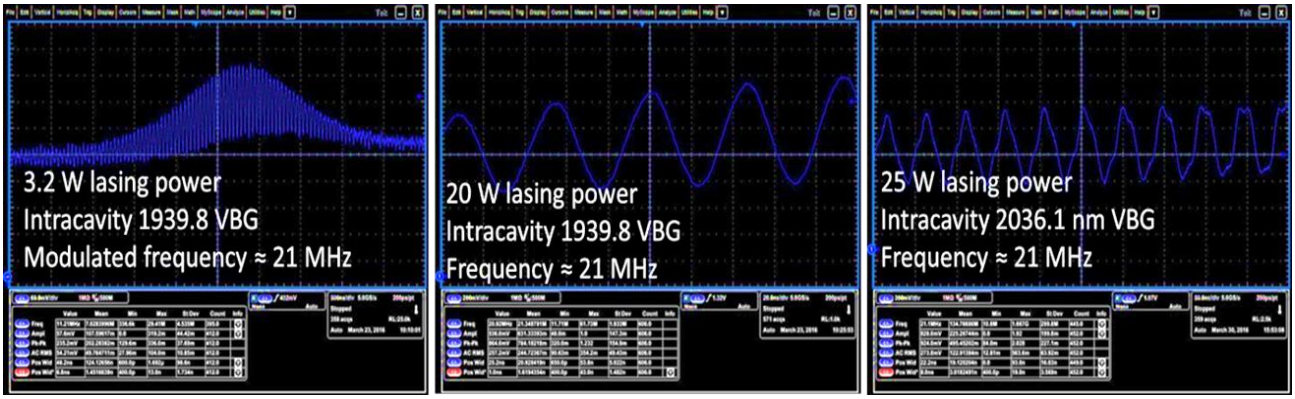

Figure 71: (left) Output stability the 3.7 m TDFL with an intracavity 1939.8 nm VBG at low power (@ 500 ns/division), (middle) high power (@ 20 ns/division)and (right) with an intracavity 2036.1 nm VBG at high power (@ 50 ns/division).

The loss in beam quality with the introduction of the VBGs was likely due to the backscatter seen in Figure 69. Scattering losses off the VBG will also have contributed to the slope efficiency losses. The distance from the angle cleave to the VBG was fairly long (~10 cm). This long free space propagation distance possibly exacerbated scattering losses. The loss is also not due to the VBGs clipping the beams. It has been shown that for beams clipped by VBG, maximum laser output power is reduced but not slope efficiency [46]. The 1939.8 nm VBG introduced the greatest loss; this was partly due to

its 91 % diffraction efficiency (Appendix B). Intracavity atmospheric absorption losses at the 1939.8 nm (Figure 69(c)) wavelength could also have decreased laser efficiency.

4.5 Conclusions

The high power, 3.7 m TDFL performed very well in terms of output power stability and beam quality (M^2 ≤ 1.86). The highest recorded power for the laser was 63 W at ~118 W of launched pump power. Due to the output lasing stability, it can be inferred that the thermal management scheme for the laser performed well and could potentially be scaled to significantly higher powers with the introduction of a more powerful FCLD source. For the length of fibre involved, the efficiency of the laser was comparable to similar high efficiency TDFLs found in literature [87], even though the slope efficiencies calculated in this experiment were with respect to the launched pump light and not absorbed pump light as often found in literature. It should be noted that the residual pump light measured for this experiment was approximately 8 % indicating that bidirectional pumping cannot be implemented on the TDF without breaching the 5 % back reflection threshold of the Dilas FCLD's. A slightly longer length of fibre would increase pump absorption and further improve the lasers slope efficiency. Implementation of a longer fibre (~5 m) and a bi-directional pumping scheme should increase the slope efficiency by ~8 %.

For future work it would be recommended that an aspheric doublet or triplet lens pair be used as an intracavity collimating lens. This will improve the lasers overall beam quality. It is also recommended that when introducing VBGs to first characterize the optical elements to ascertain their reflective and scattering properties. Beam quality can be improved with the introduction of a cladding mode stripper and better splice optimisation processes since the addition of splices was shown in the development of this laser to be the main contributing factor to loss of beam quality.

Chapter 5: Development of a Q-switched TDFL

5.1 Introduction

In this experiment a polarised, Q-switched TDFL was developed. The aim of the TDFL was to produce high intensity, ~2 µm wavelength pulses with pulse lengths in the 10's of nanosecond range. The pulsed 2 µm wavelength laser output could then directly pump a ZGP, OPO crystal for frequency down conversion [12,104]. Nonlinear frequency down conversion by the ZGP crystal is dependent on the pump lasers (TDFL) intensity. It is therefore imperative that the pulsed TDFL has a near diffraction limited beam quality.

5.2 Fibre preparation and pump setup

This section introduces the fibre parameters and preparation techniques relating to the polarisation maintaining TDFL. The pump design and pump light coupling efficiency is also discussed.

5.2.1 Fibre parameters

In this experiment, the Q-switched TDFL was developed using a Nufern, 25/400 LMA, polarisation maintaining (PM) Tm-doped fibre. Some of the relevant fibre parameters of the PM 25/400 TDF are listed in Table 7.

Table 7: Fibre parameters for the polarization maintaining thulium-doped fibre.

Fibre manufacturer	Nufern
Fibre type	Multimode, LMA, thulium doped, double clad
Operating wavelength	1.9 – 2.1 µm
Fibre length	4.0 m
Pump absorption	2.4 dB/m
Core diameter	25.0 ± 2.5 µm, NA = 0.090
Inner cladding diameter	400.0 ± 15.0 µm, NA ≈ 0.46
Low index polymer coating diameter	550.0 ± 20.0 µm
Pedestal	Diameter ~40 µm
Cladding geometry	Circular
Doping concentration	4 % wt
Birefringence	Nominal 2.5 x 10^{-4}
Configuration	Panda

Birefringence along the length of the fibre was induced by stress rods in a panda configuration. A cross section of the PM 25/400 TDF is illustrated in Figure 72. The figure is colour coded to match the fibre parameters listed in Table 7. The birefringence of the fibre allowed for a single polarisation

mode to be transmitted (maintained) either parallel (slow axis) or perpendicular (fast axis) to the stress rods along the length of the fibre.

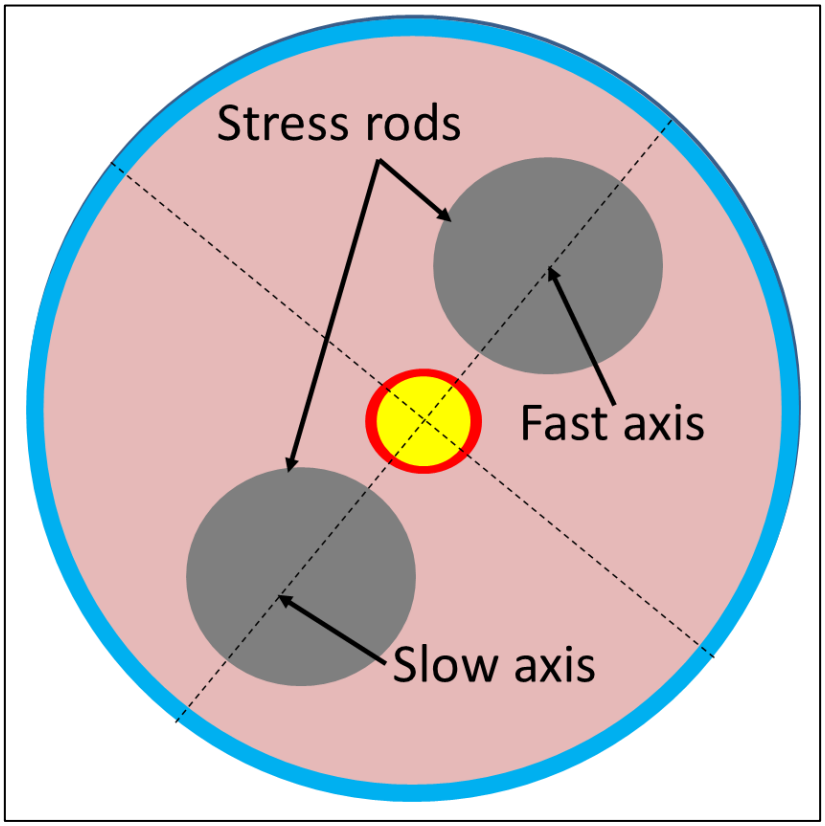

Figure 72: Colour coded cross section (Table 7) of the PM 25/400 TDF used in the development of the Q-switched TDFL.

5.2.2 Fibre preparation

Cleaving of the PM fibre is very different from that of TDF used in previous experiments. Applying the same tensions as used on the non-PM fibre induced severe hackle about the stress rods. The tension was therefore significantly reduced from 12 N to 10 N. Below 10 N there was not sufficient tension to cleave the fibre. Also at a tension of 10 N, there was intermittent chipping of the fibre by the cleaver blade. To mitigate this problem, the piezo induced blade vibrational frequency was increased from a set point of 10 to 100 (Appendix B). These adjustments allowed for acceptable cleaves to be performed, as illustrated in Figure 73.

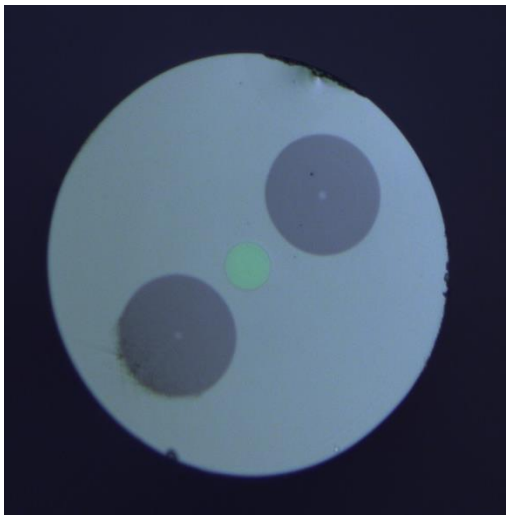

Figure 73: Fibre facet after the successful cleaving of the PM 25/400 TDF.

5.2.3 Pump design and coupling efficiency

The pump absorption per unit length of the PM 25/400 TDF (2.4 dB/m) was higher than that of the TDF's used in previous experiments (1.8 dB/m). The PM 25/400 TDF was also slightly longer (4 m vs. 3.7 m). The increased pump absorption and fibre length allowed for the implementation of a bi-directional pumping with reduced risk of damage to the FCLD's.

The first pump laser remained the same as in previous experiments. A second identical ~793 nm diode source was used as a pump source. Pump coupling optics for the second pump source consisted of two BK7 silicate substrate lenses coated for high transmittance at the 793 nm diode laser wavelength. Both lenses had focal lengths of 50 mm, however only one of the lenses was spherically corrected. This reduced the pump coupling efficiency of the second pump source. It was also found that the 45° dichroic mirror through which the second diode would need to pump through was not transmitting 793 nm pump light as efficiently as the specifications of the mirror suggested (> 99 %). To accurately account for such losses the coupling efficiency for the second laser diode was measured with this mirror in place. The respective coupling efficiencies can be seen in Figure 74.

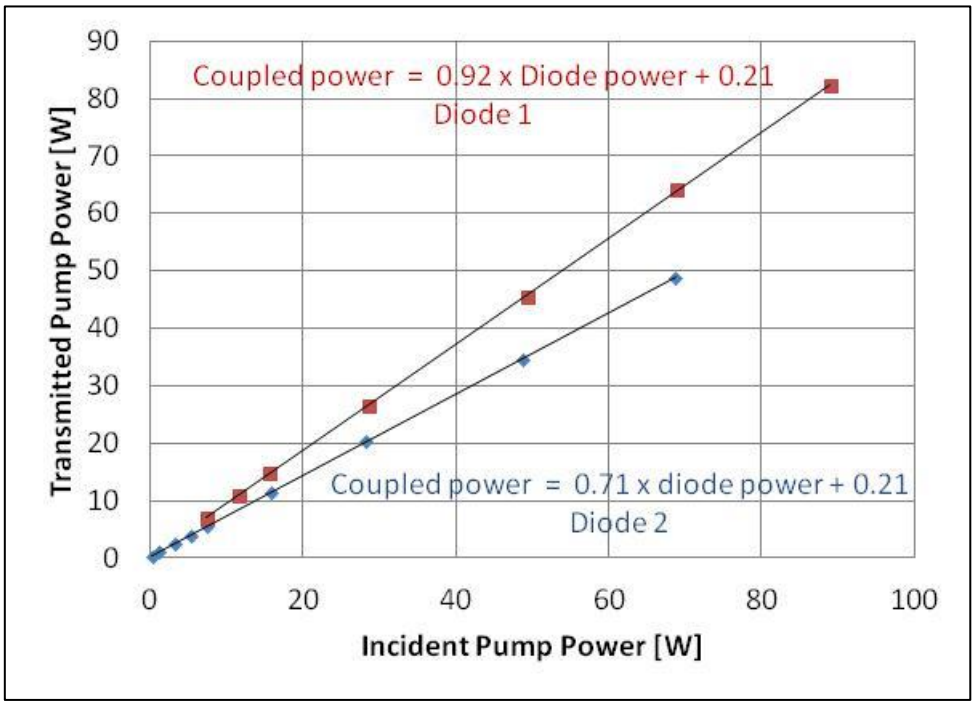

Figure 74: Respective coupling efficiencies for the two pump diodes used in the development of the Q-switched TDFL.

5.3 Laser design

This section covers the laser design considerations and laser setup and procedures.

5.3.1 Laser design considerations

In section 4.4.1 it was found that the addition of splices can potentially reduce the laser beam quality. It was also shown in this experiment (section 4.4.2) that without passive splices attached, no more than ~56 W of pump power could be safely coupled into the TDFL. It has been shown in literature that the optical damage threshold for silicate fibres is approximately 40 GW/cm^2 [105].

If we assume the Q-switched TDFL will produce pulse lengths of roughly 60 ns, at a repetition rate of 40 kHz, as was the case in similar q-switched TDFLs [12], the average power for such a laser would be approximately 35 W at the 10 kW peak power limit. Assuming a relatively poor slope efficiency of 30 %, this level of laser power could be achieved with around ~105 W of cw pump power from a FCLD. This estimate is too high for pumping directly into an unspliced TDFL (upper limit ~56 W), however, with bi-directional pumping both ends of the PM TDFL, this figure can be halved and still be within the safe pumping limit. Furthermore, as discussed in section 3.3.2, a bi-directional pumping scheme will improve temporal stability and increase pump to laser output efficiency. It was also assumed that mitigation of splices would be less detrimental to output beam quality. Based on these considerations, a bidirectional pumping scheme with no passive splices attached to the TDF was decided upon.

5.3.2 Setup and procedures

Like the high power cw TDFL, the q-switched laser was developed and characterised in stages in order to identify any laser performance losses introduced. Figure 75 is a schematic of the Q-switched TDFL. The Brewster plate AOM would ensure intracavity linear polarisation and the half wave plate (HWP) would align the linearly polarised light to the polarisation axis of the TDF. The higher pump absorption per unit length of the PM TDF (2.4 dB/m) also ensured that there was < 3 % residual pump light exiting the fibre. This was well within the 5 % tolerance of the FCLD's.

The PM TDFL was first set up for continuous mode operation. The "collimating" doublet lens pair (L3 in Figure 75) made up of a 25.4 mm and a 57 mm focal length lenses. The 25.4 mm and 57 mm focal length lenses had lens diameters of 12.5 mm and 25.4 mm respectively. The smaller diameter lens was placed in front of the larger diameter lens, that is, light exiting the fibre passed through the smaller lens first. Placing the smaller diameter lens first ensured that the smallest possible intracavity beam diameter passed through this optical element reducing spherical aberration. The larger lens was placed after the smaller lens where the beam diameter is slightly larger.

A Brewster angled, crystal quartz AOM manufactured by Gooch and Housego was used for the Q-switching (Specs are listed in Appendix B). The AOM driver was a Gooch and Housego RF driver with up to 100 W of RF output power with variable pulse rates up to 100 kHz (Appendix B). The diagnostics at the lasers output consisted of a half wave plate, a thin film polarising beam splitter and a power meter. The HWP was placed between the TDF and the thin film polariser. This allowed for accurate determination of the average polarised laser output power.

The cavity was first polarised with an intracavity polarising beam splitter (PBS) and the output powers and slope efficiencies determined. The PBS was then placed intracavity with the AOM. This was done to accurately determine the Brewster angle for the AOM simply by adjusting the AOM angle for maximum vertically polarised, cw laser output power. Once the Brewster angle was determined the PBS was removed from the cavity and the slope efficiency re-measured to account for any loss of power or beam polarisation.

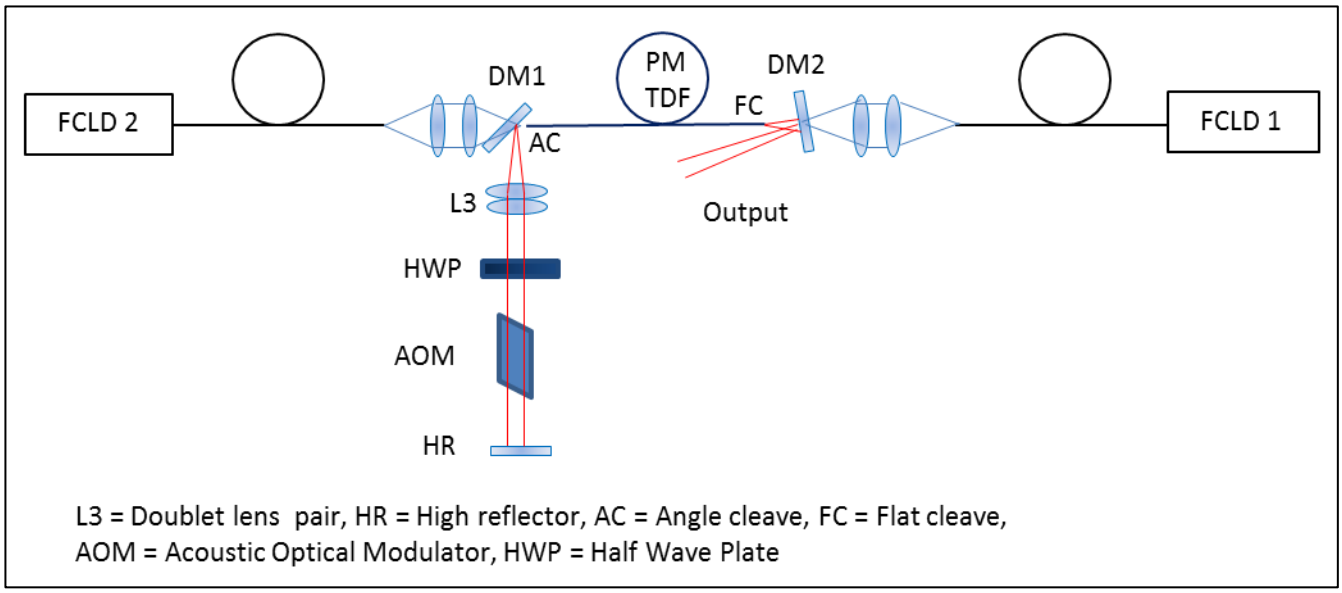

Figure 75: Schematic of the q-switched TDFL with a bi-directional pumping scheme.

Azimuthal alignment of the AOM about its centre axis was performed with a micro positioning plate attached by a rigid rod to the AOM. It was also noticed that air flows destabilised the Q-switching. To remedy the turbulence, a sealed dry air box was built around the entire laser maintaining the humidity at a steady 3 %. Figure 76 illustrates the various AOM translation stages and the dry air box. Figure 77 is a photograph of the laser setup. The HWP (yellow) is at the laser output end of the TDFL.

After careful azimuthal alignment at relatively high powers (10 W average laser power), the slope efficiencies at a variety of pulse repetition rates was measured, as illustrated in Figure 83. The intracavity polarisation was periodically checked with an intracavity thin film polariser, in line with the AOM to monitor for any polarisation changes.

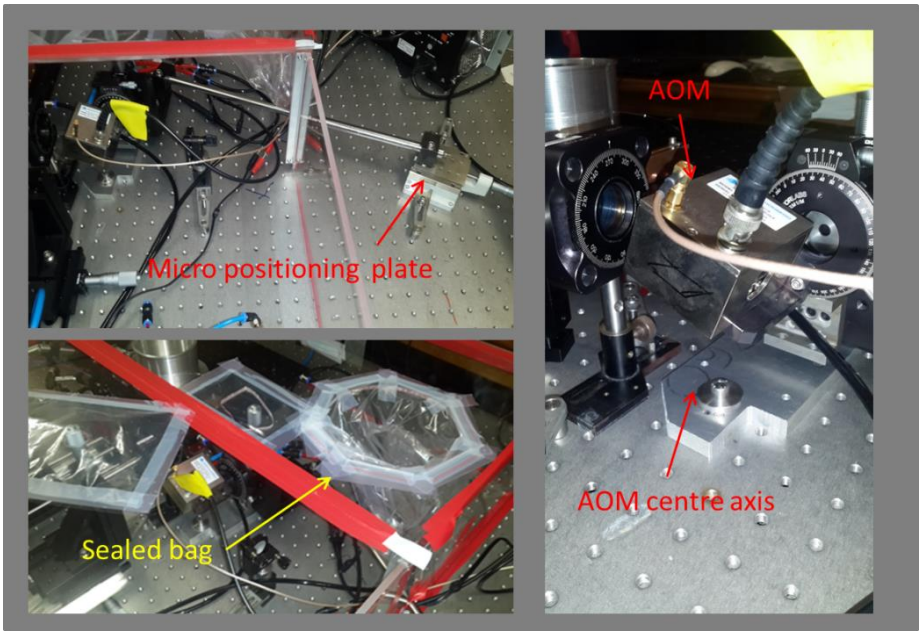

Figure 76: (top left, right) The AOM's adjustable azimuthal and elevation stages and (right) the dry air box with sealed bag for adjusting.

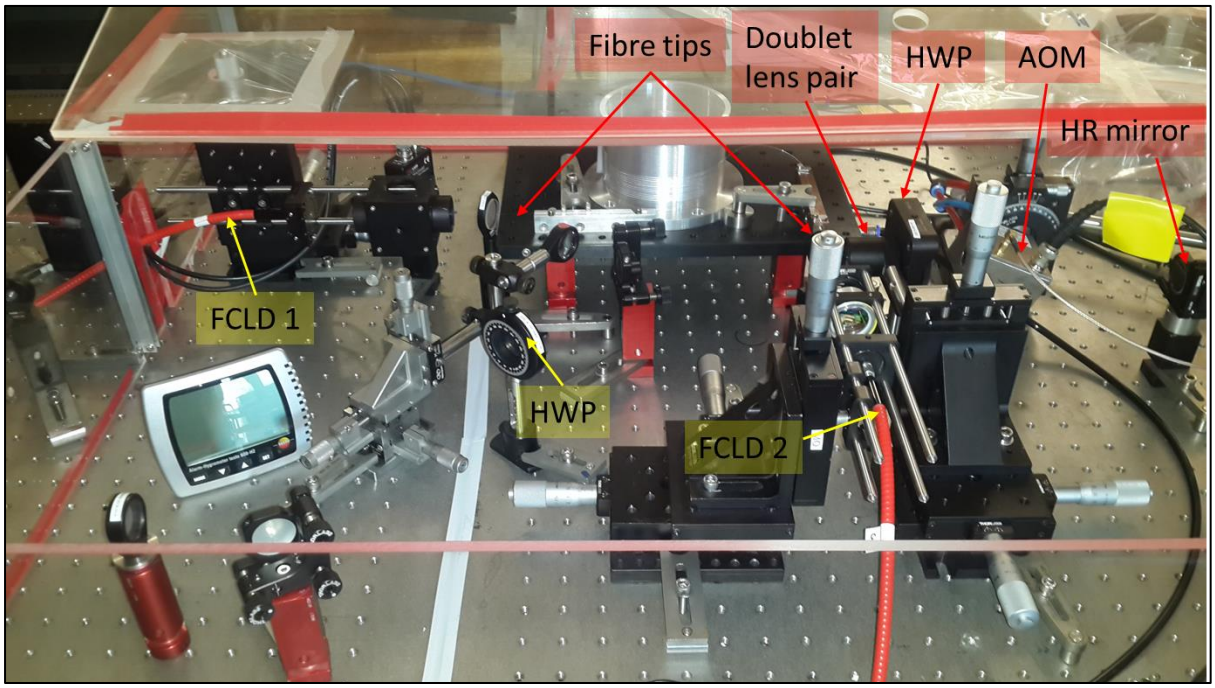

Figure 77: Photograph of the Q-switched TDFL highlighting some important laser components.

5.4 Experimental results and discussions

5.4.1 Continuous wave operation

Figure 78 illustrates the measured cw slope efficiencies leading up to and including the insertion of the Brewster angled AOM. Measurement of the unidirectional pumped, polarised cw laser slope efficiency was observed to drop (~4 %) after the insertion of the PBS. Replacement of the PBS with the Brewster angled AOM resulted in a further decrease of ~5 % (~9 % total). Implementation of a bidirectional pumping scheme was measured to increase the slope efficiency by ~4 %.

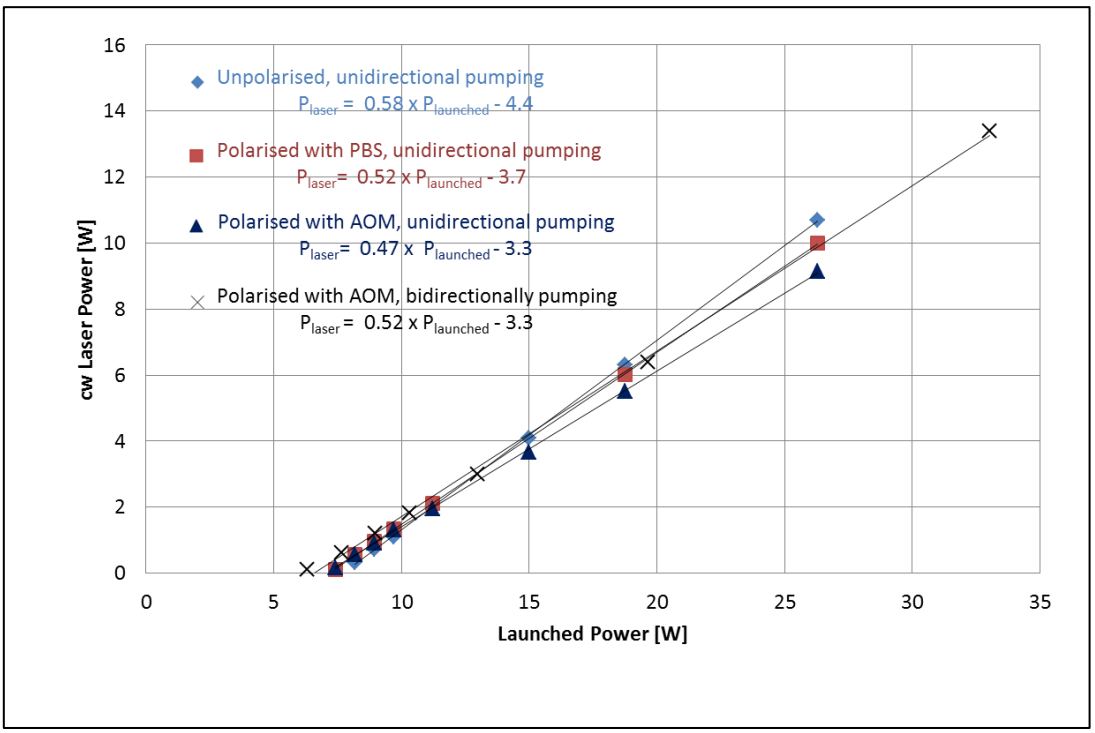

Figure 78: Slope efficiencies of the cw laser output (vertically polarised) for the PM TDF. Polarised laser output was first induced with a PBS (unidirectional pumping). Polarisation was later induced by a Brewster angled AOM which replaced the PBS. Efficiency measurements with the intracavity AOM were performed with unidirectional and bidirectional pumping schemes.

Slope efficiency measurements were performed for the total output laser powers for the intracavity PBS and AOM cases as illustrated in Figure 79.

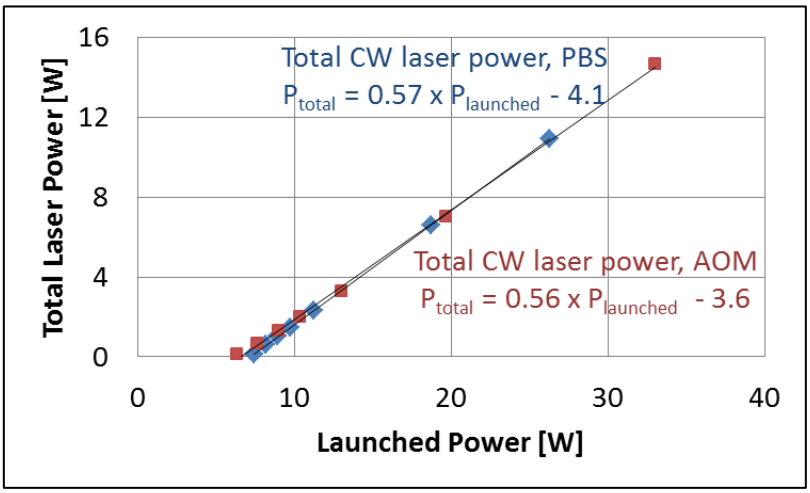

Figure 79: Comparison between the cw laser output slope efficiencies with an intracavity PBS and the total unpolarised laser output.

The HWP angle at the cw laser output was varied through 360°. Figure 80 illustrates the measured ration of polarised (vertically) to total laser output powers. The polarisation factor $(P_{max}-P_{min})/(P_{max}+P_{min})$ of this curve was ≥ 87 % which corresponds to a polarisation extinction ratio (PER) of 8.9 dB.

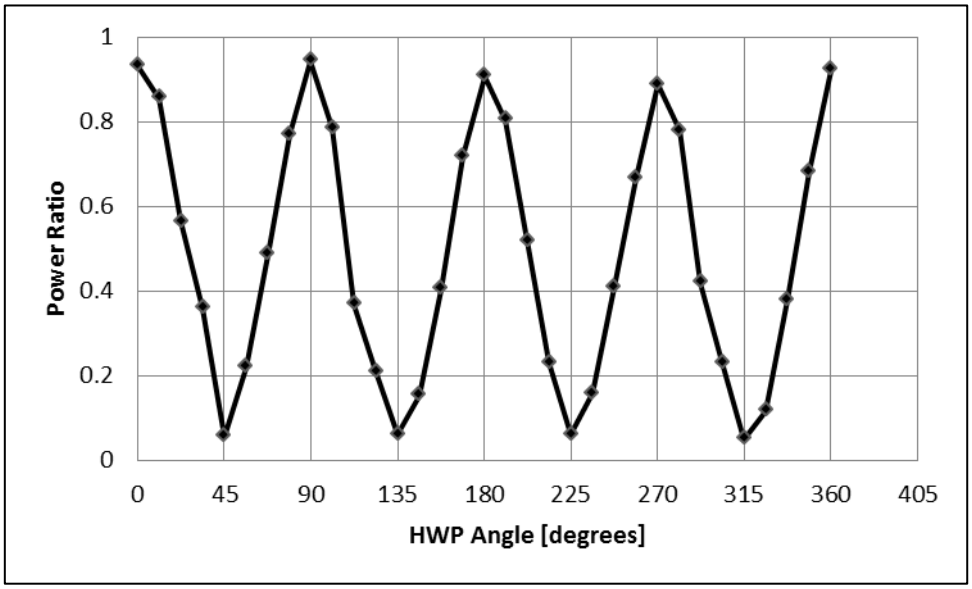

Figure 80: Ratio of vertically polarised to total laser output power on rotation of a HWP between the TDFL and a fixed thin film polariser. The AOM was the intracavity polarising element.

The polarised cw output stability was measured for both the unidirectional and bidirectional pumping scheme as illustrated in Figure 81. Both the upper and lower trace was recorded by the oscilloscope over a 20 µs time interval at 14 W of average laser output power. Self-pulsing was evident at lower pump powers and transitioned to a modulated quasi cw laser output at higher pump powers. For the bi-directional pumping scheme, the transition from self-pulsing to quasi cw

was observed at lower pump powers than for the unidirectional pumping scheme. This is clearly illustrated in Figure 81, where at 14 W of average laser output power the bidirectional pumping scheme has a stable quasi cw output, whereas self-pulsing is still evident in the unidirectional pump scheme at the same average laser output power level.

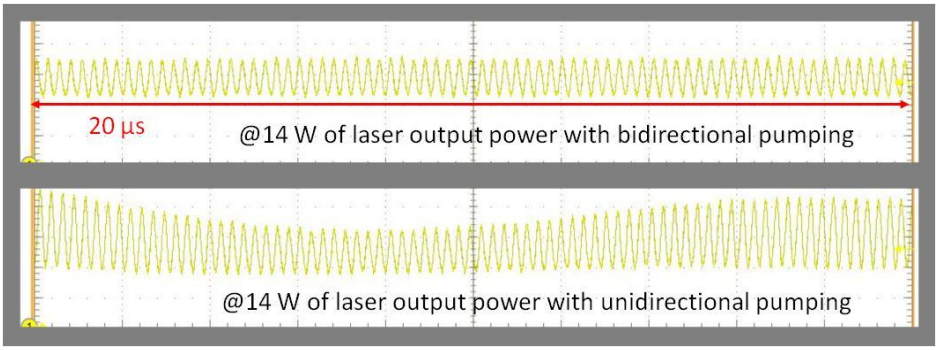

Figure 81: (upper trace) Output stability of the cw laser output with bidirectional pumping and, (lower trace) unidirectional pumping of the PM TDFL. The traces were recorded over a 20 µs interval (@ 2 µs/division) with 14 W of average laser output power.

The bidirectional laser output stability was recorded at several laser output powers as illustrated in Figure 82. Modulation of the cw output was measured to have a consistent frequency of ~3.8 MHz.

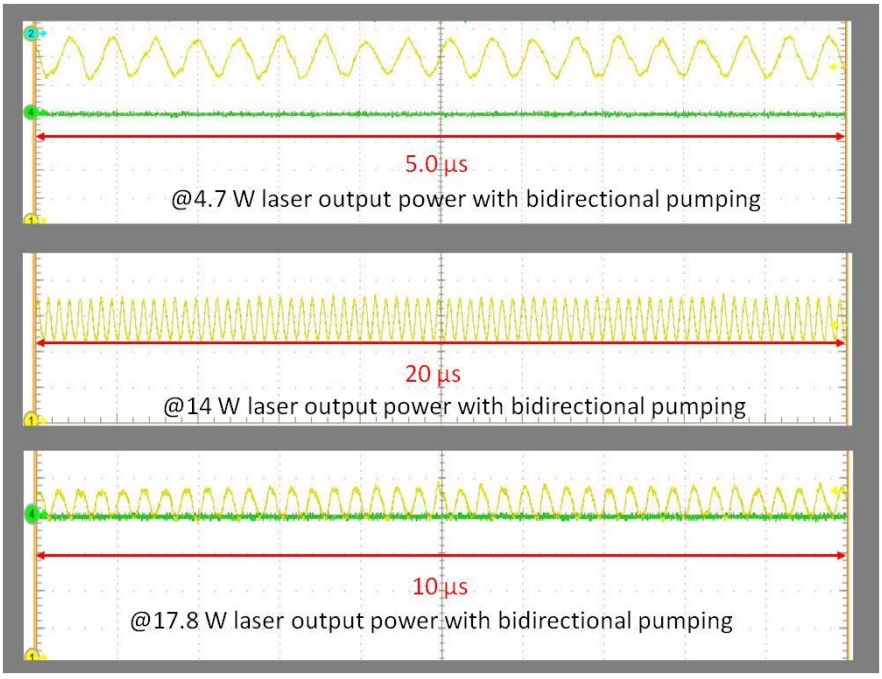

Figure 82: Screen shots recorded by the oscilloscope at laser output powers (upper trace) 4.7W (@ 500 ns/division), (middle trace) 14 W (@ 2 µs/division) and (lower trace) 17.8 W (@ 1 µs/division)of laser output power with a bidirectional pumping scheme. The frequency of the modulated cw output was measured to have a frequency of ~3.8 MHz for all three traces.

5.4.2 Discussion

Comparison of Figure 78 and Figure 79 reveals that the drop in slope efficiency after the implementation of the PBS and Brewster angled AOM is predominantly due to the presence of horizontally polarised light in the laser output. Figure 80 shows that the ratio of vertically polarised to horizontally laser output power with the Brewster angled AOM as polarising element was ≥ 87 %. Figure 79 also shows that the PBS was more effective as an intracavity polarising element. However, the PBS was not designed for high power laser operation and is therefore excluded from future setups.

Bidirectional pumping of the PM TDFL improved the temporal stability (Figure 82) and slope efficiency (Figure 78) of the laser output beam was also shown to improve. In section 4.4.3, the cw output of the high power TDFL was shown to be modulated at a frequency corresponding to the round trip time of the laser cavity. The cw output of the PM TDFL was again shown to be modulated, however the measured modulation frequency (~3.8 MHz) did not correspond to the calculated round trip time of the cavity (~27 MHz). For a mode-locked laser, the fundamental frequency (lowest) should correspond to the cavity round trip time. Therefore, self-mode-locking in this instance is unlikely and it is not known at this stage what could be the cause of the modulation.

5.4.3 Q-switched operation

A slope efficiency measurement was performed for the Q-switched laser at various pulse repetition frequencies (PRF's), as illustrated in Figure 83. At each respective PRF, as the pump power was increased the pulse lengths were observed to shorten and the average laser output power increased. Subsequently pulse peak powers increased with increasing pump power. This trend continued until a minimum pulse length, and correspondingly, a maximum pulse peak power was achieved. Up to this point the Q-switching was observed to be extremely stable with negligible timing jitter as is illustrated by the top trace in Figure 84. The green trace in Figure 84 represents the wave function generators switching voltage and the blue trace the actual RF signal supplied to the AOM. Further increasing the pump power resulted in the laser output becoming temporally unstable. The temporal destabilisation was first observed as a post pulse (top and middle trace Figure 84) and upon further increase of the pump power as chaotic self-pulsing and complete depolarising of the laser output beam. The onset of laser destabilisation occurred at lower pump powers for lower PRF's. At the various PRF's shown in Figure 83, the last measurement point (highest power) at each respective PRF indicates the highest measured power before destabilisation.

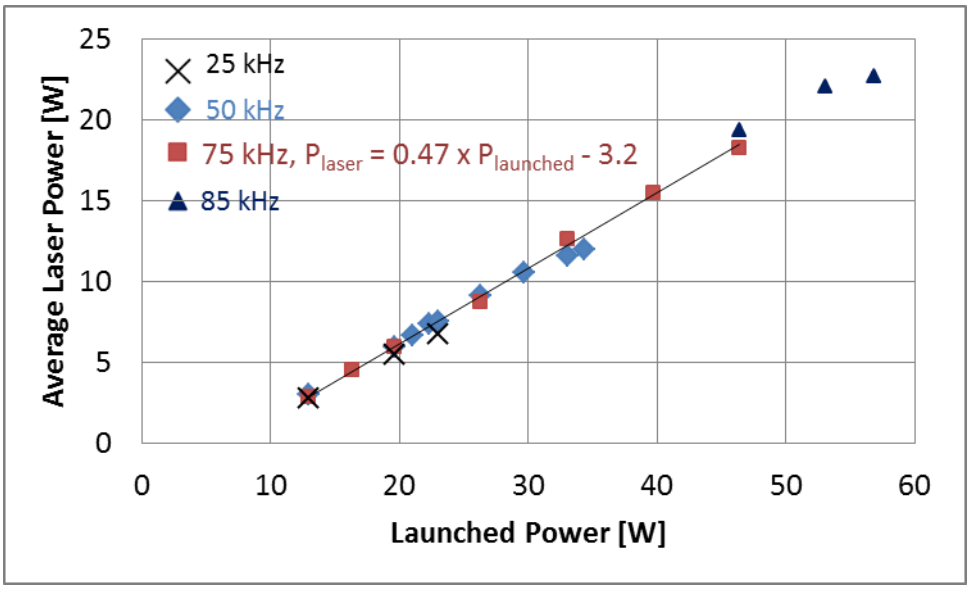

Figure 83: Slope efficiency of the q-switched PM TDFL at various pulse repetition rates.

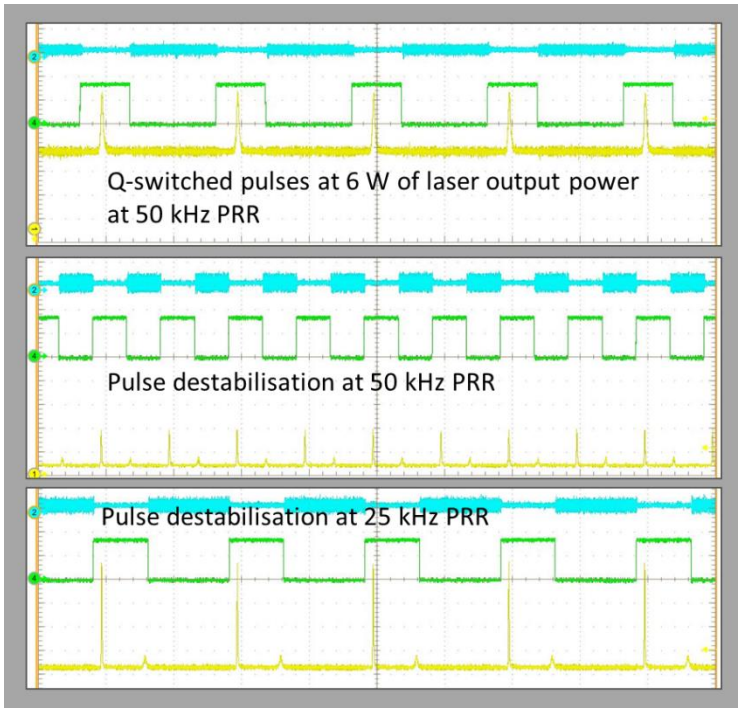

Figure 84: (top) Stable Q-switching of the TDFL before (50 µs/division) and (middle) observed post pulsing before temporal destabilisation of the laser output at 50 kHz PRF (100 µs/division). (bottom) Post pulsing before the onset of temporal instability at 25 kHz PRF (100 µs/division).

Figure 85 illustrates the maximum obtainable energies and average laser output powers at at various PRF's. The results for these measurements and the corresponding pulse lengths (minimum) at various PRF's are listed in Table 8.

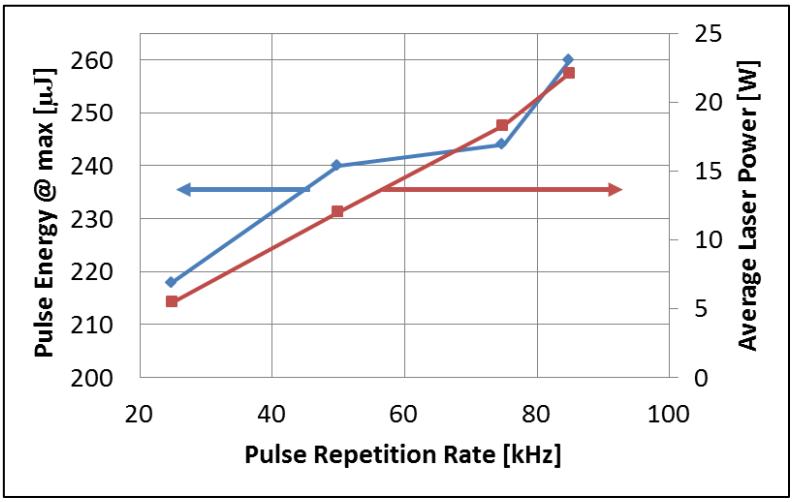

Figure 85: Plot of the pulse energy and average laser power as functions of pulse repetition frequency.

At the higher PRF's tested (75 and 85 kHz) at lower laser output powers, pulse skipping was observed. Figure 85 illustrates the laser output pulse energies and pulse lengths with increasing pump power and the PRF kept constant at 75 kHz. Below 30 W of launched pump power (Figure 86); the effective PRF due to pulse skipping was 37.5 kHz. The pulse skipping at lower pump powers and high PF's is a result of gain build up in the TDFL not exceeding the round trip cavity losses (section 1.2, section 2.6).

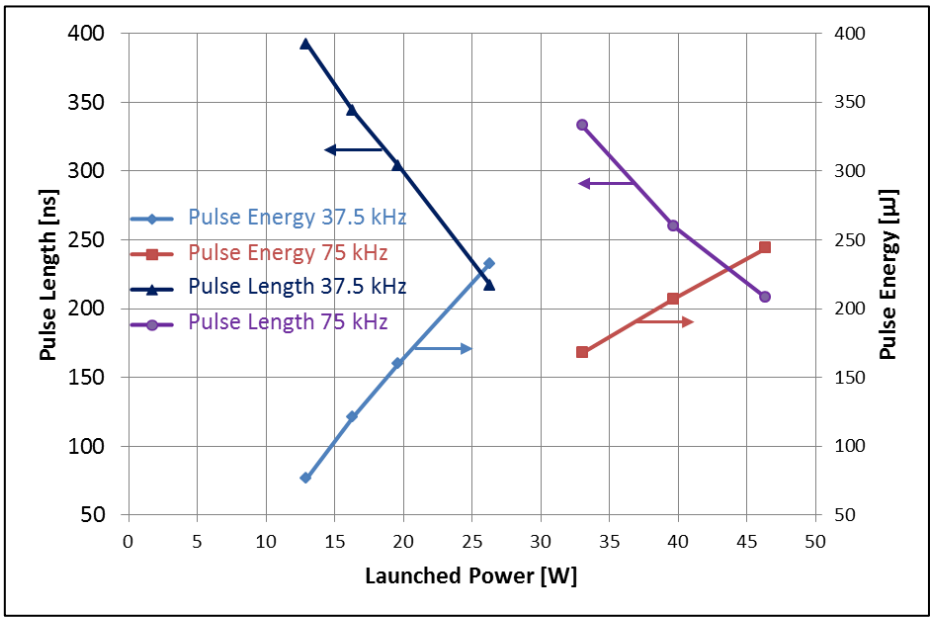

Figure 86: Pulse energy and pulse length curves at 37.5 KHz (pulse skipping at 75 kHz) and 75 kHz (every pulse).

Table 8: Maximum average powers, pulse energies and peak pulse powers at the minimum achievable pulse lengths for several pulse repetition frequencies.

PRR [kHz]	25	50	75	85
Minimum pulse length [ns]	207	211	208	208
Average power [W] @ minimum pulse length	5.47	12.0	18.3	22.1
Energy per pulse [µJ] @ minimum pulse length	218	240	244	260
Peak Power [kW] @ minimum pulse length	0.99	1.06	1.10	1.17

The outcomes of this Q-switched TDFL can be directly compared to a similar AOM Q-switched TDFL developed by Willis et al.. Major differences between the components used to develop the TDFL developed in this experiment and those used by Willis et al.[65] are listed in Table 9.

Table 9: Comparison between components used for the development of the Q-switched TDFL (this work) and that of Willis *et al.*

	Willis *et al.*	This work
Polarising element	PBS	Brewster plate AOM
Passive fibre attached	Y	N
AOM deflection efficiency	~70 %	~60 %
Pumping scheme	Unidirectional	Bidirectional

The comparative laser performance is listed in Table 10.

Table 10: Comparison between the performance of the Q-switched TDFL (author) and that of Willis *et al*.

	Willis *et al* [84] @ 100 kHz PRF	**This work @ 85 kHz PRF**
cw slope efficiency [%]	44	52
Q-switched slope efficiency [%]	40	47
Peak power [kW]	2.28 (calculated)	1.17
Average power [W]	28	22.1
Peak energy [µJ]	360	260
Pulse length [ns]	115	208

Comparison of the cw and Q-switched slope efficiencies (variance ≤ 0.06) show that this work is a significant improvement over the work reported by Willis *et al*. This was possibly due to the bidirectional pumping scheme (Figure 78). However, the Q-switched TDFL developed by Willis *et al.* performed better in terms of minimum pulse length, maximum pulse energy, peak power and average power. The performance of their laser, as was the case of this work, was limited by temporal destabilisation of the laser output pulses [46].

Figure 84 illustrates the observed post pulsing before the onset of pulse destabilisation (chaotic self-pulsing). The post pulse indicates that after the first pulse and within the off time of the AOM, there is sufficient gain build up in the TDFL for a second pulse. The opposite is true for pulse skipping. At high levels of pump light the gain build up and consequently ASE [64] in the TDFL is sufficient to cause laser action with the AOM in its on state. The result was a temporally chaotic, self-pulsing output. Since the AOM deflection efficiency for this Q-switched TDFL was ~10 % lower than that of Willis *et al*, less pump power was required for laser action to be induced in the AOM on state, thus reducing the maximum obtainable the pulse energies and peak powers.

The deflection efficiency of the AOM was also hindered by the presence of unpolarised light in the cavity. This is clearly shown by comparing Figure 78 with Figure 79, where the slope efficiencies with respect to total powers were the same despite different slope efficiencies with respect to the vertically polarised laser output. Figure 80 shows the ratio of the vertically to total output laser power. The measured polarisation factor of ≥87 % is lower than similar systems reported in literature which measured ~95 % [12].

5.4.4 Gain switching the Q-switched TDFL

As a consequence of the observed gain build up in the fibre whilst the AOM is “on” (section 5.3), gain switching of a single FCLD’s was implemented. The single channel wave function generator was replaced by a dual channel function pulse generator (DCFPG) (Hewlett Packard 8116A) which allowed for simultaneous or delayed pulse modulation to the AOM and FCLD power supply.

By modulating the FCLD, high power pump pulses at PRF’s corresponding to the AOM could be delivered to the TDFL. Figure 87 illustrates one such pump pulse. The blue trace in Figure 87 represents the switching voltage of the DCFPG (external analogue modulation) to the FCLD power supply. The yellow trace represents the temporal intensity profile (@ 100 µs/div) of the output

pump pulse. The curved edges of the pump pulse are due to the rise and fall times of the power supply. The green trace in Figure 87 represents the modulated switching voltage of the DCFPG to the AOM.

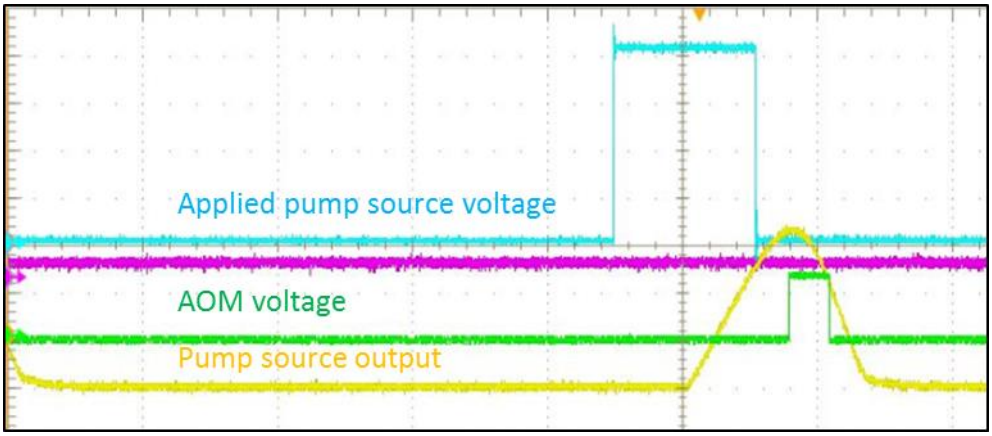

Figure 87: The DCFDG voltage (blue trace) and corresponding pump intensity (yellow trace) as recorded by the oscilloscope (@ 100 µs/div).

The rise and fall time of the FCLD limited the peak power and minimum pulse length of the pump pulses i.e. increasing the pulse power increased the pulse length. The slow modulation speed of the power supply is why the pump pulse trace in Figure 87 is not a square wave. To this end, the rise and fall times of the modulated pump pulse was compared between external analogue modulation (DCFPG) and internal digital modulation (FCLD power supply). A comparison of the two modulation modes is illustrated in Figure 88.

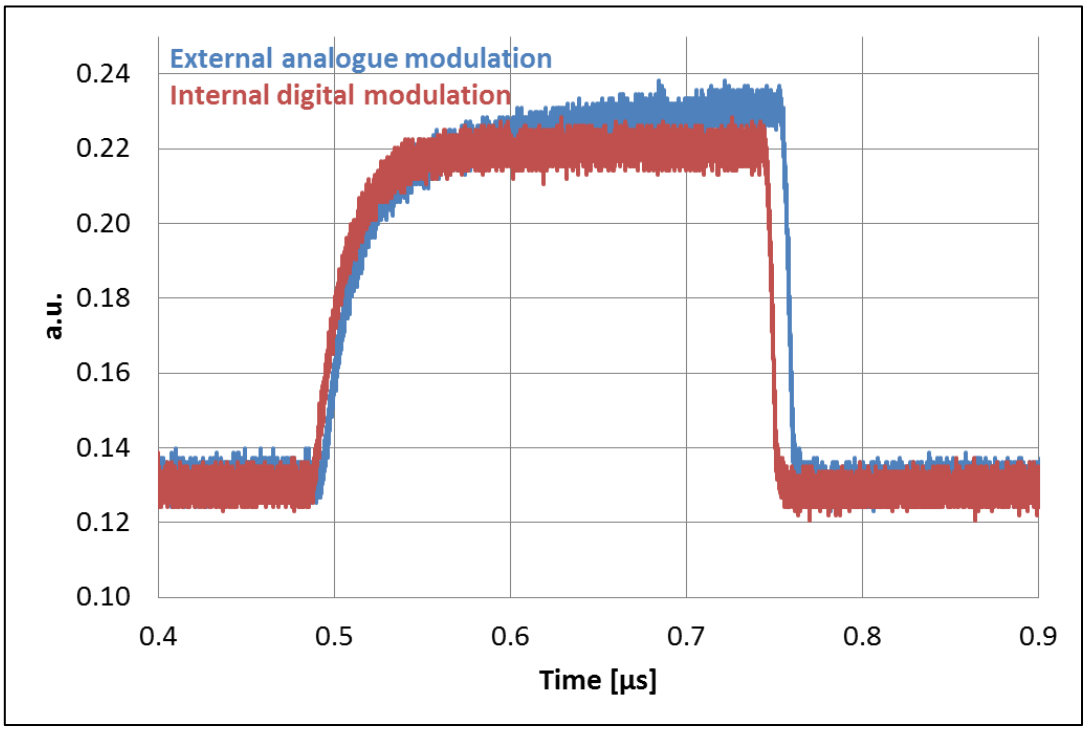

Figure 88: Comparison of the rise and fall times between external analogue and internal digital modulation of the FCLD.

There was no noticeable difference between the two modulation modes so external analogue modulation was decided upon for ease of synchronising the AOM and power supply modulation times.

The gain switch FCLD was coupled into the TDFL. Figure 89 illustrates the gain switched laser output pulses with no Q-switching. With no active Q-switching of the pulse lengths were ~870 ns. The blue trace indicates the DCFPG to power supply modulation voltage and, the purple trace the DCFPG modulation voltage to the AOM.

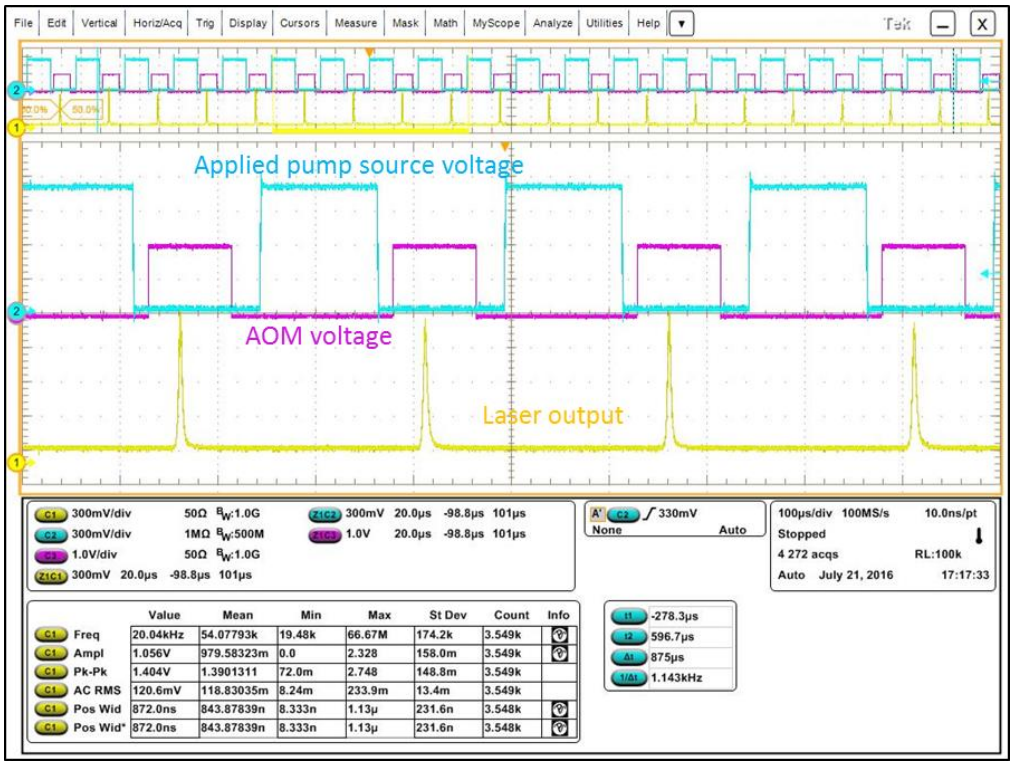

Figure 89: Screen shot recorded by the oscilloscope (@ 100 µs/div) illustrating the pulsed TDFL output with gain switching of the FCLD and no Q-switching.

Figure 90 illustrates an output laser pulse resulting from the Q-switched laser with a gain switched pump diode. The yellow trace represents the Q-switched pulses, the blue and green traces represent the DCFPG modulation voltages to the power supply and AOM respectively. The purple trace in this instance is irrelevant.

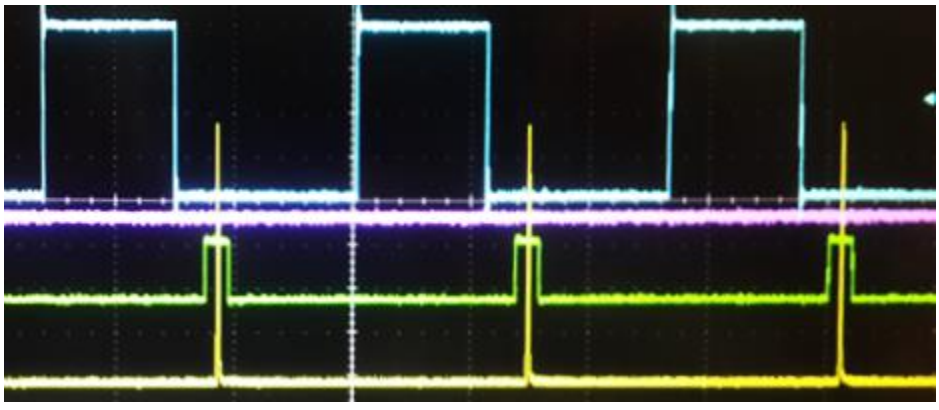

Figure 90: Photograph of the oscilloscope screen (@ 100 µs/div) showing the laser output pulses (yellow trace) for the Q-switched TDFL with a gain switched pump.

Previously the Q-switched pulse lengths were restricted to ~208 ns (Table 8). By limiting the gain build up time the pulse length was successfully reduced to ~164 ns (~21 % decrease) at a PRF of

19 kHz. Laser output pulse energy and peak pulse powers were ~238 µJ and ~1.35 kW respectively. The average output laser power for this measurement was ~4.5 W.

Gain switching of the Q-switched TDFL, in this instance, proved to be successful as a means of increasing peak powers and pulse energies whilst reducing pulse lengths at the respective PRF (19 kHz). The rise and fall time of the power supply limited the peak power of the pump pulses for scaling to higher average laser output powers at higher PRF's.

5.4.5 Beam quality of the Q-switched PM TDFL

Figure 91 illustrates the far field beam profile of the Q-switched TDFL at ~21 W of average laser output power at 85 kHz PRF. Although an M^2 measurement was not performed for the Q-switched TDFL, the output beam is free of cladding light and symmetric. The beam quality factor, based on the measurements performed on the unspliced cw laser (section 4.4) is assumed to be ≤ 1.2.

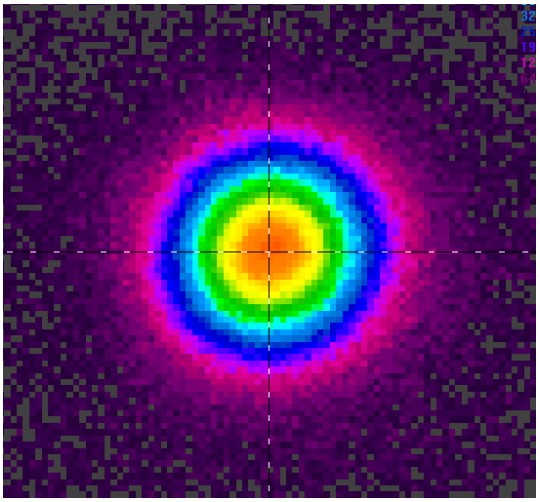

Figure 91: Beam profile of the Q-switched TDFL.

5.5 Conclusions

In this experiment, stable Q-switching of the PM 25/400 TDF was demonstrated. With continuous pumping at a PRF of 85 kHz, the Q-switched TDFL produced 260 µJ pulses. The corresponding pulse length and peak power was 208 ns and 1.17 kW respectively Comparative slope efficiency measurements of the TDFL were measured to be higher (52 % vs. 44 %) than similar lasers reported in literature [64,65]. Scaling to shorter pulse lengths and higher peak powers was limited by temporal destabilisation of the laser output beam. The destabilisation was caused by ASE build up in the TDF inducing laser action with the AOM switched on. Comparison with literature seems to indicate that the poor deflection efficiency and polarisation extinction ratio of the AOM was the likely cause. It was also shown in the experiment that gain switching of the FCLD's reduces the ASE build up time and therefore the threshold at which the laser destabilises. It can therefore be concluded that to reduce the pulse lengths of the Q-switched PM 25/400 TDF, an AOM with a higher

deflection efficiency or EOM be implemented. Furthermore it is recommended that a PBS capable of handling high power be used as the intracavity polarising element. To reduce pulse lengths by gain switching the FCLD, a power supply with rise and fall times comparable to the desired pulse length is recommended. Pulse lengths can also be reduced by decreasing the cavity length. This can be done by using a TDF with a higher absorption per unit length. However power scaling limitations will need to be considered.

Chapter 6: Conclusions and future work

This chapter serves to highlight important results relating to experiments performed in this dissertation. Each section of this chapter focuses on a specific experiment. In each section the following is addressed; important experimental outcomes, a brief comparison with results found in literature, limitations, and future work and recommendations.

6.1 Chapter 3 (Design, cavity and temperature considerations for TDFLs)

It was highlighted in this chapter that reabsorption effects in TDFLs affect the temporal stability and efficiency of the output laser. It was also shown that insufficient cooling of the TDFL exacerbates reabsorption effects. To minimise reabsorption the following conclusions were drawn;

- For longer TDFLs, a low mirror reflectivity product is desirable.
- Introduce where possible, a bi-directional or retro reflected pumping scheme.
- Cool the TDFL.

It was shown in this experiment and from literature sources that a low FCMRP (laser signal) reduces reabsorption effects. This was shown by spectral broadening of the laser output with increased FCMRP. It was also inferred by way of discussion that self-pulsing and temporal instability in TDFLs is closely related to reabsorption affects, particularly in unpumped regions of the TDF. To alleviate this issue it is suggested that a bidirectional or retro reflected pump scheme be implemented where possible. Bidirectional and to a lesser extent, retro reflected pump schemes will improve the TDFLs temporal stability and, pump to output laser conversion efficiency. Also, with retro reflected pump schemes, shorter doped fibres with higher mirror reflectivity products can be implemented potentially reducing the development cost. For future TDFL development it is therefore recommended that comprehensive models capable of calculating the optimal fibre length for specific fibre geometries and pumping schemes be developed. The outcomes of this model could then be weighed up against the desired usable output power and cost implications.

6.2 Chapter 4 (Development of a high power TDFL)

The high power cw TDFL slope efficiency of ~56 % compares well with similar TDFLs from literature. One such laser reports a slope efficiency of ~63 % with respect to the launched pump light (reference MCComb). The TDF's from both experiments were Nufern LMA 25/400 fibres; however the fibre used in this experiment was 3.7 m as opposed to 5 m. The increased fibre length improves pump absorption and allows for bidirectional pumping. For future high power TDFL development it is recommended that a longer length of TDF be implemented (≥ 5 m). Implementation of a longer fibre will improve the slope efficiency up to ~5 % (section 4.4.6).due to increased pump absorption and, ~ 4 % with a bidirectional pumping scheme (section 5.3.1). For the current laser scheme, retro

reflection of the pump light can be implemented. The MOPA developed by Goodno (section 2.8) was a bidirectionally pumped 3.1 m, LMA 25/400 TDF. The reported slope efficiency for this TDFL was 54 %.

The beam quality dropped after the implementation of splices. It is therefore recommended that splice optimisation processes be improved. Cladding mode strippers should also be investigated as a means of improving overall beam quality. The 3.7 m TDFL developed in this chapter will serve as a good platform for such an experiment because of its ~ 8 % residual pumps light and beam quality factor ($M^2 \leq 1.86$).

The stability of the average laser output power was excellent at all power levels. At low powers, the self-pulsing was periodic and at high powers the "self-mode-locked" output was very stable. The "self-mode-locking" observed in chapter 4 and 5 however, was unresolved. Apart from the correlation of the modulated frequency with the cavity round trip time (section 4.4.4), little can be said about the supposed pulse lengths and pulse shapes. A comprehensive study on a similar phenomenon in Neodymium fibre lasers has been reported [103]. Perhaps reports of this nature have been studied in the context of TDFLs unbeknown to the author. However, to the best of the authors knowledge such a study has not yet been performed and little is understood regarding the exact dynamical behaviour of the phenomenon in TDFLs. It is therefore recommended that the laser's temporal output be analysed with an autocorrelator.

Wavelength selection in this experiment proved to be lossier than expected. The decrease in slope efficiency indicates that cavity losses beyond those specified (Appendix B) were introduced into the laser cavity.by the VBGs. It is therefore recommended that VBGs be tested for scattering, reflectivity, and diffraction losses before implementation into laser cavities.

6.3 Chapter 5 (Development of a Q-switched TDFL)

A Q-switched TDFL was developed in chapter 5. The shortest reported pulse length for a Q-switched PM 25/400 TDFL is 115 ns. The minimum pulse lengths reported in this experiment were 207 ns. As discussed in section 5.4.3, the pulse length can be reduced with the implementation of a PBS and an AOM with higher diffraction efficiency. Gain switching of the Q-switched TDFL pump diodes was shown to reduce pulse lengths (section 5.4.4) from ~207 ns to ~164 ns.

It is therefore recommended that a PBS and AOM be implemented into the current Q-switched laser. Furthermore, it is recommended that if possible, a power supply with a faster rise and fall time (order of nanoseconds) gain switch the pump diodes. By gain switching the Q-switched TDFL it seems reasonable to expect that pulse lengths shorter than 115 ns are achievable. Also, because of the high gain volume of the LMA 25/400 TDF compared to shorter fibres [12], higher pulse peak powers and energies are obtainable.

References

[1] N. M. Fried, “High-Power Laser Vaporization of the Canine Prostate Using a 110 W Thulium Fiber Laser at 1.91 um,” *Lasers Surg. Med.*, vol. 36, no. 1, p. 36:52–56, Jan. 2005.

[2] N. M. Fried and K. E. Murray, “High-Power Thulium Fiber Laser Ablation of Urinary Tissues at 1.94 um,” *J. Endourol.*, vol. 19, no. 1, p. 19(1): 25-31., Feb. 2005.

[3] J. Yu, U. N. Singh, J. C. Barnes, N. P. Barnes, and M. Petros, “A high energy 2-µm laser for multiple lidar applications,” in *Proceedings of SPIE - The International Society for Optical Engineering*, 2001, vol. 4153, pp. 70–77.

[4] Phil Saunders, “Fiber Lasers,” *Optics and Photonics*, pp. 34–41, Aug-2014.

[5] T. S. McComb, V. Sudesh, L. Shah, R. A. Sims, and M. C. Richardson, “Widely tunable (>100 nm) continuous-wave narrow-linewidth high-power thulium fiber laser,” 2009, p. 71931I–71931I–8.

[6] G. Renz and W. Bohn, “Two-micron thulium-pumped-holmium laser source for DIRCM applications,” in *Proceedings of SPIE - The International Society for Optical Engineering*, 2007, vol. 6552.

[7] P. F. Moulton *et al.*, “Tm-Doped Fiber Lasers: Fundamentals and Power Scaling,” *IEEE J. Sel. Top. Quantum Electron.*, vol. 15, no. 1, pp. 85–92, Jan. 2009.

[8] T. Ehrenreich, R. Leveille, I. Majid, and K. Tankala, “1-kW, all-glass Tm:fiber laser,” in *Fiber Lasers VII: Technology, Systems and Applications*, Photonics West 2010, 2010.

[9] E. Lippert, S. Nicolas, G. Arisholm, K. Stenersen, A. S. Villanger, and G. Rustad, “High-power fiber-laser-pumped mid-infrared laser sources,” *Proc. SPIE - Int. Soc. Opt. Eng.*, vol. 6397, 2006.

[10] W. Koen, C. Jacobs, L. Wu, and H. J. Strauss, “60W Ho:YLF oscillator-amplifier system,” 2015, vol. 9342, p. 93421Y–93421Y–6.

[11] W. Koen, C. Bollig, H. Strauss, M. Schellhorn, C. Jacobs, and M. J. D. Esser, “Compact fibre-laser-pumped Ho:YLF oscillator–amplifier system,” *Appl. Phys. B*, vol. 99, no. 1–2, pp. 101–106, Apr. 2010.

[12] C. Kieleck, A. Berrou, B. Donnellan, B. Cadier, T. Robin, and M. Eichhorn, “6.5W mid-infrared ZnGeP2 parametric oscillator directly pumped by a Q-switched Tm3+-doped single oscillator fiber laser,” 2015, p. 93470O.

[13] H. J. Strauss *et al.*, “330 mJ, 2 µm, Single Frequency, Ho:YLF Slab Amplifier,” in *Advanced Solid-State Photonics*, 2011, p. ATuA4.

[14] W. A. Gambling, “The rise and rise of optical fibers,” *IEEE J. Sel. Top. Quantum Electron.*, vol. 6, no. 6, pp. 1084–1093, 2000.

[15] The Nobel Foundation, “The Nobel Prize in Physics 2009.” 2009.

[16] S. D. Jackson, “The spectroscopic and energy transfer characteristics of the rare earth ions used for silicate glass fibre lasers operating in the shortwave infrared,” *Laser Photonics Rev.*, vol. 3, no. 5, pp. 466–482, Sep. 2009.

[17] W. E. Lamb, W. P. Schleich, M. O. Scully, and C. H. Townes, “Laser physics: Quantum controversy in action,” *Rev. Mod. Phys.*, vol. 71, no. 2, p. S263, 1999.

[18] O. Svelto, *Principles of Lasers*, Fourth. Springer, 1998.

[19] D. C. Hanna, “Continuous-wave oscillation of a monomode thulium-doped fibre laser,” *Electron. Lett.*, vol. 24, no. 19, pp. 1222–1223, 1988.

[20] A. . Kenyon, “Recent developments in rare-earth doped materials for optoelectronics,” *Prog. Quantum Electron.*, vol. 26, no. 4–5, pp. 225–284, 2002.

[21] S. D. Jackson, “Cross relaxation and energy transfer upconversion processes relevant to the functioning of 2 µm Tm3+-doped silica fibre lasers,” *Opt. Commun.*, vol. 230, no. 1–3, pp. 197–203, Jan. 2004.

[22] S. D. Jackson, “The effects of energy transfer upconversion on the performance of Tm3+, Ho3+-doped silica fiber lasers,” *IEEE Photonics Technol. Lett.*, vol. 18, no. 17, pp. 1885–1887, Sep. 2006.

[23] G. Lakshminarayana, M. Mao, R. Yang, J. R. Qiu, and M. G. Brik, “Spectroscopic investigations of Nd3+-, Er3+-, Er3+/Yb3+-, and Tm3+-ions doped SiO2–Al2O3–CaF2–GdF3 glasses,” *Phys. B Condens. Matter*, vol. 404, no. 20, pp. 3348–3355, Nov. 2009.
[24] D. Creeden, B. R. Johnson, S. D. Setzler, and E. P. Chicklis, “Resonantly pumped Tm-doped fiber laser with >90% slope efficiency,” *Opt. Lett.*, vol. 39, no. 3, pp. 470–473, Feb. 2014.
[25] “IPG PHOTONICS,” *IPG PHOTONICS*. [Online]. Available: www.ipgphotonics.com.
[26] B. M. Antipenko, A. S. Glebov, and R. V. Dumbravyanu, “Physics of energy storage in a BaEr2F8: Tm: Ho active medium,” *Sov. J. Quantum Electron.*, vol. 18, no. 6, p. 806, 1988.
[27] D. A. Simpson, “Spectroscopy Of Thulium Doped Silica Glass,” Doctor Of Philosophy, Victoria, Optical Technology Research Laboratory, 2008.
[28] Thorlabs, “Thulium-doped Single Mode and Large-Mode-Area Optical Fibers.” .
[29] G. Frith *et al.*, “Mitigation of photodegradation in 790nm-pumped Tm-doped fibers,” in *Proceedings of SPIE*, 2010, vol. 7580, p. 75800A–75800A–9.
[30] I.T. Sorokinam K.L. Vodopyanov, *Solid-State Mid-Infrared Laser Sources, Topics in Applied Physics*. 1989.
[31] S. D. Jackson and T. A. King, “Dynamics of the output of heavily Tm-doped double-clad silica fiber lasers,” *JOSA B*, vol. 16, no. 12, pp. 2178–2188, 1999.
[32] A. F. El-Sherif and T. A. King, “Dynamics and self-pulsing effects in Tm3+-doped silica fibre lasers,” *Opt. Commun.*, vol. 208, no. 4–6, pp. 381–389, Jul. 2002.
[33] D. Marcuse, “Pulsing behavior of a three-level laser with saturable absorber,” *IEEE J. Quantum Electron.*, vol. 29, no. 8, pp. 2390–2396, 1993.
[34] S. D. Jackson, “Direct evidence for laser reabsorption as initial cause for self-pulsing in three-level fibre lasers,” *Electron. Lett.*, vol. 38, no. 25, pp. 1640–1642, Dec. 2002.
[35] G. Turri, V. Sudesh, M. Richardson, M. Bass, A. Toncelli, and M. Tonelli, “Temperature-dependent spectroscopic properties of Tm3+ in germanate, silica, and phosphate glasses: A comparative study,” *J. Appl. Phys.*, vol. 103, no. 9, pp. 093104-093104-7, May 2008.
[36] UKIRT, “Atmospheric Transmission.” [Online]. Available: http://www.ukirt.hawaii.edu/astronomy/utils/index1.html. [Accessed: 01-Sep-2017].
[37] Y. J. Zhang, B. Q. Yao, S. F. Song, and Y. L. Ju, “All-fiber Tm-doped double-clad fiber laser with multi-mode FBG as cavity,” *Laser Phys.*, vol. 19, no. 5, pp. 1006–1008, May 2009.
[38] T. McComb, V. Sudesh, and M. Richardson, “Volume Bragg grating stabilized spectrally narrow Tm fiber laser,” *Opt. Lett.*, vol. 33, no. 8, pp. 881–883, Apr. 2008.
[39] E. Bahaa, *Fundamentals of Photonics*. John Wiley & Sons, 1991.
[40] Rudiger Paschotta, “RP Photonics Modelling & Design Software.” [Online]. Available: https://www.rp-photonics.com/rp_fiber_calculator.html.
[41] L. Zenteno, “High-power double-clad fiber lasers,” *Light. Technol. J. Of*, vol. 11, no. 9, pp. 1435–1446, 1993.
[42] M. N. Zervas and C. . Codemard, “High Power Fiber Lasers: A Review,” *IEEE J. Sel. Top. Quantum Electron.*, vol. 20, no. 5, pp. 1–23, Sep. 2014.
[43] Nufern, “Optical Fibers,” 2016. [Online]. Available: http://www.nufern.com/pam/optical_fibers/searchresult/#/?dopants=%7B%226%22:true%7D&type=%7B%224%22:true%7D.
[44] N. Simakov *et al.*, “Design and experimental demonstration of a large pedestal thulium-doped fibre,” *Opt. Express*, vol. 23, no. 3, p. 3126, Feb. 2015.
[45] J. P. Koplow, D. A. Kliner, and L. Goldberg, “Single-mode operation of a coiled multimode fiber amplifier,” *Opt. Lett.*, vol. 25, no. 7, pp. 442–444, 2000.
[46] T. S. McComb, “Power Scaling of Large Mode Area Thulium fiber lasers in various spectral and temporal regimes,” University of Central Florida Orlando, Florida, 2009.
[47] M. Faucher and Y. K. Lize, “Mode Field Adaptation for High Power Fiber Lasers,” 2007, pp. 1–2.
[48] M. J. F Digonnet and C. J. Gaeta, “Theoretical analysis of optical fiber laser amplifiers and oscillators,” *OSA*, vol. 24. No. 3, no. Applied Optics, pp. 333–342, 1986.

[49] Anthony E. Siegman, *Lasers*. California: University Science Books, 1986.
[50] International Organisation for Standardization, “Lasers and laser-related equipment-Test methods for laser beam widths, divergence angles and beam propagation ratios,” 2005. [Online]. Available: http://www.auniontech.com/uploadfile/2011/35/13149580538536.pdf.
[51] T. S. McComb, L. Shah, R. A. Sims, V. Sudesh, and M. Richardson, “High power tunable thulium fiber laser with volume Bragg grating spectral control,” 2010, p. 75801F–75801F–7.
[52] C. Kneis *et al.*, “4.5 W mid-infrared supercontinuum generation in a ZBLAN fiber pumped by a Q-switched mode-locked Tm $^{3+}$ - doped fiber laser,” 2015, p. 93420B.
[53] M. A. Chernysheva *et al.*, “Thulium-doped mode-locked all-fiber laser based on NALM and carbon nanotube saturable absorber,” *Opt. Express*, vol. 20, no. 26, pp. B124–B130, Dec. 2012.
[54] F. Z. Qamar and T. A. King, “Self-mode-locking effects in heavily doped single-clad Tm $^{3+}$ -doped silica fibre lasers,” *J. Mod. Opt.*, vol. 52, no. 8, pp. 1053–1063, May 2005.
[55] A. F. El-Sherif and T. A. King, “High-energy, high-brightness Q-switched Tm3+-doped fiber laser using an electro-optic modulator,” *Opt. Commun.*, vol. 218, no. 4–6, pp. 337–344, Apr. 2003.
[56] Y. Tang and J. Xu, “High-Power Pulsed 2-μm Tm 3-Doped Fiber Laser,” *INTECH*, no. Semiconductor Laser Diode Technology and Applications, pp. 287–320, 2012.
[57] J. Swiderski, M. Maciejewska, J. Kwiatkowski, and M. Mamajek, “An all-fiber, resonantly pumped, gain-switched, 2 μm Tm-doped silica fiber laser,” *Laser Phys. Lett.*, vol. 10, no. 1, p. 015107, Jan. 2013.
[58] A. M. Heidt *et al.*, “100 kW peak power picosecond thulium-doped fiber amplifier system seeded by a gain-switched diode laser at 2 μm,” *Opt. Lett.*, vol. 38, no. 10, pp. 1615–1617, May 2013.
[59] T. S. McComb *et al.*, “Thulium Fiber Lasers Stabilized by a Volume Bragg Grating in High Power, Tunable and Q-Switched Configurations,” in *Advanced Solid-State Photonics*, 2010, p. AMB2.
[60] G. D. Goodno, L. D. Book, and J. E. Rothenberg, “600-W single-mode single-frequency thulium fiber laser amplifier,” in *Proc. of SPIE*, 2009, vol. 7195, p. 71950Y–71950Y–10.
[61] D. Creeden *et al.*, “Thulium fiber laser-pumped mid-IR OPO,” *Proc. SPIE*, vol. 6952, no. 1, p. 69520S–69520S–7, Apr. 2008.
[62] N. Simakov *et al.*, “Mid-infrared generation in ZnGeP pumped by a monolithic, power scalable 2-μm source,” 2012, p. 82373K–82373K–6.
[63] Y. Tang, L. Xu, Y. Yang, and J. Xu, “High-power gain-switched Tm3+-doped fiber laser,” *Opt. Express*, vol. 18, no. 22, pp. 22964–22972, Oct. 2010.
[64] M. Eichhorn and S. D. Jackson, “High-pulse-energy actively Q-switched Tm3+-doped silica 2 um fiber laser pumped at 792 nm,” *Opt. Lett.*, vol. 32, no. 19, pp. 2780–2782, Oct. 2007.
[65] C. C. C. Willis *et al.*, “High-energy Q-switched Tm3+-doped polarization maintaining silica fiber laser,” 2010, pp. 758003-758003–6.
[66] P. Kadwani *et al.*, “Q-switched thulium-doped photonic crystal fiber laser,” *Opt. Lett.*, vol. 37, no. 10, pp. 1664–1666, 2012.
[67] J. E. Rothenberg, P. A. Thielen, M. Wickham, and C. P. Asman, “Suppression of stimulated Brillouin scattering in single-frequency multi-kilowatt fiber amplifiers,” 2008, p. 68730O.
[68] Andrew D. Yablon, *Optical Fiber Fusion Splicing*. Somerset, USA: Springer, 2005.
[69] 3SAE Technologies, Inc, “Large Diameter Fiber Cleaver,” 2010. [Online]. Available: http://www.3sae.com/products/large-diameter-fiber-cleaver.php. [Accessed: 01-Jun-2016].
[70] W. A. Clarkson *et al.*, “High power thulium doped fiber lasers,” in *Conference on Optical Fiber Communication - incudes post deadline papers, 2009. OFC 2009*, 2009, pp. 1–3.
[71] J. Wu, S. Jiang, T. Luo, J. Geng, N. Peyghambarian, and N. P. Barnes, “Efficient thulium-doped 2-um germanate fiber laser,” *IEEE Photonics Technol. Lett.*, vol. 18, no. 2, pp. 334–336, Jan. 2006.
[72] J. Wu, Z. Yao, J. Zong, and S. Jiang, “Highly efficient high-power thulium-doped germanate glass fiber laser,” *Opt. Lett.*, vol. 32, no. 6, pp. 638–640, Mar. 2007.
[73] S. D. Jackson and T. A. King, “High-power diode-cladding-pumped Tm-doped silica fiber laser,” *Opt. Lett.*, vol. 23, no. 18, pp. 1462–1464, 1998.

[74] Y. Zhang, Y. Tian, C. Song, W. Wang, B. Yao, and Y. Wang, “High efficient single-end operation Tm-doped silica fiber laser based on intracore FBGs,” *Laser Phys. Lett.*, vol. 6, no. 8, pp. 590–593, Aug. 2009.
[75] B. M. Walsh, “Review of Tm and Ho materials; spectroscopy and lasers,” *Laser Phys.*, vol. 19, no. 4, pp. 855–866, 2009.
[76] M. Eichhorn, “Quasi-three-level solid-state lasers in the near and mid infrared based on trivalent rare earth ions,” *Appl. Phys. B*, vol. 93, no. 2–3, pp. 269–316, Nov. 2008.
[77] Y. Tang and J. Xu, “Self-induced pulsing in Tm^{3+} -doped fiber lasers with different output couplings,” 2008, p. 72760L.
[78] G. P. Agrawal, “Chapter 5, Fibre Lasers,” in *Applications of Nonlinear Fiber Optics*, Elselvier, 2001, pp. 201–260.
[79] P. Le Boudec, M. Le Flohic, P. L. François, F. Sanchez, and G. Stephan, “Self-pulsing in Er3+-doped fibre laser,” *Opt. Quantum Electron.*, vol. 25, no. 5, pp. 359–367, 1993.
[80] S. D. Jackson and T. A. King, “Efficient gain-switched operation of a Tm-doped silica fiber laser,” *IEEE J. Quantum Electron.*, vol. 34, no. 5, pp. 779–789, May 1998.
[81] T. S. McComb *et al.*, “Atmospheric propagation testing with a high power, tunable thulium fiber laser system,” 2010, p. 75781G–75781G–7.
[82] J. Liu, H. Shi, K. Liu, Y. Hou, and P. Wang, “210 W single-frequency, single-polarization, thulium-doped all-fiber MOPA,” *Opt. Express*, vol. 22, no. 11, p. 13572, Jun. 2014.
[83] C. Gaida *et al.*, “Peak power scaling in Tm doped fiber lasers to MW-level,” 2013, p. 86012Y–86012Y–8.
[84] C. C. Willis *et al.*, “Highly polarized all-fiber thulium laser with femtosecond-laser-written fiber Bragg gratings,” *Opt. Express*, vol. 21, no. 9, pp. 10467–10474, 2013.
[85] F. Jansen, F. Stutzki, C. Jauregui, J. Limpert, and A. Tünnermann, “High-power very large mode-area thulium-doped fiber laser,” *Opt. Lett.*, vol. 37, no. 21, pp. 4546–4548, Nov. 2012.
[86] T. S. McComb *et al.*, “High-power widely tunable thulium fiber lasers,” *Appl. Opt.*, vol. 49, no. 32, pp. 6236–6242, Nov. 2010.
[87] G. D. Goodno, L. D. Book, and J. E. Rothenberg, “Low-phase-noise, single-frequency, single-mode 608 W thulium fiber amplifier,” *Opt. Lett.*, vol. 34, no. 8, pp. 1204–1206, Apr. 2009.
[88] J. Swiderski, M. Michalska, W. Pichola, and M. Mamajek, “Generation of 25-ns pulses with a peak power of over 10 kW from a gain-switched, 2-mm Tm-doped fibre laser and amplifier system,” *Quantum Electron.*, vol. 44, no. 4, p. 294, Apr. 2014.
[89] C. Kieleck, M. Eichhorn, D. Faye, E. Lallier, and S. D. Jackson, “2-µm-Fiber-Laser-Pumped OP-GaAs OPO and Its Polarization Effects,” in *Advanced Photonics & Renewable Energy*, 2010, p. NWD5.
[90] F. Wang, D. Shen, D. Fan, and Q. Lu, “Spectrum narrowing of high power Tm: fiber laser using a volume Bragg grating,” *Opt. Express*, vol. 18, no. 9, pp. 8937–8941, Apr. 2010.
[91] M. Tao, Q. Huang, P. Yang, T. Yu, W. Chen, and X. Ye, “Narrow linewidth CW amplification of a Tm-doped double-clad fiber MOPA system,” *Opt. - Int. J. Light Electron Opt.*, vol. 125, no. 3, pp. 1141–1143, Feb. 2014.
[92] Z. Jiao, B. Zhang, and B. Wang, “Linearly polarized and narrow-linewidth pulse generation at high repetition rate from an all-fiber gain-switched Thulium-doped fiber laser,” *Opt. Laser Technol.*, vol. 55, pp. 58–61, Feb. 2014.
[93] Y. E. Sadovnikova, V. A. Kamynin, A. S. Kurkov, O. I. Medvedkov, A. V. Marakulin, and L. A. Minashina, “Q-switching of a thulium-doped fibre laser using a holmium-doped fibre saturable absorber,” *Quantum Electron.*, vol. 44, no. 1, pp. 4–6, Jan. 2014.
[94] T. Walbaum *et al.*, “Spatially resolved measurement of the core temperature in a high-power thulium fiber system,” 2016, p. 97280P.
[95] 3SAE Technologies, Inc, “3SAE Large Diamter Splicing System-LDS 2.5,” 2010. [Online]. Available: http://www.3sae.com/products/3saelargediametersplicingsystem.php.

[96] J. Kilmer, “Optical Fiber Mode Field Diameter Specification-Statistical Analysis of Predicted Splice Loss,” in *OE/Fiber LASE’88*, 1989, pp. 245–252.
[97] C. Fu, P. Yan, Q. Xiao, D. li, and M. Gong, “Efficiency and beam quality deterioration in double-cladding fiber amplifiers induced by core misalignment of fusion splices,” *Opt. Commun.*, vol. 351, pp. 9–14, Sep. 2015.
[98] A. Wetter, M. Faucher, and B. Sévigny, “High power cladding light strippers,” in *Fiber Lasers V: Technology, Systems and Applications*, 2008, pp. 687327-687327–8.
[99] A. Kliner *et al.*, “Fabrication and evaluation of a 500 W cladding-light stripper,” in *MOEMS and Miniaturized Systes XII*, 2013, p. 86160N.
[100] David, Gerald, Seerbak, Eric, Sean, Pooler, Gordon, Edgar, Gottfried, and Evan, Matthew, Rogers, “MONOLITHIC MODE STRIPPER FIBER FERRULE/COLLIMATOR AND METHOD OF MAKING SAME,” US 7306376 B2.
[101] F. Qamar and T. A. King, “Short-pulse, high-peak-power Q-switched Tm–silica fibre laser at 1.9 m,” *Opt. Laser Technol.*, vol. 38, no. 1, pp. 1–7, Feb. 2006.
[102] Sharp R. C, Spock D. E, Pan N, and Elliot J, “190 fs passively mode-locked thulium fiber laser with low threshold,” *Cleo*, p. 31, 1996.
[103] P. Glas, M. Naumann, A. Schirrmacher, L. Däweritz, and R. Hey, “Self pulsing versus self locking in a cw pumped neodymium doped double clad fiber laser,” *Opt. Commun.*, vol. 161, no. 4–6, pp. 345–358, Mar. 1999.
[104] A. Dergachev, D. Armstrong, A. Smith, T. Drake, and M. Dubois, “High-power, high-energy ZGP OPA Pumped by a 2.05-µm Ho:YLF MOPA System,” in *Proceedings of SPIE - The International Society for Optical Engineering*, 2008, vol. 6875.
[105] B. C. Stuart, M. D. Feit, A. M. Rubenchik, B. W. Shore, and M. D. Perry, “Laser-Induced Damage in Dielectrics with Nanosecond to Subpicosecond Pulses,” *Phys. Rev. Lett.*, vol. 74, no. 12, pp. 2248–2251, Mar. 1995.
[106] Weisstein, Eric W, “Bessel Function of the First Kind,” *Wolfram Mathworld*. [Online]. Available: http://mathworld.wolfram.com/BesselFunctionoftheFirstKind.html.
[107] Weisstein, Eric W, “Bessel Function of the Second Kind,” *Wolfram Mathworld*. [Online]. Available: http://mathworld.wolfram.com/BesselFunctionoftheSecondKind.html.

Appendix A: Supplementary mathematics

Derivation of the V parameter from Helmholtz's equation

This derivation is continued from section 2.3. and is taken is taken from the book Fundamentals of Photonics [39].....Helmholtz's equation can be rewritten in cylindrical coordinates as,

$$\frac{\partial^2 U}{\partial r^2}+\frac{1}{r}\frac{\partial U}{\partial r}+\frac{1}{r^2}\frac{\partial U^2}{\partial \phi^2}+\frac{\partial^2 U}{\partial z^2}+n^2k^2U=0 \quad ...(14)$$

Treating the wave function $U(r,\phi,z)$ as a travelling wave along in the z direction and as a periodic function in the azimuthal direction ϕ, we write U as,

$$U(r,\phi,z)=u(r)e^{-jl\phi}e^{-jz\beta} \quad ...(15)$$

where $u(r)$ is the complex amplitude, l is an integer (l = 0, ±1, ±2, ...,) and β is the wave propagation constant. Substituting Equation 15 into Equation 14 results in an ordinary differential equation,

$$\frac{d^2u}{dr^2}+\frac{1}{r}\frac{du}{dr}+\left(n^2k^2-\beta^2-\frac{l^2}{r^2}\right)u=0 \quad ...(16)$$

Analysis of Equation 16 reveals that if $\beta < n_1 k$ and $\beta > n_2 k$ β then the wave is bound (guided) in the fibre core. For convenience we define,

$$k_T^2=n_1^2k^2-\beta^2 \quad ...(17)$$

$$\gamma^2=\beta^2-n_2^2k^2 \quad ...(18)$$

where for guided waves, k_T^2 and γ^2 are positive and k_T and γ are real. Equation 5 can be rewritten for separate instances. That is when $r < a$ (core guided) and $r > a$ (cladding guided).

$$\frac{d^2u}{dr^2}+\frac{1}{r}\frac{du}{dr}+\left(k_T^2-\frac{l^2}{r^2}\right)u=0,\ r<a \quad ...(19),$$

$$\frac{d^2u}{dr^2}+\frac{1}{r}\frac{du}{dr}-\left(\gamma^2+\frac{l^2}{r^2}\right)u=0,\ r>a \quad ...(20)$$

The solutions to Equations 8 and 9 belong to the family of Bessel functions. This can easily be shown by substituting $x=k_T r$ and $x=\gamma r$ into Equations 8 and 9 respectively. Equations 8 and 9 are type 1

and type 2 Bessel functions respectively. The solutions to these Bessel functions in the limit x >>1 with integer values of l are[102,103],

$$J_l(x) \approx \left(\frac{2}{\pi x}\right)^{\frac{1}{2}} \cos\left[x - \left(l + \frac{1}{2}\right)\frac{\pi}{2}\right], \; x >> 1 \; \ldots(21)$$

$$K_l(x) \approx \left(\frac{\pi}{2x}\right)^{\frac{1}{2}} \left(1 + \frac{4l^2 - 1}{8x}\right) \exp(-x), \; x >> 1 \; \ldots(22)$$

where $x = k_T r$ and $x = \gamma r$. The combined solution for the core and cladding are a piecewise function which can be represented as,

$$u(r) \propto \begin{cases} J_l(k_T r), r < a(core) \\ K_l(\gamma r), r > a(cladding) \end{cases} \ldots(23)$$

Figure 92 is a plot of Equation 12 for $l = 1$ (*left)* and $l = 3$ (*right)*. The proportionality constants k_T and γ are chosen such that r is continuous and differentiable at $r = a$.

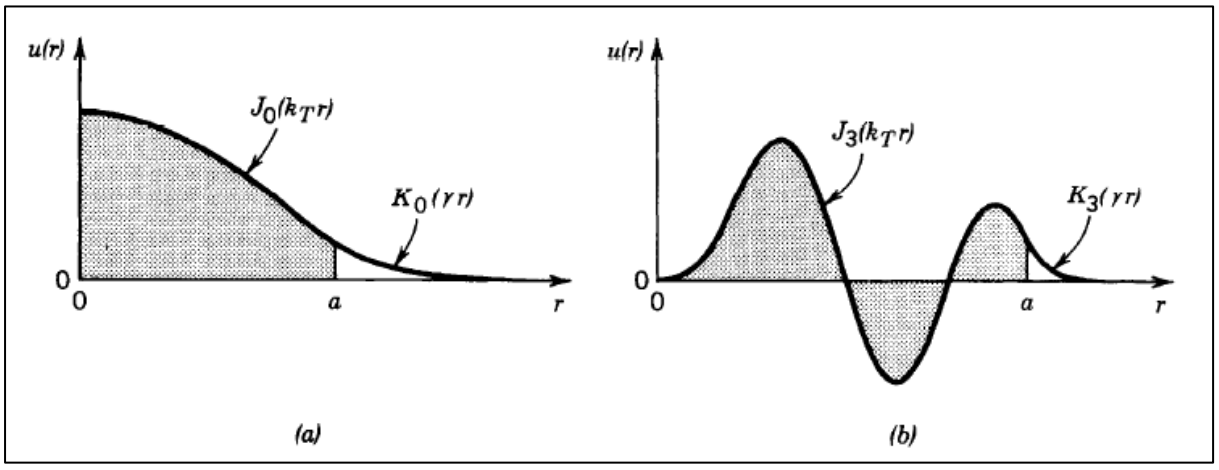

Figure 92: Radial plot of $u(r)$ with the proportionality constants γ and k_T chosen such that the function is continuous at $r = a$. *Left,* plot of $u(r)$ with $l = 1$ and *right,* $l = 3$.

From Equation 6 and 7 it can be shown that the sum of the squares (k_T)^2 and (γ)^2 is constant,

$$k_T^2 + \gamma^2 = (n_1^2 - n_2^2)k^2 = (NA)^2 k^2 \; \ldots(24)$$

where NA, is the numerical aperture as defined in Equation 1. For convenience the sum of the squares of k_T and γ are normalised such that

$$X = k_T a, \qquad \text{and} \qquad Y = \gamma a \; \ldots(25)$$

We now define the V parameter given by

$$X^2 + Y^2 = V^2 \text{ ...(26)}$$

From which it can be seen from Equation 24 that

$$V = 2\pi \frac{a}{\lambda} NA \text{ ...(27)}$$

Appendix B: Component specifications

Table 11: Gooch & Housego AO Q-switch Specifications.

Manufacturer	Gooch & Housego
Device	AO Q-switch
Model number	QS027-10M(BR)-NL6
Wavelength	2054 mm
Polarisation	Linear (vertical to base)
Interaction material	Crystal quartz
Optical faces	Brewster angled (parallel)
Damage threshold	> 500 MW/cm2
Frequency	27.12 MHz
Acoustic mode	Compressional
Active aperture	6.5 mm
Clear aperture	8.0 mm
Interaction length	46.0 mm
Loss modulation	~ 60 % @ 100 W RF power
Max recommended RF power	100 W
Cooling	Water (de-ionised)
Housing	Standard QS27-xx-B (Aluminium)

Table 12: Gooch & Housego RF driver specifications.

Manufacturer	Gooch & Housego
Device	High power RF driver for acousto-optic Q-switch
Model number	MQH0XX-YYDS3-ZZZ
RF frequency	24, 27.12, 40.68, 68 or 80 MHz
RF power	Up to 100 W
Pulse rate	Up to 100 kHz

Table 13: Optigrate 2036.1 nm VBG specifications.

Manufacturer	OptiGrate
Component	Volume Bragg Grating (VBG)
Diffraction efficiency [%]	> 99.5
Resonant wavelength [nm] (in air @ 22 °C)	2036.1
Spectral selectivity [nm] FWHM	< 0.5
Grating tilt [deg] (azimuth x elevation)	-0.4 x -0.1
Thickness [mm]	15.0
Aperture [mm]	5.0 x 5.0
Clear aperture [%]	> 85
Surface (1) flatness [λ] (2) scratch-dig)	**(1)** λ/4 **(2)** 0/10
AR coating [%] @ RWL	< 0.5

Table 14: Optigrate 1939.8 nm VBG specifications.

Manufacturer	OptiGrate
Component	Volume Bragg Grating (VBG)
Diffraction efficiency [%]	~91
Resonant wavelength [nm] (in air @ 22 °C	1939.8
Spectral selectivity [nm] FWHM	< 1.0
Grating tilt [deg] (azimuth x elevation)	1.10 x -0.36
Thickness [mm]	5.8
Aperture [mm]	12 x 5
Clear aperture [%]	> 85
Surface (1) flatness [λ] (2) scratch-dig)	**(1)** λ/4 **(2)** 20/10
AR coating [%] @ RWL	< 0.1

Appendix C: Parameter settings

Table 15: 3SAE LDS splice parameters for LMA Nufern 25/400 passive and TDF.

Splice parameter	Setting
Splicing gain [set point]	-3
Prefuse time [s]	1
Arc time 1 [s]	0.3
Arc time 2 [s]	3.5
Prefuse power [set point]]	85
Arc power 1 [set point]	85
Arc power 2 [set point]	85
Push distance [µm]	65
Pull distance [µm]	0
ROF splice offset [µm]	0
Pull time [s]	0
Splice mode	Piezo
Pull power [SP]	o

Table 16: Parameter settings for Vytran PTR-200-MRC for recoating a Nufern 25/400 TDF to passive splice

Parameter	Setting
Lamp 1 [%]	0-50
Lamp 2 [%]	51-100
Cure time [s]	240
Cooldown time [s]	300

Table 17: Parameter setting for 3SAE LCCII cleaver for the various fibres used in this dissertation.

Cleave Parameter	Nufern LMA 25/400 TDF/passive flat cleave	Nufern LMA 25/400 TDF/passive angle cleave	Nufern LMA PM 25/400 flat cleave
Tension [N]	12	12	9.3
Twist [deg]	0	14.5	0
Clamp force [N]	100	100	100
Blade speed	5	5	20
Vibration [Hz]	5	5	150
Pause for anvil [s]	1	1	1